



UNIVERSITY OF LEEDS

Design and Fabrication of Soft Magnetic Manipulators for Clinical Applications

Zaneta Milena Koszowska

**Submitted in the accordance with the requirements for the Degree of
Doctorate in Philosophy**

The University of Leeds

**Faculty of Physical Sciences and Engineering
School of Electronic and Electrical Engineering**

May 2024

Intellectual Property and Publication Statements

I confirm that the work submitted is my own, except where work which has formed part of jointly authored publications has been included. My contribution and the other authors to this work has been explicitly indicated below. I confirm that appropriate credit has been given within the thesis where reference has been made to the work of others.

Chapter 3 includes work from jointly authored publications:

1. Feasibility of Fiber Reinforcement Within Magnetically Actuated Soft Continuum Robots, P. Lloyd, Z. Koszowska, M. Di Lecce, O. Onaizah, J. H. Chandler and P. Valdastrì, *Front. Robot. AI*, 08 July 2021, Sec. Soft Robotics, Volume 8 - 2021
<https://doi.org/10.3389/frobt.2021.715662>

The contribution to this work is as follows:

Design conception, simulation, experimental setup, data analysis and manuscript preparation: PL

Prototyping, experimental design and manuscript revision: ZK

Simulation and experimental setup: ML

Design conception, experimental design, data analysis and manuscript revision: OO

Design conception, prototyping, experimental design and setup and manuscript revision: JHC

Scientific support and manuscript revision: PV

2. Personalized magnetic tentacles for targeted photothermal cancer therapy in peripheral lungs, G. Pittiglio, J. H. Chandler, T. da Veiga, Z. Koszowska, M.

Brockdorff, P. Lloyd, K. L. Barry, R. A. Harris, J. McLaughlan, C. Pompili, P.

Valdastri, *Commun Eng* **2**, 50 (2023). <https://doi.org/10.1038/s44172-023-00098-9>

The contribution to this work is as follows:

Conceptualization: GP, JHC, Td., ZK, MB, PL, PV

Methodology: GP, JHC, TdV, ZK, MB, PL, RH, PV, JM.

Investigation: GP, JHC, TdV, ZK, MB, PL, CP, JM, KB, CP, RH, PV

Visualization: GP, MB

Funding acquisition: JM, RH, PV

Project administration: GP, JC, PV

Supervision: GP, JC, PV

Writing - original draft: GP, JHC, TdV, ZK, MB, PL

Writing - review & editing: GP, JHC, TdV, ZK, MB, PL, JM, RH, PV

Chapter 4 includes work from jointly authored publication:

Independently Actuated Soft Magnetic Manipulators for Bimanual Operations

in Confined Anatomical Cavities, Z Koszowska, M Brockdorff, T da Veiga, G

Pittiglio, P Lloyd, T Khan-White, R A Harris, J W Moor, J H Chandler, and P

Valdastri, *Adv. Intell. Syst.*, 6:2300062. <https://doi.org/10.1002/aisy.202300062>

The contribution to this work is as follows:

Idea conceptualisation: ZK, MB, TdV, GP, PL, JHC, RAH, PV

SMM design: ZK, JC

Experimental design: ZK, MB, TdV

Medical input: TK-W, JWM

Data collection: ZK, MB

Data analysis: ZK, MB, TdV, PL

Manuscript writing: ZK, MB, TdV, PL, JHC, TK-W

Manuscript revisions: all authors

Supervision: JHC, RAH, PV

Clinical supervision: JWM

Chapter 5 includes work from jointly authored publication:

Selective Geometric Modification for Independent Actuation of Multiple Soft Magnetic Manipulators," Z. Koszowska, A. Bacchetti, P. R. Lloyd, G. Pittiglio, J. H. Chandler and P. Valdastrì, 2023 IEEE International Conference on Robotics and Biomimetics (ROBIO), Koh Samui, Thailand, 2023, pp. 1-6, doi: 10.1109/ROBIO58561.2023.10354735

The contribution to this work are as follows:

Idea conceptualisation: ZK, PRL, GP, JHC, PV

SMM design: ZK

Experimental design: ZK, JHC

Data collection: ZK

Data analysis: ZK, AB

Manuscript writing: ZK

Manuscript revisions: all authors

Supervision: JHC, PV

Chapter 6 includes work from jointly authored publication:

A Pneumatic Anchoring Mechanism for Improved Stability in Soft Magnetic

Manipulators for Surgery; Z. Koszowska, M. Brockdorff, P. R. Lloyd, J. H.

Chandler and P. Valdastrì;

2024, Manuscript submitted to Robosft, IEEE

The contributions to this work are as follows:

Idea conceptualisation: ZK, PRL, JHC

Design: ZK

Experimental design: ZK, MB

Data collection: ZK, MB

Data analysis: ZK, MB

Manuscript writing: ZK, MB

Manuscript revisions: all authors

Supervision: JHC, PV

This copy has been supplied on the understanding that it is copyright material and that no quotation from the thesis may be published without proper acknowledgement.

© 2024 The University of Leeds, Zaneta Koszowska

Acknowledgements

I would like to express my gratitude to Professor Pietro Valdastri for the opportunity to undertake this PhD, and for his guidance and advice throughout my time in Storm Lab.

My biggest thanks go to James Chandler and Pete Lloyd for their constant support, technical advice and brainstorming sessions. Special appreciation goes to Samwise for always providing spot-on technical advice. And to all my co-authors, thank you for your invaluable contributions.

A special thanks go to Michael for enduring what felt like countless months (or has it been years?) of experiments in the lab with me and for solving all my magnetic problems.

To the tentacle office team - Michael, Tomas, Josh, Nikita, Pete, Ali, Vittorio - thank you for the daily banter and endless tea breaks. And to all the Storm Lab members for their technical advice, and equally important - amusing lunch conversations.

To my dear friends, Weronika and Ola, for always believing in me.

Lastly, I dedicate this thesis to my parents, Beata and Edek, with all my love and gratitude.

Abbreviations

CT – Computer Tomography

dEPM -dual External Permanent Magnet

DoF - Degree of Freedom

DS - DragonSkin

EES - Endoscopic Endonasal Surgery

EET - Endoscopic Endonasal Transsphenoidal

EF - EcoFlex

EPM - External Permanent Magnet

FBG – Fiber Bragg Grating

FDM - Fused Deposition Modelling

ID - Inner Diameter

LMPA – Low Melting Point Alloy

NdFeB - Neodymium, Iron and Boron alloy

OD - Outer Diameter

OM - Orthogonal Magnetisation

PLA - Polylactic Acid

PM - Parallel Magnetisation

RMSE - Root Mean Square Error

SLA - Stereolithography

SMA - Shape Memory Alloy

SMM - Soft Magnetic Manipulator

SMM_{LB} - Soft Magnetic Manipulator Left Base

SMM_{LT} - Soft Magnetic Manipulator Left Tip

SMM_{RB} - Soft Magnetic Manipulator Right Base

SMM_{RT} - Soft Magnetic Manipulator Right Tip

UV - Ultraviolet

Table of Contents

Intellectual Property and Publication Statements	iii
Acknowledgements	vii
Abbreviations	viii
Abstract	xiii
Chapter 1 Introduction	1
1.1 Motivation	1
1.2 Contributions	3
1.3 Thesis structure	6
Chapter 2 State of the art	10
2.1 Endoscopic procedures and current challenges	10
2.2 Soft Robots for Medical Applications	13
2.3 Magnetically Actuated Soft Devices	16
2.4 Functionalizing SMMs for Clinical Applications	23
Chapter 3 SMM Fabrication	36
3.1 Fabrication techniques	36
3.1.1 Instrumentation	39
Chapter 4 Independent SMM Actuation	42
4.1 Introduction	43
4.2 Results	47
4.2.1 Principle of Magnetic Actuation	47
4.3 Segment Design	49
4.3.1 Segment Fabrication	51
4.3.2 Segment Design Evaluation	52

4.4 Modular Design for Independent Control.....	55
4.4.1 Orthogonal Magnetization Strategy	57
4.4.2 Parallel Magnetization Strategy	59
4.4.3 Independent Control Characterization	61
4.4.4 Phantom Testing	73
4.5 Discussions and Conclusions.....	77
Chapter 5 Double Helix Optimization	85
5.1 Introduction.....	86
5.2 Double Helix Reinforced SMM.....	88
5.2.1 Principles of Magnetic Actuation	88
5.2.2 Design and Fabrication	90
5.3 Results.....	93
5.3.1 Design Evaluation.....	93
5.4 Discussion and Future Work.....	100
5.5 References.....	103
Chapter 6 Stability in SMMs	107
6.1 Introduction.....	108
6.2 Pneumatic-Magnetic Multi-Modal SMM Approach	111
6.3 Operational Principles.....	112
6.3.1 Principles of Magnetic Actuation	112
6.3.2 Pneumatic Chamber Design and Fabrication.....	113
6.4 Results.....	115
6.4.1 The Anchor Experiment.....	115
6.4.2 Tip Independence.....	116
6.5 Case Study: Demonstration in a Brain Phantom.....	119

6.6 Discussion and Future Work.....	121
6.7 Acknowledgements.....	123
6.8 References.....	124
Chapter 7 Discussion and Future Directions	129
7.1 Open Challenges	132
7.1.1 Miniaturization.....	132
7.1.2 Independent and Collaborative SMM actuation	133
7.1.3 Stability in surgical tasks	135
7.1.4 Biocompatibility	135

Abstract

While endoscopic approaches offer advantages over open surgeries, they still suffer from numerous limitations. One of the biggest challenges is related to device miniaturization and access to deeper anatomy. The research presented here investigates methods for enhancing endoscopic technologies using Soft Magnetic Manipulators (SMMs), enabling the needed miniaturization through magnetic actuation. We explore a novel technique to mitigate torsional behavior in unstable actuation scenarios through a monolithic double helix reinforcement. Then, we investigate methods for simultaneously actuating two SMMs within a single anatomical and magnetic workspace. The first method entails employing the double helix reinforcement in conjunction with a specific magnetization profile of the SMMs to enable independent actuation of both. The second method involves applying local gradient fields, maintaining homogeneity in mechanical and magnetic designs between the agents. Cross-talk, cross activation and available area for each manipulator were experimentally evaluated for both methods. Clinical applicability of the proposed system was shown in a brain phantom, mimicking laser ablation of a lesion in a pituitary fossa. Evaluation of laser tip position showed the average positional error of 0.13 mm. Furthermore, the double helix reinforcement is extensively examined in a characterization study. Nine prototypes with varied design parameters are compared to identify the ones that correspond to the most optimal response to unstable actuation cases.

Lastly, another critical aspect addressed in this thesis revolves around overcoming the challenge of ensuring the stability of the soft body of a continuum magnetic manipulator during clinical

procedures. To address this, the SMM was engineered with an integrated pneumatic chamber that, when inflated, anchors within the anatomy, providing essential stability for procedures requiring precise control or payload at the tip. Our findings reveal that the anchored SMM exhibited a 73.26% increase in accuracy when drawing a circle with its tip compared to an unanchored SMM, showing promise to be used in clinical environments for precise control of an endoscopic tool.

Chapter 1 Introduction

1.1 Motivation

Reducing the invasiveness of surgical procedures has been a longstanding goal for researchers. The field of surgical technologies has witnessed numerous innovations, ranging from novel tools and materials to advanced surgical techniques and robotic solutions, driving significant progress in recent years [1]. Among these innovations, soft magnetic robots offer significant advantages over the surgical tools currently in use. The elastic modulus close to that of soft tissues makes them a great candidate for minimally invasive or endoluminal approaches [2]. This is especially important when navigating in delicate or fragile anatomy, such as brain, vasculature or tissues affected by disease. The potential for extreme miniaturization enabled through magnetic actuation has opened doors for expanding use of soft robots to deeper anatomy.

Even though many significant advancements have been made in the field in recent years, the technology still presents itself with plenty of challenges that need to be solved before it can be implemented in surgical scenarios [3]. Due to their cylindrical shape and material compliance, they suffer from instability in complex navigation scenarios, where magnetization direction create an obtuse angle with external field direction [4]. Additionally, the majority of research on magnetic continuum devices focuses on their navigation methods and not many explore how to implement surgical functionality to the devices, upon arrival at a target. This is a crucial area to be explored and tested before SMMs can be implemented in real-life surgical scenarios as manipulators. One of the challenges in terms of functionalizing SMMs for surgery is the requirement for multiple

tools. In many surgical scenarios, there are numerous tools or scopes used at the same time or alternately. This means, there is a need for developing methods of actuating multiple SMMs independently and collaboratively. This is challenging with magnetic actuation due to multiple tools responding simultaneously to magnetic field changes in the environment. Local field application with currently used magnetic field generating systems is either impossible or very challenging to achieve. Therefore, implementing more than one SMM in magnetic workspace remains an open challenge.

Moreover, another challenge that must be overcome before SMMs can be applied in practical applications is ensuring stability to perform surgical tasks effectively. Due to the high compliance of elastomeric bodies, they require stiffening or anchoring to execute precise tasks or those that necessitate force transmission at the tip. To tackle this challenge the last part of this thesis investigates utilization of an anchoring mechanism that stabilizes the SMM for precise task execution.

The motivation behind the work detailed in this thesis stemmed from the clinical necessity of enhancing endoscopic tools in terms of their maneuverability and interactions with tissue. With the long-term goal in mind of miniaturizing endoscopic devices for deep access to the anatomy, this thesis explores methods utilizing magnetic actuation of soft robots. The content presented in this dissertation is anticipated to bridge the gap between research on soft endoscopic robots and their real-life applications.

1.2 Contributions

Based on highlighted scientific and clinical motivations, this thesis presents methods that enable functionalization of SMMs and which in long term would facilitate the transition of SMMs into clinical practice. In particular, the work presented in this thesis is aimed to answer following research objectives:

1. To develop a method for reducing torsional behaviour in unstable scenarios in SMM actuation, where vector of magnetic field direction creates an obtuse angle with the SMM magnetization direction.
2. To develop methods facilitating independent actuation of two SMMs in one magnetic and anatomical workspace.
3. To develop a stabilisation mechanism for SMMs, providing magnetic tip independence and stability during actuation.

The content of this thesis, along with the scientific groundwork that led to its developments, has been published in peer-reviewed journal articles, conference presentations and patent applications:

Mechanical Reinforcement towards Fully Soft Magnetic Endoscopic Endonasal Surgical Manipulators 2021 CRAS, **Z Koszowska**, G Pittiglio, J Chandler, M Brockdorff, P Valdastrì

Mechanical Reinforcement towards Fully Soft Magnetic Endoscopic Endonasal Surgical Manipulators 2022 Hamlyn Symposium **Z Koszowska**, G Pittiglio, J Chandler, M Brockdorff, P Valdastrì

Guidelines for robotic flexible endoscopy at the time of COVID-19, 2021, Frontiers in Robotics and AI, O Onaizah, **Z Koszowska**, C Winters, V Subramanian, D Jayne, A Arezzo, K L Obstein, P Valdastrì
<https://doi.org/10.3389/frobt.2021.612852>

Feasibility of Fiber Reinforcement Within Magnetically Actuated Soft Continuum Robots 2021, Frontiers in Robotics and AI; P Lloyd, **Z Koszowska**, M Di Lecce, O Onaizah, J H Chandler, P Valdastrì
<https://doi.org/10.3389/frobt.2021.715662>

Personalized Magnetic Tentacles for Targeted Photothermal Cancer Therapy in Peripheral Lungs, Nature Communications Engineering; G Pittiglio, J H Chandler, T da Veiga, **Z Koszowska**, M Brockdorff, P Lloyd, K L Barry, R A Harris, J McLaughlan, C Pompili, P Valdastrì
<https://doi.org/10.1038/s44172-023-00098-9>

Independently Actuated Soft Magnetic Manipulators for Bimanual Operations in Confined Anatomical Cavities, **Z Koszowska**, M Brockdorff, T da Veiga, G Pittiglio, P Lloyd, T Khan-White, R A Harris, J W Moor, J H Chandler, and P Valdastrì, Adv. Intell. Syst., 6: 2300062.

<https://doi.org/10.1002/aisy.202300062>

Selective Geometric Modification for Independent Actuation of Multiple Soft Magnetic Manipulators," **Z Koszowska**, A Bacchetti, P Lloyd, G Pittiglio, J H Chandler and P Valdastrì, 2023 IEEE International Conference on Robotics and Biomimetics (ROBIO), Koh Samui, Thailand, 2023, pp. 1-6,

doi: 10.1109/ROBIO58561.2023.10354735

Magnetic Shape-Forming Surgical Continuum Manipulator 2023, US patent, P Valdastrì, J H Chandler, G Pittiglio, P R Lloyd, T G Da Veiga, **Z M Koszowska**, O Onaizah, R A Harris, H E Owston, S J Russell

1.3 Thesis structure

This thesis is structured as follows:

Chapter 2: State of the art

This chapter starts with a brief history of endoscopic procedures and is followed by highlighting current challenges in endoscopy. It includes literature review on soft robotics for endoscopic applications.

Chapter 3: SMM Fabrication

This chapter covers fabrication methods for SMMs that I developed during my PhD. The methods include molding techniques, preparation of magnetic elastomer, as well as assembly of the SMMs with functional components, such as cameras and fibers.

Some of the techniques presented in this chapter were published as a part of the following publications:

Feasibility of Fiber Reinforcement Within Magnetically Actuated Soft Continuum Robots
2021, Frontiers in Robotics and AI; P. Lloyd, **Z. Koszowska**, M. Di Lecce, O. Onaizah, J.
H. Chandler, P. Valdastrì

Personalized Magnetic Tentacles for Targeted Photothermal Cancer Therapy in Peripheral
Lungs, Nature Communications Engineering; G. Pittiglio, J. H. Chandler, T. da Veiga, **Z.
Koszowska**, M. Brockdorff, P. Lloyd, K. L. Barry, R. A. Harris, J. McLaughlan, C.
Pompili, P. Valdastrì

The fabrication, designs, and assembly techniques presented in this chapter were background work for further developments presented in my first-author publications in Chapters 4-6.

Chapter 4: Independent SMM actuation

This chapter presents a novel approach to SMM design. The double helix reinforcement reduces torsional behavior of the manipulator in unstable actuation scenarios, at the same time facilitating independent actuation of two SMMs in one workspace. This is achieved through heterogeneity of the two SMMs, in terms of their magnetic and mechanical designs. An alternative solution for independently actuating the SMMs is also presented, by the means of local magnetic gradient application, enabling independent control of two magnetically homogenous agents in one magnetic workspace. The designs are thoroughly tested in terms of their available workspace under magnetic actuation. The system is then demonstrated in a brain phantom, mimicking ablation of a pituitary lesion.

Chapter source: Independently Actuated Soft Magnetic Manipulators for Bimanual Operations in Confined Anatomical Cavities, Z Koszowska, M Brockdorff, T da Veiga, G Pittiglio, P Lloyd, T Khan-White, R A Harris, J W Moor, J H Chandler, and P Valdastrì, *Adv. Intell. Syst.*, 6: 2300062.

<https://doi.org/10.1002/aisy.202300062>

Chapter 5: Experimental Optimization of a Double-Helix Reinforcement

This chapter explores in detail, designs presented in Chapter 4. Through experimental process, critical design parameters are varied and the prototypes are tested under magnetic field conditions

to find most optimal behavior desired for independent control. The designs with most optimal features are then tested under magnetic field, showcasing independent actuation of two and three manipulators in one workspace. The chosen designs are also tested for their capability of bending with a loaded tip.

Chapter source: Selective Geometric Modification for Independent Actuation of Multiple Soft Magnetic Manipulators," Z Koszowska, A Bacchetti, P Lloyd, G Pittiglio, J H Chandler and P Valdastri, 2023 IEEE International Conference on Robotics and Biomimetics (ROBIO), Koh Samui, Thailand, 2023, pp. 1-6,
doi: 10.1109/ROBIO58561.2023.10354735

Chapter 6: SMM Anchoring for Stability

This chapter focuses on improving the stability of the SMM's tip during endoscopic procedures. The SMM is designed with an on-board pneumatic chamber, which upon inflation, anchors in the anatomy and facilitates precise actuation of the functional tip. The design is evaluated for its anchoring strength in anatomically accurate lumen phantoms. Additionally, tip manipulation stability, both with and without the anchoring system activated, is assessed by measuring the SMM's ability to trace a parametric circle using an integrated laser fiber. The system's effectiveness is further illustrated in a case study involving a brain phantom, where the prototype equipped with a laser fiber was navigated through a brain fold.

Chapter source: A Pneumatic Anchoring Mechanism for Improved Stability in Soft Magnetic Manipulators for Surgery; Z Koszowska, M Brockdorff, P R Lloyd, J H Chandler and P Valdastrì; 2024, *Manuscript submitted to Robosoft, IEEE*

Chapter 7 - Discussions and Future Directions

This chapter summarizes and discusses research presented in this thesis. Limitations of the work are discussed in detail, as well as future work that should be conducted further based on this thesis.

Chapter 2 State of the art

2.1 Endoscopic procedures and current challenges

A significant breakthrough in medicine emerged in 1953 with the invention of the first flexible endoscope, a pivotal development that transformed medical practice and facilitated its widespread adoption [5]. Initially resembling rigid tubes, over time, endoscopes evolved into slender, thinner devices with tool channels for interventions within the body. This evolution greatly contributed to understanding many conditions better, improving diagnosis rates, and enabling localized treatment in previously challenging areas. Endoscopy's benefits lie in its minimally invasive nature, which leads to less pain, shorter recovery times, reduced risk of complications, and minimal scarring compared to traditional open surgeries [6]. Additionally, endoscopy enables direct visualization of internal organs, allowing healthcare providers to obtain accurate diagnoses and perform targeted treatments such as biopsies, removal of abnormal tissues, and insertion of stents or drainage tubes [7]. Overall, endoscopy plays a crucial role in modern medicine by facilitating early detection, diagnosis, and treatment of various medical conditions while prioritizing patient comfort and safety.

Nowadays, endoscopy is widely utilized for both diagnostic and interventional purposes across various medical specialties, including gastroenterology, pulmonology, urology, gynecology, and otolaryngology. Despite its widespread application, there remain numerous conditions within the human body where endoscopic access is not feasible due to the required depth and narrow lumen size that the device needs to travel through to reach the affected area [6]. In such instances, procedures are typically conducted through open approaches or laparoscopic surgeries, both of which may entail damage to healthy tissue to access the surgical site.

Accessibility to currently challenging anatomical regions for diagnostic and therapeutic purposes presents a significant opportunity for enhancing patient recovery times, given the absence of collateral damage to healthy tissue.

Consequently, downsizing the dimensions of existing endoscopic instrumentation holds promise for facilitating a broader range of minimally invasive procedures, particularly in anatomical areas currently calling for open surgical approaches or where localized treatment remains unfeasible. Another crucial point in advancing endoscopic interventions is interaction of the tools with healthy tissue that surrounds the affected area. Improved delicacy of the device-tissue interaction could greatly reduce trauma during endoscopic navigation and combined with miniaturization, it could significantly affect patient's comfort and pain levels during the procedure, as well as post-procedure.

Nevertheless, the need for downsizing and enhancing the safety profile of endoscopic tools introduces numerous technological hurdles, necessitating the exploration of novel solutions in actuation mechanisms and manufacturing methodologies [8].

This image has been
removed by the author
of this thesis for
copyright reasons

Figure 1.1. Examples of robotic solutions in medical practice. A. Ion platform by Intuitive Surgical B. Da Vinci by Intuitive Surgical. C and D. Monarch by J&J MedTech.

There are solutions on the market offering improved tool control and accuracy through robotic platforms, such as released in the early 2000s Da Vinci Surgical System (Intuitive Surgical, Inc., Sunnyvale, CA, USA). Since then, numerous companies specializing in surgical tools have introduced new robotic-assisted systems [9]. Notable examples that improved endoscopic procedures with robotic control is an Ion Platform for bronchoscopy by Intuitive Surgical and Monarch platform by J&J MedTech (Auris Health, Inc., Redwood City, CA, USA) (Figure 1.1). Endovascular interventions, which are also one of the most challenging procedures in terms of the importance of accuracy, have been recently presented with some robotic solutions such as with CorPath GRX and Navion and NanoFlex Robotics.

2.2 Soft Robots for Medical Applications

An alternative to tendon driven approaches, used in standard endoscopes, are soft elastomeric robots. The common actuation mechanisms involve pneumatics and hydraulics, where elastomeric chambers deform in a predesigned fashion by filling them out with pressurized air [10], [11], [12] or fluid [13], [14], [15], [16].

Due to ease of design and fabrication, those type of actuators quickly became popular in the scientific community for various applications like in gripper design, food handling and medical applications [17], [18].

Functional application of soft robots in endoscopy would require the tip to be fully operational in multiple DoF. This is a significant limitation in pneumatic and hydraulic soft robots since each DoF is supplied by a separate air/fluid connection. Additionally, hydraulically driven soft robots, even though more robust in control than pneumatic robots, are heavier due to the fluid flowing through the chambers. Both mechanisms also suffer from risks of puncture, introducing potential harm through gas leak or pressurised jets of fluid.

Pneumatic devices designed for endoscopic applications are usually made in centimetre scale, for example 10 mm in diameter as in [19], 13 mm in [20], or 14 mm in [21] and due to their size they are mainly suitable for limited applications in the gastrointestinal tract. There are smaller devices, such as 7 mm in diameter [22], intended for bronchoscopic procedures, but they provide only shallow access to the anatomy. Scaling these devices down for broader endoscopic use poses significant fabrication challenges. As pneumatic chambers get smaller, they become increasingly sensitive to variations in wall thickness, making it difficult to accurately predict their response to input pressure at smaller scales [23].

Some research groups have explored smaller scale soft robots that are pneumatically actuated, such as [10], [23], presenting designs with diameters of 2.4 mm and 2.5 mm respectively. Although these robotic systems have shown success in performing biopsies in phantoms, their limited maneuverability due to having only 1 Degree of Freedom (DoF) remains a significant drawback. A manipulator with 1 DoF can only move along a single axis, which restricts its ability to make complex movements. This limitation makes it unsuitable for tasks requiring complex manipulation, such as those in endoscopic procedures, where precise and flexible control in multiple planes is often necessary.

Apart from scaling challenges, the field of soft robotics still faces multiple limitations that need to be addressed before they can be transferred to utilisation in a human body. For applications in interventional endoscopy, apart from carrying a camera on board for diagnosis, an important feature is a tool channel that delivers tools to the site.

It is intuitive that soft robots are well-suited for endoscopic navigation due to their gentle interaction with tissues and minimized forces if any contact occurs. This however, being a benefit while navigating in the tortuous lumens, could present itself as a disadvantage in cases where procedure requires localized and accurate tip control. Therefore, endoscopic intervention such as biopsy, injection or tissue manipulation brings an inevitable challenge of buckling. The elastomeric body deforms under contact force at the tip, which can often overcome its overall stability. Addressing this challenge in soft robotics has led to numerous efforts aimed at stiffening soft robots on demand [24]. One of the methods involves utilization of Shape Memory Alloy (SMA), which under exposure to heat changes its young's modulus [25]. Presented structure stiffened 66 times upon heating, however this method poses challenges related to applying such

high temperatures (80 °C) in the human body. Similarly, utilization of low melting point alloys (LMPA) can help with modulating stiffness of a soft device e.g. as in [26], [27].

Other popular methods also include layer/fiber jamming [28], [29] and 3D printed structures such as chain mail embedded in the soft body [30], [31]. All above methods work under similar principle of stiffening through the compression/jamming of embedded elements when subjected to negative pressure. The utilization of jamming mechanisms has been primarily practiced in larger soft robots, typically at centimeter scales, and may not consistently yield comparable levels of stiffening when applied to devices at millimeter scale. Additionally due to difficulties in fabrication, miniaturization of popular stiffening approaches can be challenging, e.g. implementing sheet layers or chainmail would require precise manufacturing techniques.

2.3 Magnetically Actuated Soft Devices

The solution to miniaturising actuation components of soft robots could be utilisation of smart materials. These stimuli-responsive materials can induce shape deformation under external actuation trigger such as magnetic field, pH gradient, ultrasonication or temperature [32]. The significant advantage of such materials is in miniaturization potential, since they often eliminate the need for onboard actuation components such as motors, wires, pressure connections or tubing. An example of smart material that can be applied in medical devices is in magnetic elastomers, where addition of magnetic particles to an elastomeric matrix makes them responsive to external magnetic fields [33]. This material moulded into the shape of e.g. catheter can function as a soft robot in the body, when actuated with external source of magnetic field [34].

The precursors to soft robots with magnetic particles were devices with permanent magnets embedded in a device. Notable examples in endoscopy are tethered capsules endoscopes [35], [36], [37], [38] that are able to be pulled through anatomy with magnetic fields generated by a magnet manipulated outside of the body. Similarly, there are continuum devices, resembling endoscopes, with embedded permanent magnets, usually at its tip [27], [39], [40]. More recent advances also include devices with multiple permanent magnets with opposite magnetization directions, which leads to larger and more complex deformations than continuum devices with one magnet [41].

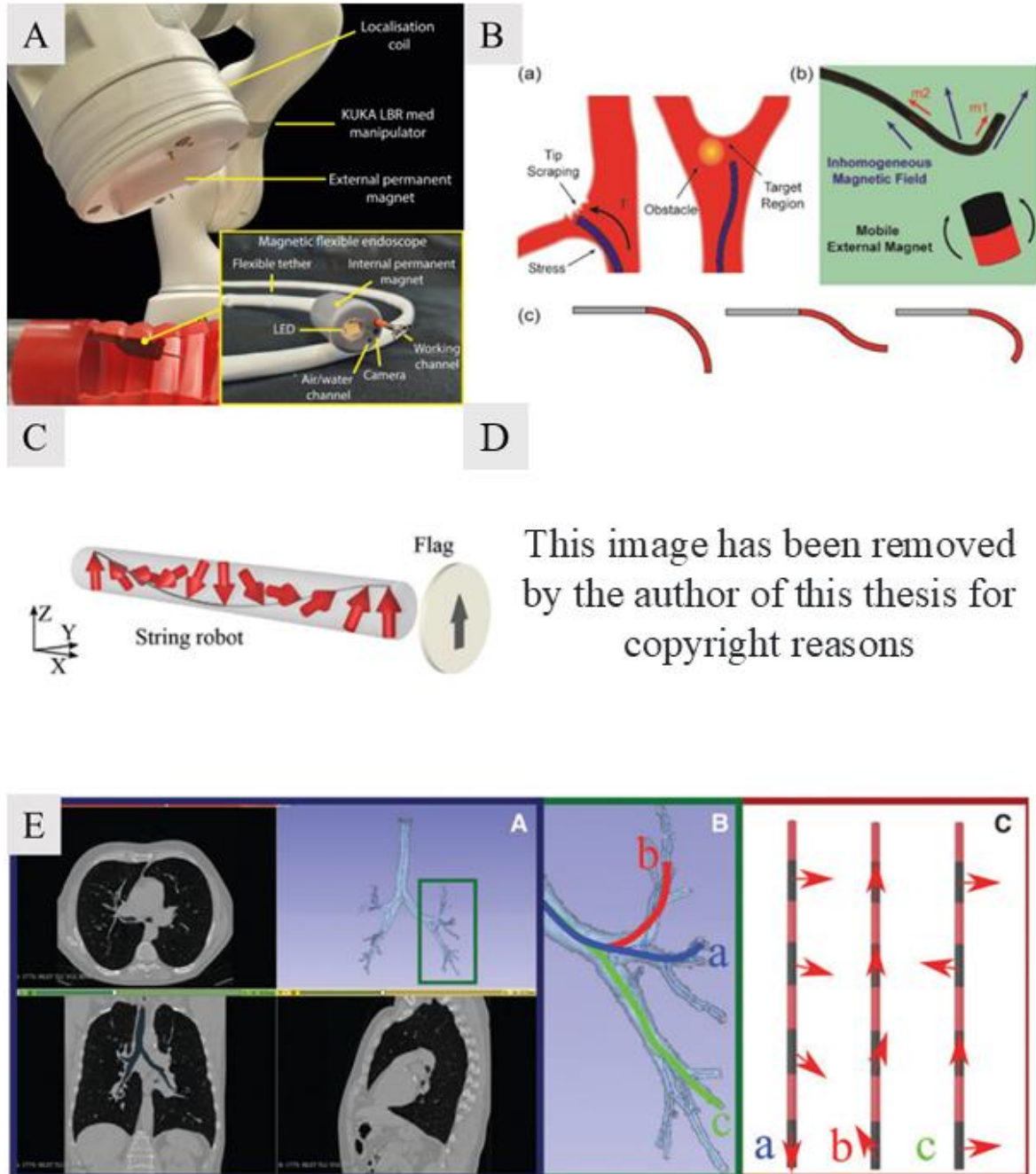


Figure 1.2. Examples of magnetic devices for medical applications. A. Magnetic Flexible Endoscope [35], ©[2019] IEEE. B. Magnetic catheter with opposite magnetization [42], ©[2022] IEEE. C and E. Magnetic soft manipulators with 3D magnetization profiles [43], [44]. D. Magnetic soft manipulator with an axial magnetization [45].

Devices with permanent magnets proved successful in some medical navigations and their major advantage is high magnetic moment, provided by a dense magnet. However, they are difficult to

miniaturize further and embedding a magnet accurately in a soft elastomeric body is challenging at the scale in question [46]. Using magnetic micro particles as a magnetic element can facilitate the needed miniaturization. Soft robots with embedded magnetic particles can be fabricated by adapting well-established fabrication techniques in soft robotics, such as injection molding, by incorporating magnetic elements into the liquid phase of the silicone thermoset [34]. Due to the lack of chambers, wiring and tubing, they can be produced in micro-scale, as opposed to their pneumatic or hydraulic precursors.

Magnetic theory

Magnetically actuated devices work under the principle of generating torques and forces through externally applied magnetic fields and gradients on the magnetized body. The internal magnetic element in the device, (either a permanent magnet or a network of magnetic micro or nano particles) is rotating to find a minimum energy state under exposure the external magnetic field [47]. This in result creates a torque, leading to deformation. A magnetic element with magnetization μ is subject to magnetic force \mathbf{f} and torque $\boldsymbol{\tau}$, under an applied field \mathbf{B} respectively as

$$\mathbf{f}(\mathbf{p}) = \nabla (\mu \cdot \mathbf{B}(\mathbf{p})) \quad (2.1)$$

$$\boldsymbol{\tau}(\mathbf{p}) = \mu \times \mathbf{B}(\mathbf{p}) \quad (2.2)$$

At position $\mathbf{p} \in R^3$ in space, where \mathbf{p} is the point the magnetic workspace where the magnetic field is aimed at, known as the focal point. Lower case bold letters represent vectors (e.g., $\mathbf{v} = [v_x \ v_y \ v_z]^T$) and the gradient operator ∇ represents partial derivatives in each of the three basis directions in the form $\nabla = \left[\frac{\partial}{\partial x} \ \frac{\partial}{\partial y} \ \frac{\partial}{\partial z} \right]^T$. Magnetic gradients allow for the generation of force,

while magnetic field misalignments generate torques on a magnetic element. Considering a workspace with x, y and z axes, equations (2.1) and (2.2) could be further expanded as

$$\mathbf{f}(\mathbf{p}) = \begin{bmatrix} f_x \\ f_y \\ f_z \end{bmatrix} = \begin{bmatrix} \mu_x & \mu_y & \mu_z & 0 & 0 \\ 0 & \mu_x & 0 & \mu_y & \mu_z \\ -\mu_z & 0 & \mu_x & -\mu_z & \mu_y \end{bmatrix} \begin{bmatrix} \frac{\partial B_x(\mathbf{p})}{\partial x} \\ \frac{\partial B_x(\mathbf{p})}{\partial y} \\ \frac{\partial B_x(\mathbf{p})}{\partial z} \\ \frac{\partial B_y(\mathbf{p})}{\partial x} \\ \frac{\partial B_y(\mathbf{p})}{\partial y} \\ \frac{\partial B_y(\mathbf{p})}{\partial z} \end{bmatrix} \quad (2.3)$$

$$\boldsymbol{\tau}(\mathbf{p}) = \begin{bmatrix} \tau_x \\ \tau_y \\ \tau_z \end{bmatrix} = \begin{bmatrix} 0 & -\mu_z & \mu_y \\ \mu_z & 0 & -\mu_x \\ -\mu_y & \mu_x & 0 \end{bmatrix} \begin{bmatrix} B_x(\mathbf{p}) \\ B_y(\mathbf{p}) \\ B_z(\mathbf{p}) \end{bmatrix} \quad (2.4)$$

Magnetic actuation through the use of two external permanent magnets, such as the dEPM platform [48], allows for individual control of magnetically induced forces and torques on magnetic objects. Pittiglio et al. [48] showed how the dEPM platform could be used to independently control the wrench of a magnetic object. This was done by using homogenous fields to control the torque and linear gradients to control the forces. Chapter 4 proposes a further alternative method to generate magnetic torques in addition to using homogenous fields.

Magnetization

In elastomeric devices with a network of hard magnetic particles, the magnetization direction can be assigned by applying an impulse magnetic field on the cured device. The impulse field causes the particles to rotate in its direction, leading to permanent (or semi-permanent) magnetization μ . First SMMs were fabricated with the magnetic profile assigned axially (along the long axis of the

SMM body) [34], [49], [50]. Fabrication of these devices does not require complex machinery nor advanced skills and can be actuated with magnetic field or gradients generated by one external permanent magnet such as in [49], [50]. They are suitable for relatively simple navigation scenarios requiring low bending angles. However, in cases where reaching the target involves navigating through a tortuous pathway or interaction with extremely fragile tissue, different approaches have been proposed. They involve more sophisticated methods in terms of SMM design as well as pre-planning the specific magnetic fields to apply which will lead to desired behavior. This method can provide complex deformations and sharp bending angles of the device, which are more suitable for convoluted paths. The principle involves magnetizing the SMM in different directions (in 3D) along its length, creating sections with varying magnetization vectors μ .

Due to the particles rotating with the direction of the external field, torque is created, leading to deformation. This can be especially useful in medical applications, where basing on a specific anatomy of a patient, e.g. bronchi as in [51], the magnetic profile can be pre-programmed into the SMM body. This, combined with a series of calculated magnetic field conditions [52] causes the SMM to shape form into the desired path. This in result minimizes contact with tissues during the navigation, leading to reduced tissue trauma [44].

In complex cases, an obtuse angle between the device's magnetization vector and the applied magnetic field can cause the SMM to twist around its main axis, rather than producing the desired bending. While careful pre-planning can help prevent this, it is not always feasible. This issue may also arise during transitional fields, such as when permanent magnets on robotic arms (as in dEPM platform [44]) switch positions to generate a sequence of fields. During these transitions, fields may form angles greater than 90 degrees with the SMM, leading to unintended torsional responses

where the SMM twists along its longitudinal axis instead of bending, as illustrated in Figures 1.3A.A and 1.3A.B. This effect can be mitigated by imposing constraints on the magnetization profile and/or actuating fields, or by introducing anisotropic stiffness. For instance, as demonstrated in [46] this can be achieved by incorporating two helical fibers into a 6 mm robot design (Figure 1.3A), or as illustrated in [4], by embedding a braid into a 2 mm robot design (Figure 1.3B). These methods however make the robots challenging to miniaturize, therefore there is still a need to explore techniques of torsion reduction in SMMs that can be miniaturized and fabricated in a repeatable manner.

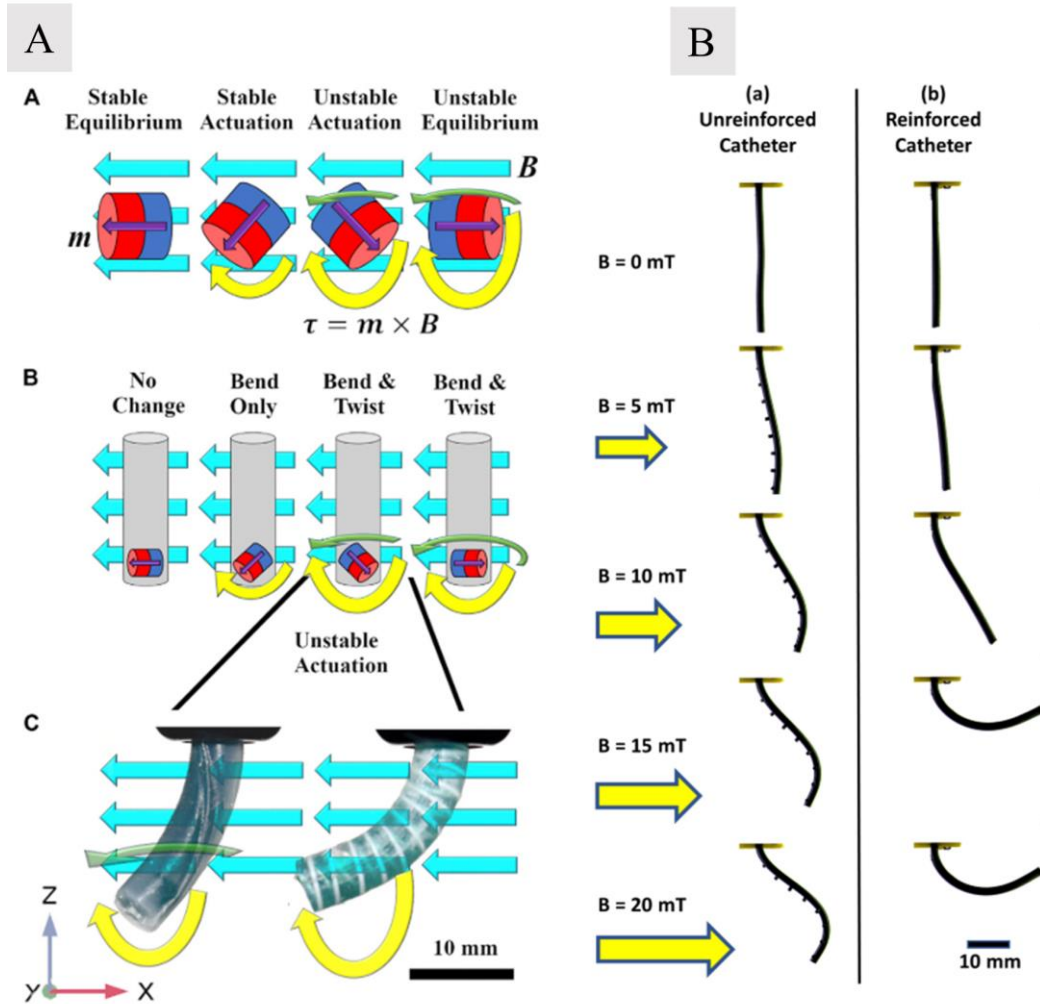


Figure 1.3A. Cases of magnetic instability and solutions. Fiber reinforced magnetic manipulator. Reproduced from [46] : (A) Magnets in free space subject to a homogeneous actuating field $[-B_x \ 0 \ 0]$ (turquoise arrows) and with

magnetization [mx 0 mz] (purple arrows). As actuation lies in the x-z plane, theoretically, torque acts only about the y axis (yellow arrows) and is zero in the unstable equilibrium position. In practice, due to the inverted pendulum instability, torque exists about both z (green arrows) and y axes. Unstable modes of actuation also produce magnetic torque which increases with deflection. (B) Once embedded in a CM these unstable torques translate as both bending and twisting deformations. (C) Photographs from experimental actuation; the unreinforced sample on the left succumbs to the twisting instability about the z-axis. The reinforced sample on the right constrains the unstable twisting mode of actuation resulting in larger magnetic torque in the desired, bending, mode of deflection. 1.3B. Braid reinforced magnetic manipulator and its deformation under magnetic field, in comparison to un-reinforced magnetic manipulator [4], ©[2022] IEEE.

There is an alternative magnetization strategy where instead of applying a large in magnitude impulse field on a set elastomer, the network of particles is arranged in a pattern while in liquid phase. This has been first widely explored for magnetic composites utilized for their magnetorheological properties such as in damping mechanisms at large scales, by simply curing samples next to a permanent magnet [53], [54]. Some researchers use curing in the presence of magnetic field to fabricate magnetic robots accurately and in a repeatable manner. For example in [55], [56], SLA techniques are adapted to cure resins with embedded magnetic particles. The structures can be magnetized pixel by pixel by maneuvering a permanent magnet beneath a reservoir of magnetic uncured material. Within the liquid resin, the particles are free to move, forming chains aligned with the magnetic field induced by the permanent magnet. Subsequently, the material is solidified using UV light. These methods enable creating soft devices with complex magnetic profiles.

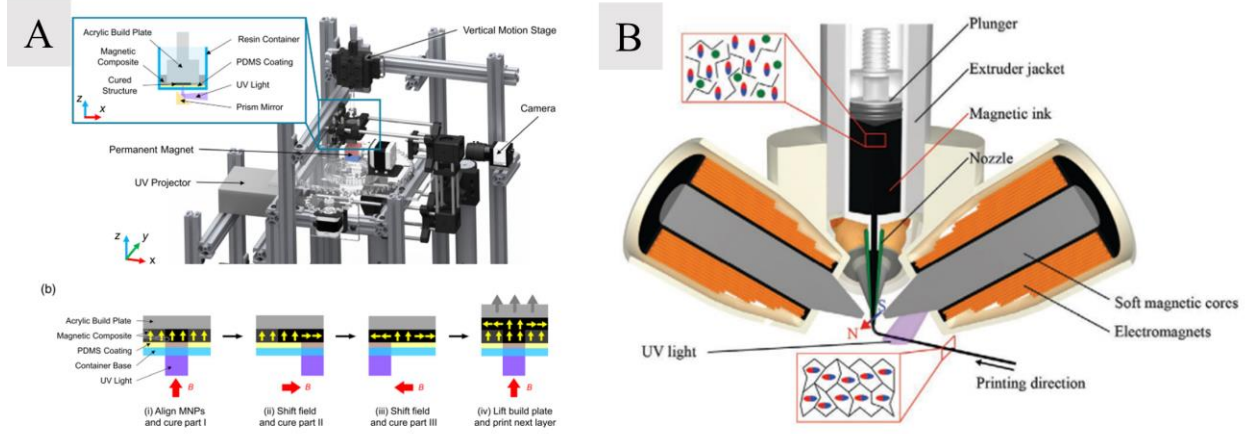


Figure 1.4. A. SLA adapted method of manufacturing soft magnetic structures with 3D magnetic profiles in a layered fashion [55]. B. 3D printing of soft magnetic structures using nozzle based printing [43].

It is worth mentioning that there are multiple research groups focusing on magnetically actuated micro-robots such [56], [57], [58], [59], [60], [61]. They have been explored in terms of medical applications, and even though the type and size of magnetic element and medical application itself, is often different to those in SMMs, some techniques used in micro robotic research can be applicable to larger scales. For instance, the only research thus far on actuating multiple magnetic agents in one workspace was explored in the field of micro robots [62], [63] (more in the following section 2.4).

2.4 Functionalizing SMMs for Clinical Applications

Obvious advantages of magnetic actuation are possibilities of extreme miniaturization and lack of additional driving components on board. However, there are drawbacks when it comes to translating magnetically actuated endoscopes into clinical practice. A major challenge is expanding use of one endoscope to multiple endoscopes/tools at once in one anatomical workspace. Most of interventional endoscopy scenarios require usage of multiple tools in either collaborative manner or one by one. Common procedures include tissue manipulation with forceps, acquiring samples for biopsy (with a needle or grippers), and tissue ablation [9]. All these

tasks require ability to actuate the scope in multiple DoFs that can be accurately controlled. Apart from the functional tools, there is also often a requirement for a camera that can visualise the operating site. In flexible endoscopy the camera is mounted at the tip, while the functional tools are passed through a channel. In multi-tool endoscopic procedures such as endonasal endoscopy, cameras are often mounted on a rigid scope. This is due to surgeons often being occupied with manipulating various tools such as forceps, drills, or laser sources during procedures. Consequently, it is advantageous to incorporate a fixed camera within the workspace, eliminating the need for additional user's attention to manipulate an extra tool. However, this setup significantly restricts the accessible area during surgery, particularly if the lesion is positioned beyond the camera's field of view. Although pre-bent rigid scopes are available, they do not substantially enhance outcomes because the camera angle remains fixed, necessitating the replacement of scopes with varying pre-bent angles to adjust the field of view during the procedure. This can be a major challenge, depending on a specific surgery. In cases where a lesion is not located in a straight path from the camera view, the procedure becomes extremely challenging and often, only partial treatment can be applied to a lesion or none at all. This results in patients requiring revision surgeries with open approaches or pharmaceutical treatments in case of cancer. In both cases, of flexible and multi-tool endoscopy, several tools are being operated in one workspace. This is an important requirement to keep in mind when designing novel and miniaturized endoscopic tools.

Considerations for multiple magnetic tools

Multi-agent magnetic control was investigated at the micro-scale for control of untethered mobile micro-robots, swimmers and spheres. The proposed methods leverage differences in

geometry[64], [65], [66], [67], [68] or magnetism[63], [69] among the agents, as well as interactions between their magnetic fields[62], [70], to produce varied behaviors under a uniform magnetic field. Additionally, sophisticated magnetic control systems, including arrays of electromagnetic coils [71], are employed to create non-uniform magnetic fields [72] or to achieve independent actuation of multiple magnetic degrees of freedom (DoFs) [73], [74]. The research in this field has primarily investigated the behavior of untethered micro-scale robots operating in a fluid environment.

Considering two magnetic SMMs in one workspace that are identical (magnetically and mechanically), application of uniform magnetic field will cause them to deform in the same direction. Intuitive solution is to magnetize the two SMMs in a manner such that only one SMM can respond, basing on magnetic heterogeneity previously explored in micro-robotics. In SMMs this method can work for only one bending primitive, however it is not suitable where high manoeuvrability and bending in multi-DoF is required, such as endoscopic applications. Additionally, unstable actuation scenarios are likely to occur in multi-DoF actuation cases. The issue of independent control of continuum SMMs within a confined workspace still remains an open challenge.

References

- [1] J. Burgner-Kahrs, D. C. Rucker, and H. Choset, “Continuum Robots for Medical Applications: A Survey,” Dec. 01, 2015, *Institute of Electrical and Electronics Engineers Inc.* doi: 10.1109/TRO.2015.2489500.
- [2] T. Da Veiga *et al.*, “Challenges of continuum robots in clinical context: A review,” *Prog. Biomed. Eng.*, vol. 2, no. 3, 2020, doi: 10.1088/2516-1091/ab9f41.

-
- [3] P. E. Dupont *et al.*, “A decade retrospective of medical robotics research from 2010 to 2020,” *Sci. Robot.*, vol. 6, no. 60, 2021, doi: 10.1126/scirobotics.abi8017.
- [4] P. Lloyd, O. Onaizah, G. Pittiglio, D. K. Vithanage, J. H. Chandler, and P. Valdastrì, “Magnetic Soft Continuum Robots With Braided Reinforcement,” *IEEE Robot. Autom. Lett.*, vol. 7, no. 4, pp. 9770–9777, 2022, doi: 10.1109/LRA.2022.3191552.
- [5] T. Arantes, D. C. Visconti, E. Luiz, and D. A. Artifon, “Robotic endoscopy. A review of the literature,” *Acta Cir Bras.*, vol. 35, no. 2, 2020, doi: doi.org/10.1590/s0102-8650202000200000006.
- [6] M. W. Gifari, H. Naghibi, S. Stramigioli, and M. Abayazid, “A review on recent advances in soft surgical robots for endoscopic applications,” *Int. J. Med. Robot. Comput. Assist. Surg.*, vol. 15, no. 5, pp. 1–11, 2019, doi: 10.1002/rcs.2010.
- [7] Z. Li and P. W. Y. Chiu, “Robotic Endoscopy,” *Visc. Med.*, vol. 34, no. 1, pp. 45–51, 2018, doi: 10.1159/000486121.
- [8] K. Kume, “Flexible robotic endoscopy: Current and original devices,” *Comput. Assist. Surg.*, vol. 21, no. 1, pp. 150–159, 2016, doi: 10.1080/24699322.2016.1242654.
- [9] D. T. H. de Moura, H. Aihara, and C. C. Thompson, “Robotic-assisted surgical endoscopy: a new era for endoluminal therapies,” *VideoGIE*, vol. 4, no. 9, pp. 399–402, 2019, doi: 10.1016/j.vgie.2019.04.014.
- [10] M. McCandless, A. Perry, N. DiFilippo, A. Carroll, E. Billatos, and S. Russo, “A Soft Robot for Peripheral Lung Cancer Diagnosis and Therapy,” *Soft Robot.*, vol. 00, no. 00, pp. 1–13, 2021, doi: 10.1089/soro.2020.0127.
- [11] J. H. Chandler, M. Chauhan, N. Garbin, K. L. Obstein, and P. Valdastrì, “Parallel Helix Actuators for Soft Robotic Applications,” *Front. Robot. AI*, vol. 7, no. September, pp. 1–

-
- 17, 2020, doi: 10.3389/frobt.2020.00119.
- [12] M. Brancadoro, M. Manti, F. Grani, S. Tognarelli, A. Menciassi, and M. Cianchetti, “Toward a variable stiffness surgical manipulator based on fiber jamming transition,” *Front. Robot. AI*, vol. 6, no. MAR, pp. 1–12, 2019, doi: 10.3389/frobt.2019.00012.
- [13] T. Ranzani, G. Gerboni, M. Cianchetti, and A. Menciassi, “A bioinspired soft manipulator for minimally invasive surgery,” *Bioinspiration and Biomimetics*, vol. 10, no. 3, 2015, doi: 10.1088/1748-3190/10/3/035008.
- [14] M. S. Xavier, A. J. Fleming, and Y. K. Yong, “Finite Element Modeling of Soft Fluidic Actuators: Overview and Recent Developments,” *Adv. Intell. Syst.*, vol. 3, no. 2, 2021, doi: 10.1002/aisy.202000187.
- [15] S. Onorati, F. Semproni, L. Paterno, G. Casagrande, V. Iacovacci, and A. Menciassi, “A hydraulic soft robotic detrusor based on an origami design,” *Proc. - IEEE Int. Conf. Robot. Autom.*, vol. 2023-May, no. Icara, pp. 6817–6822, 2023, doi: 10.1109/ICRA48891.2023.10160652.
- [16] J. Fras, Y. Noh, M. Macias, H. Wurdemann, and K. Althoefer, “Bio-Inspired Octopus Robot Based on Novel Soft Fluidic Actuator,” *Proc. - IEEE Int. Conf. Robot. Autom.*, pp. 1583–1588, 2018, doi: 10.1109/ICRA.2018.8460629.
- [17] J. Hughes, U. Culha, F. Giardina, F. Guenther, A. Rosendo, and F. Iida, “Soft manipulators and grippers: A review,” *Front. Robot. AI*, vol. 3, no. NOV, pp. 1–12, 2016, doi: 10.3389/frobt.2016.00069.
- [18] M. Cianchetti, C. Laschi, A. Menciassi, and P. Dario, “Biomedical applications of soft robotics,” *Nat. Rev. Mater.*, vol. 3, no. 6, pp. 143–153, 2018, doi: 10.1038/s41578-018-0022-y.

-
- [19] G. Gerboni, T. Ranzani, A. Diodato, G. Ciuti, M. Cianchetti, and A. Menciassi, “Modular soft mechatronic manipulator for minimally invasive surgery (MIS): overall architecture and development of a fully integrated soft module,” *Meccanica*, vol. 50, no. 11, pp. 2865–2878, 2015, doi: 10.1007/s11012-015-0267-0.
- [20] K. H. Lee *et al.*, “Nonparametric Online Learning Control for Soft Continuum Robot: An Enabling Technique for Effective Endoscopic Navigation,” *Soft Robot.*, vol. 4, no. 4, pp. 324–337, 2017, doi: 10.1089/soro.2016.0065.
- [21] T. Rehman, A. A. M. Faudzi, D. E. O. Dewi, and M. S. M. Ali, “Design, characterization, and manufacturing of circular bellows pneumatic soft actuator,” *Int. J. Adv. Manuf. Technol.*, vol. 93, no. 9–12, pp. 4295–4304, 2017, doi: 10.1007/s00170-017-0891-z.
- [22] R. F. Surakusumah, A. A. M. Faudzi, D. E. O. Dewi, and E. Supriyanto, “Development of a half sphere bending soft actuator for flexible bronchoscope movement,” *2014 IEEE Int. Symp. Robot. Manuf. Autom. IEEE-ROMA2014*, pp. 120–125, 2015, doi: 10.1109/ROMA.2014.7295873.
- [23] D. Van Lewen, T. Janke, H. Lee, R. Austin, E. Billatos, and S. Russo, “A Millimeter-Scale Soft Robot for Tissue Biopsy Procedures,” *Adv. Intell. Syst.*, vol. 5, no. 5, 2023, doi: 10.1002/aisy.202200326.
- [24] M. Manti, V. Cacucciolo, and M. Cianchetti, “Stiffening in soft robotics: A review of the state of the art,” *IEEE Robot. Autom. Mag.*, vol. 23, no. 3, pp. 93–106, 2016, doi: 10.1109/MRA.2016.2582718.
- [25] Y. Piskarev *et al.*, “Fast-Response Variable-Stiffness Magnetic Catheters for Minimally Invasive Surgery,” *Adv. Sci.*, vol. 11, no. 12, pp. 1–14, 2024, doi: 10.1002/advs.202305537.
- [26] C. Chautems, A. Tonazzini, D. Floreano, and B. J. Nelson, “A variable stiffness catheter

-
- controlled with an external magnetic field,” *IEEE Int. Conf. Intell. Robot. Syst.*, vol. 2017-
Septe, pp. 181–186, 2017, doi: 10.1109/IROS.2017.8202155.
- [27] C. Chautems, A. Tonazzini, Q. Boehler, S. H. Jeong, D. Floreano, and B. J. Nelson, “Magnetic Continuum Device with Variable Stiffness for Minimally Invasive Surgery,” *Adv. Intell. Syst.*, vol. 2, no. 6, p. 1900086, 2020, doi: 10.1002/aisy.201900086.
- [28] Y. J. Kim, S. Cheng, S. Kim, and K. Iagnemma, “A novel layer jamming mechanism with tunable stiffness capability for minimally invasive surgery,” *IEEE Trans. Robot.*, vol. 29, no. 4, pp. 1031–1042, 2013, doi: 10.1109/TRO.2013.2256313.
- [29] B. Yang *et al.*, “Reprogrammable soft actuation and shape-shifting via tensile jamming,” *Sci. Adv.*, vol. 7, no. 40, pp. 1–11, 2021, doi: 10.1126/sciadv.abh2073.
- [30] Y. Wang, L. Li, D. Hofmann, J. E. Andrade, and C. Daraio, “Structured fabrics with tunable mechanical properties,” *Nature*, vol. 596, no. 7871, pp. 238–243, 2021, doi: 10.1038/s41586-021-03698-7.
- [31] D. S. Shah, E. J. Yang, M. C. Yuen, E. C. Huang, and R. Kramer-Bottiglio, “Jamming Skins that Control System Rigidity from the Surface,” *Adv. Funct. Mater.*, vol. 31, no. 1, 2021, doi: 10.1002/adfm.202006915.
- [32] S. Bahl, H. Nagar, I. Singh, and S. Sehgal, “Smart materials types, properties and applications: A review,” *Mater. Today Proc.*, vol. 28, pp. 1302–1306, 2020, doi: 10.1016/j.matpr.2020.04.505.
- [33] A. Bacchetti *et al.*, “Optimization and fabrication of programmable domains for soft magnetic robots: A review,” *Front. Robot. AI*, vol. 9, no. November, pp. 1–10, 2022, doi: 10.3389/frobt.2022.1040984.
- [34] G. Z. Lum *et al.*, “Shape-programmable magnetic soft matter,” *Proc. Natl. Acad. Sci. U. S.*

-
- A., vol. 113, no. 41, pp. E6007–E6015, Oct. 2016, doi: 10.1073/pnas.1608193113.
- [35] L. Barducci, G. Pittiglio, J. C. Norton, K. L. Obstein, and P. Valdastrì, “Adaptive Dynamic Control for Magnetically Actuated Medical Robots,” *IEEE Robot. Autom. Lett.*, vol. 4, no. 4, pp. 3633–3640, Oct. 2019, doi: 10.1109/LRA.2019.2928761.
- [36] J. C. Norton *et al.*, “Intelligent magnetic manipulation for gastrointestinal ultrasound,” *Sci. Robot.*, vol. 4, no. 31, pp. 1–14, 2019, doi: 10.1126/scirobotics.aav7725.
- [37] P. R. Slawinski, A. Z. Taddese, K. B. Musto, S. Sarker, P. Valdastrì, and K. L. Obstein, “Autonomously Controlled Magnetic Flexible Endoscope for Colon Exploration,” *Gastroenterology*, vol. 154, no. 6, pp. 1577–1579.e1, 2018, doi: 10.1053/j.gastro.2018.02.037.
- [38] S. Yim and M. Sitti, “Design and rolling locomotion of a magnetically actuated soft capsule endoscope,” *IEEE Trans. Robot.*, vol. 28, no. 1, pp. 183–194, 2012, doi: 10.1109/TRO.2011.2163861.
- [39] N. Li, D. Lin, J. Wu, Q. Gan, X. Hu, and N. Jiao, “Novel Concentric Magnetic Continuum Robot with Multiple Stiffness Modes for Potential Delivery of Nanomedicine,” *Magnetochemistry*, vol. 9, no. 129, 2023, doi: <https://doi.org/10.3390/magnetochemistry9050129>.
- [40] D. Lin, J. Wang, N. Jiao, Z. Wang, and L. Liu, “A Flexible Magnetically Controlled Continuum Robot Steering in the Enlarged Effective Workspace with Constraints for Retrograde Intrarenal Surgery,” *Adv. Intell. Syst.*, vol. 3, no. 10, p. 2000211, 2021, doi: 10.1002/aisy.202000211.
- [41] D. Lin, N. Jiao, Z. Wang, and L. Liu, “A Magnetic Continuum Robot with Multi-Mode Control Using Opposite-Magnetized Magnets,” *IEEE Robot. Autom. Lett.*, vol. 6, no. 2, pp.

-
- 2485–2492, 2021, doi: 10.1109/LRA.2021.3061376.
- [42] Z. Li and Q. Xu, “Design and Steering Control of a New Magnetic-Actuated Multi-Segment Robotic Catheter,” *2022 IEEE Int. Conf. Robot. Biomimetics, ROBIO 2022*, pp. 927–932, 2022, doi: 10.1109/ROBIO55434.2022.10011675.
- [43] M. H. D. Ansari *et al.*, “3D Printing of Small-Scale Soft Robots with Programmable Magnetization,” *Adv. Funct. Mater.*, vol. 33, no. 15, 2023, doi: 10.1002/adfm.202211918.
- [44] G. Pittiglio *et al.*, “Patient-Specific Magnetic Catheters for Atraumatic Autonomous Endoscopy,” *Soft Robot.*, vol. 9, no. 6, pp. 1120–1133, 2022, doi: 10.1089/soro.2021.0090.
- [45] Y. Kim, G. A. Parada, S. Liu, and X. Zhao, “Ferromagnetic soft continuum robots,” *Sci. Robot.*, vol. 4, no. 33, p. eaax7329, 2019, doi: 10.1126/scirobotics.aax7329.
- [46] P. Lloyd *et al.*, “Feasibility of Fiber Reinforcement Within Magnetically Actuated Soft Continuum Robots,” *Front. Robot. AI*, vol. 8, no. July, pp. 1–10, 2021, doi: 10.3389/frobt.2021.715662.
- [47] J. J. Abbott, E. Diller, and A. J. Petruska, “Magnetic Methods in Robotics,” *Robot. Auton. Syst.*, vol. 19, no. 4, 2019, doi: 10.1146/annurev-control-081219.
- [48] G. Pittiglio, M. Brockdorff, T. da Veiga, J. Davy, J. H. Chandler, and P. Valdastri, “Collaborative Magnetic Manipulation via Two Robotically Actuated Permanent Magnets,” *IEEE Trans. Robot.*, pp. 1–12, 2022, doi: 10.1109/TRO.2022.3209038.
- [49] Y. Kim *et al.*, “Telerobotic neurovascular interventions with magnetic manipulation,” *Sci. Robot.*, vol. 7, no. 65, 2022, doi: 10.1126/scirobotics.abg9907.
- [50] Y. Kim, H. Yuk, R. Zhao, S. A. Chester, and X. Zhao, “Printing ferromagnetic domains for untethered fast-transforming soft materials,” *Nature*, vol. 558, no. 7709, pp. 274–279, Jun. 2018, doi: 10.1038/s41586-018-0185-0.

-
- [51] G. Pittiglio *et al.*, “Personalized magnetic tentacles for targeted photothermal cancer therapy in peripheral lungs,” *Nat. Commun. Eng.*, vol. 2, no. 50, pp. 1–13, 2023, doi: 10.1038/s44172-023-00098-9.
- [52] P. Lloyd, G. Pittiglio, J. H. Chandler, and P. Valdastrì, “Optimal Design of Soft Continuum Magnetic Robots under Follow-the-leader Shape Forming Actuation,” in *International Symposium on Medical Robotics (ISMR)*, 2020, pp. 111–117. doi: 10.1109/ismr48331.2020.9312943.
- [53] J. Kaleta, M. Królewicz, and D. Lewandowski, “Magnetomechanical properties of anisotropic and isotropic magnetorheological composites with thermoplastic elastomer matrices,” *Smart Mater. Struct.*, vol. 20, no. 8, Aug. 2011, doi: 10.1088/0964-1726/20/8/085006.
- [54] M. Drahansky *et al.*, “Magnetorheological Elastomers: Materials and Applications,” *Intech*, vol. i, no. tourism, p. 13, 2016, doi: <http://dx.doi.org/10.5772/57353>.
- [55] Z. Li, Y. P. Lai, and E. Diller, “3D Printing of Multilayer Magnetic Miniature Soft Robots with Programmable Magnetization,” *Adv. I*, vol. 2300052, pp. 11–16, 2023, doi: 10.1002/aisy.202300052.
- [56] T. Xu, J. Zhang, M. Salehizadeh, O. Onaizah, and E. Diller, “Millimeter-scale flexible robots with programmable three-dimensional magnetization and motions,” *Sci. Robot.*, vol. 4, no. 29, 2019, doi: 10.1126/scirobotics.aav4494.
- [57] C. Chautems, B. Zeydan, S. Charreyron, G. Chatzipirpiridis, S. Pané, and B. J. Nelson, “Magnetically powered microrobots: A medicalrevolution underway?,” *Eur. J. Cardio-thoracic Surg.*, vol. 51, no. 3, pp. 405–407, 2017, doi: 10.1093/ejcts/ezw432.
- [58] Y. Tang, M. Li, T. Wang, X. Dong, W. Hu, and M. Sitti, “Wireless Miniature Magnetic

-
- Phase-Change Soft Actuators,” *Adv. Mater.*, vol. 34, no. 40, 2022, doi: 10.1002/adma.202204185.
- [59] X. Z. Chen *et al.*, “Recent developments in magnetically driven micro- and nanorobots,” *Appl. Mater. Today*, vol. 9 (37-40), 2017, doi: 10.1016/j.apmt.2017.04.006.
- [60] C. C. J. Alcântara *et al.*, “Mechanically interlocked 3D multi-material micromachines,” *Nat. Commun.*, vol. 11, no. 1, 2020, doi: 10.1038/s41467-020-19725-6.
- [61] H. Ceylan, J. Giltinan, K. Kozielski, and M. Sitti, “Mobile microrobots for bioengineering applications,” *Lab Chip*, vol. 17, no. 10, pp. 1705–1724, 2017, doi: 10.1039/c7lc00064b.
- [62] M. Salehizadeh and E. Diller, “Two-agent formation control of magnetic microrobots in two dimensions,” *J. Micro-Bio Robot.*, vol. 12, no. 1–4, pp. 9–19, 2017, doi: 10.1007/s12213-017-0095-5.
- [63] E. Diller, S. Floyd, C. Pawashe, and M. Sitti, “Control of multiple heterogeneous magnetic micro-robots on non-specialized surfaces,” *Proc. - IEEE Int. Conf. Robot. Autom.*, vol. 28, no. 1, pp. 115–120, 2011, doi: 10.1109/ICRA.2011.5979785.
- [64] S. Tottori, L. Zhang, K. E. Peyer, and B. J. Nelson, “Assembly, disassembly, and anomalous propulsion of microscopic helices,” *Nano Lett.*, vol. 13, no. 9, pp. 4263–4268, 2013, doi: 10.1021/nl402031t.
- [65] E. Diller, J. Giltinan, and M. Sitti, “Independent control of multiple magnetic microrobots in three dimensions,” *Int. J. Rob. Res.*, vol. 32, no. 5, pp. 614–631, 2013, doi: 10.1177/0278364913483183.
- [66] I. S. M. Khalil *et al.*, “Independent Actuation of Two-Tailed Microrobots,” *IEEE Robot. Autom. Lett.*, vol. 3, no. 3, pp. 1703–1710, 2018, doi: 10.1109/LRA.2018.2801793.
- [67] J. Giltinan, P. Katsamba, W. Wang, E. Lauga, and M. Sitti, “Selectively controlled magnetic

-
- microrobots with opposing helices,” *Appl. Phys. Lett.*, vol. 116, no. 13, 2020, doi: 10.1063/1.5143007.
- [68] P. Katsamba and E. Lauga, “Micro-Tug-of-War: A Selective Control Mechanism for Magnetic Swimmers,” *Phys. Rev. Appl.*, vol. 5, no. 6, 2016, doi: 10.1103/PhysRevApplied.5.064019.
- [69] S. Miyashita, E. Diller, and M. Sitti, “Two-dimensional magnetic micro-module reconfigurations based on inter-modular interactions,” *Int. J. Rob. Res.*, vol. 592, no. 32 (5), 2013, doi: 10.1177/0278364913479837.
- [70] M. Salehizadeh and E. Diller, “Optimization-Based Formation Control of Underactuated Magnetic Microrobots via Inter-Agent Forces,” in *International Conference on Manipulation, Automation and Robotics at Small Scales (MARSS)*, IEEE, 2017. doi: 10.1109/MARSS.2017.8001910.
- [71] J. Rahmer, C. Stehning, and B. Gleich, “Spatially selective remote magnetic actuation of identical helical micromachines,” *Sci. Robot.*, vol. 2, no. 3, pp. 1–10, 2017, doi: 10.1126/scirobotics.aal2845.
- [72] F. Ongaro, S. Pane, S. Scheggi, and S. Misra, “Design of an Electromagnetic Setup for Independent Three-Dimensional Control of Pairs of Identical and Nonidentical Microrobots,” *IEEE Trans. Robot.*, vol. 35, no. 1, pp. 174–183, 2019, doi: 10.1109/TRO.2018.2875393.
- [73] E. Diller, J. Giltinan, G. Z. Lum, Z. Ye, and M. Sitti, “Six-degree-of-freedom magnetic actuation for wireless microrobotics,” 2016, doi: 10.1177/0278364915583539.
- [74] S. Salmanipour and E. Diller, “Eight-degrees-of-freedom remote actuation of small magnetic mechanisms,” *Proc. - IEEE Int. Conf. Robot. Autom.*, pp. 3608–3613, 2018, doi:

10.1109/ICRA.2018.8461026.

Chapter 3 SMM Fabrication

3.1 Fabrication techniques

As described in Section 2.3, SMMs are composed of elastomeric base material mixed with magnetic component creating a smart magnetic material.

This section provides a description of methods utilized during my PhD for various SMMs designs, including details on mould design, techniques and assembly with functional components. Processes presented in this section contributed to the development of techniques further presented in Chapters 3-5.

Cost-effective and widely used fabrication methods in soft robotics, such as silicone casting and injection molding, offer flexibility in creating intricate designs, which is particularly important for components like pneumatic chambers. This project explored various fabrication methods for SMMs including injection moulding with parts printed with Fused Deposition Modeling (FDM) and Stereolithography (SLA) 3D printers. Molds were produced using an Ultimaker S5 (Ultimaker, NL) with 20-200 μ m layer resolution with 0.4 mm nozzle for FDM printing and a Form 3 printer with layer resolution of 25-100 μ m (Formlabs, USA) for SLA printing. Figure 2.1A shows examples of samples fabricated with FDM-printed parts (left) and SLA-printed parts (right).

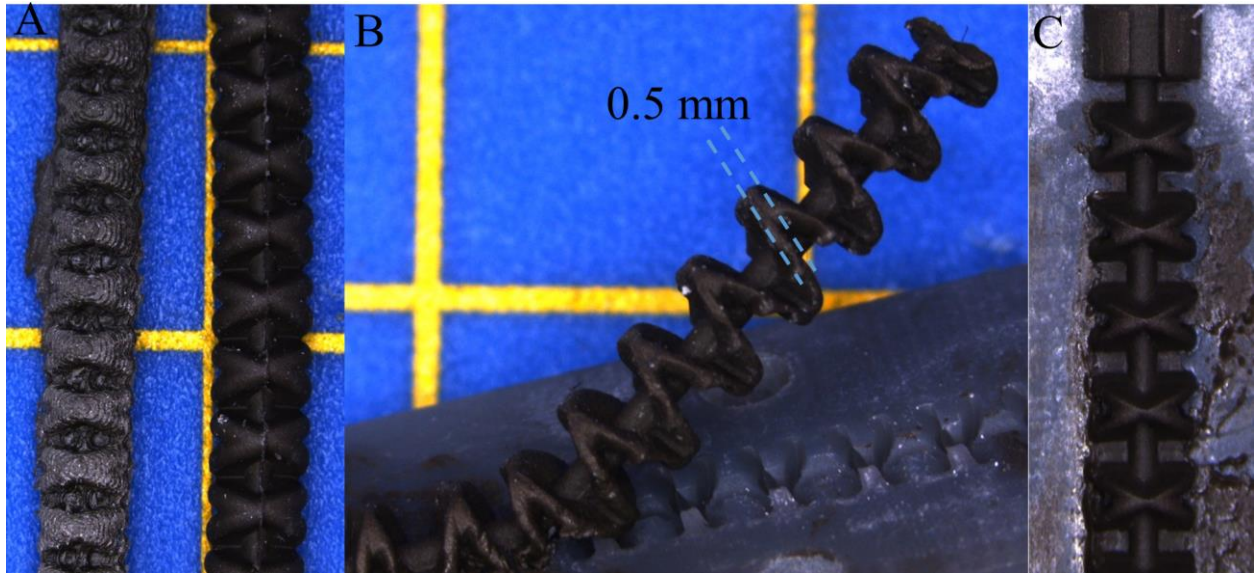


Figure 2.1. A. The difference between samples fabricated using FDM (Ultimaker S5) printed molds (left) vs using SLA printed parts (right). B and C. An example of molded double helix reinforced SMM using a mold printed with SLA printer (Form 3), showcasing detailed feature definition.

Depending on the required feature accuracy, both mould printing methods can be suitable for producing SMMs. The printer's resolution is an important factor to consider, however there are many factors that can affect the quality of the printed part, such as the specific design, size and depth of the features, as well as choosing the right layer thickness for designed feature size. Additionally, the quality of the moulded part is also affected by the specific materials used for printing and moulding. It is important to make sure that the material of the mould will not interfere with silicone curing.

Moulds created using FDM printing result in SMMs with grooves on their surface corresponding to the layers of the printed mold. This textured surface reduces contact with materials like silicone phantoms, which can help prevent sticking. A practical example is in pre-clinical testing with silicone phantoms, where adhesion and buckling at the interface between the sample and silicone can hinder smooth navigation. FDM-printed molds are particularly effective for fabricating relatively large structures (in the millimeter scale), as shown in Figure 2.2 [1], or for SMMs with cylindrical shapes, as seen in Figure 2.3 [2].

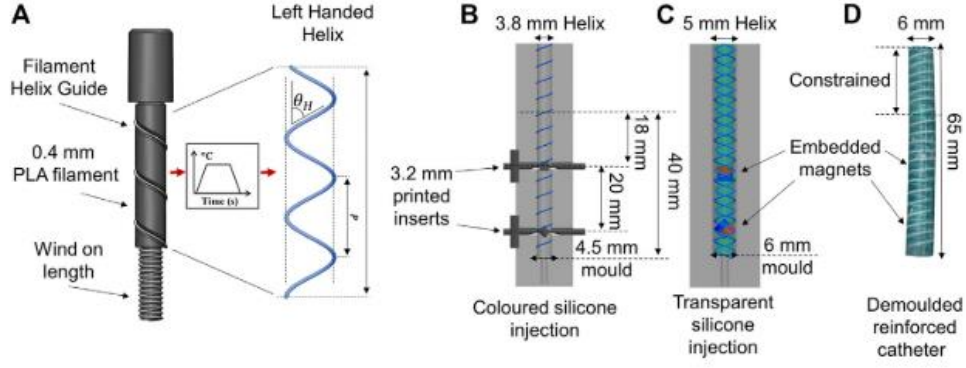


Figure 2.2. Example of a fabrication technique for a 6 mm SMM with FDM printed molds. Reproduced from [1]. | Fabrication process of the magnetic soft robot reinforced with two PLA helices. (A) Helix formation with a 0.4 mm PLA fiber at a fiber angle of θ_H . Helix pitch (P) is the parallel length of one complete turn. (B) Molding of tentacle core with inner helix and printed inserts to create magnet cavities, EcoFlex00-30 was injected into the mold and cured. (C) Magnets placed in cavities and outer, opposing helix secured around the tentacle core. EcoFlex00-30 injected into the mold and cured to create a 1.5 mm outer coating. (D) The demolded two segment tentacle featuring double helix reinforcing.

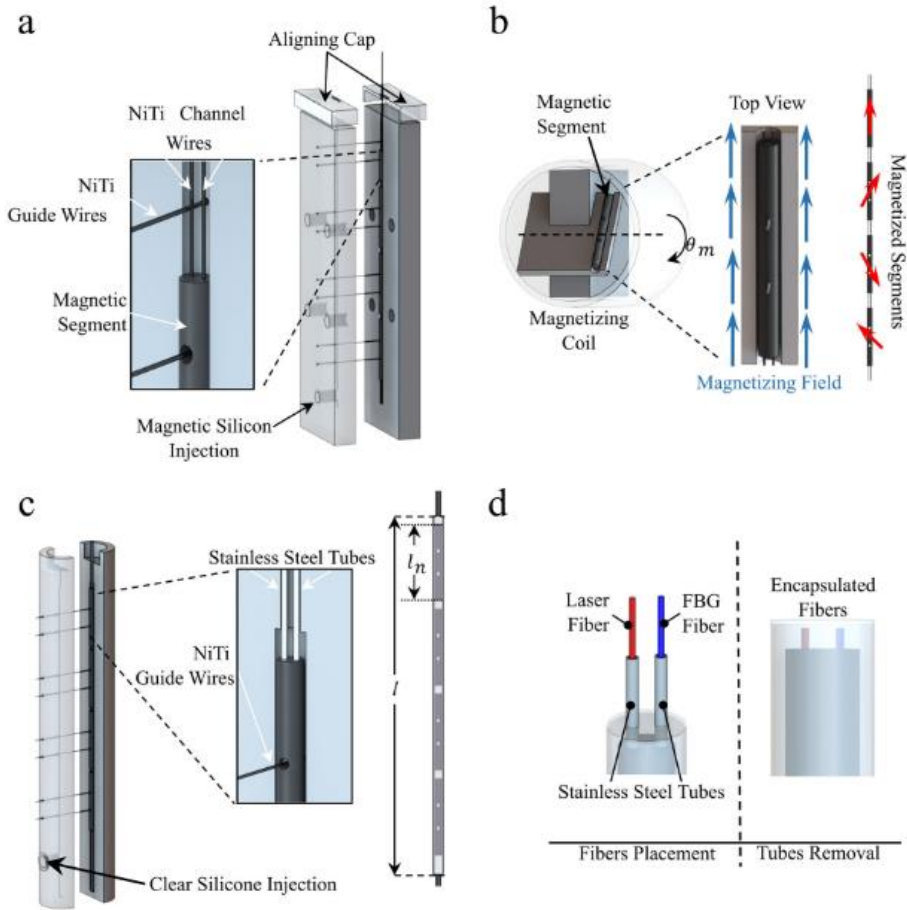


Figure 2.3. Example of fabrication technique of a cylindrical SMM with FDM printed mold. Reproduced from [2]. Fabrication of magnetic tentacles. (A) Molding of the four magnetic segments, utilizing NiTi wires as guides and for creating tool channels. (B) Segments magnetization, utilizing pulse magnetizer and 3D printer inserts to align each

segment in the coil of the magnetizer, according to the optimization algorithm. (C) Over-molding of magnetic segments for overall tentacle bonding, utilizing tool channels for placement of stainless-steel tubes to guide placement of the tools in the next step. (D) Placement of laser and FBG fibers within the tentacle after over-molding and removal of stainless-steel tubes.

However, the FDM technology is not always adequate for producing micro-scale features. For example, when designing a manipulator approximately 3 mm in diameter with features smaller than 1 mm, as discussed in Chapter 4, the moulds produced using the FDM printer lacked the quality necessary to capture the intricate details of the double helix designs described in Chapters 4 and 5, which were essential for the function of the designed SMMs. Furthermore, achieving the desired textured surface required adjusting printer's settings and increasing the layer thickness, which further compromised the detail of the features.

In contrast, SLA-printed molds provided satisfactory quality and a smooth surface finish for the fabricated parts. To ensure smooth navigation and minimize the risk of buckling on the non-textured surface, silicones initially used for prototyping from the EcoFlex range (shore hardness 00-10 to 00-30) were replaced with an elastomer of higher shore hardness (30A) from the DragonSkin range (Smooth-On). Additionally, applying talcum powder to the mold surface as a release agent provided several benefits, including easier demolding and enhanced detail in the molded features due to improved curing.

3.1.1 Instrumentation

Instrumenting magnetic catheters with surgical tools such as laser fibres, camera or sensors is crucial in the process of functionalizing soft robots to be used in medical procedures. One of the methods involves casting a tool channel. This works well in relatively large structures. However, in manipulators with few mm in diameter made of soft elastomers, this can be challenging due to

wires and fibers buckling and piercing through the SMM while passing the instruments through the elastomeric channel.

In terms of embedding tools permanently in the manipulator, the same problem occurs during the fabrication process when placing tools in the channel. It happens due to wires or fibers being stiff and often sharp (relatively to elastomer) at the tip and piercing through catheter's body. In [5] (Figure 2.3) this problem was solved by using stainless steel tubes to guide the placement of fibers to then remove the tubes leaving behind fibres embedded in the soft body. This method although proven successful in accurately placing two fibers in a 2.4 mm in diameter catheter, it consisted of multiple stages, making this process time consuming and complex. Therefore, for the next instrumentation project, I minimized the number of stages in the process. Using very soft and thin elastic tubing, with a shore hardness lower than the manipulator itself allowed to pass the fibers without piercing the material of the manipulator. The walls of the tubing provided structural integrity and smooth surface for the tools to glide through. Due to low shore hardness, the tubing did not affect the bending performance of the manipulator.

To embed a camera, due to its tip size (2mm OD) and larger connecting piece, it could not be passed through tubing in the manipulator. The wires of the camera were relatively low in stiffness in comparison to the DS 10 used for SMM body.

The camera manipulator was fabricated with a thin (300 micron) aluminum sheet that created a slit in the middle of the SMM body to fit in the camera lens with connecting wiring. The mould for this manipulator was designed with a cavity for a 2 mm camera lens. After the placement of the components, the manipulator was gently closed up with layer of Silpoxy (SmoothOn) brushed in the slit and left to cure.

[1] P. Lloyd et al., "Feasibility of Fiber Reinforcement Within Magnetically Actuated Soft

-
- Continuum Robots,” *Front. Robot. AI*, vol. 8, no. July, pp. 1–10, 2021, doi: 10.3389/frobt.2021.715662.
- [2] G. Pittiglio et al., “Personalized magnetic tentacles for targeted photothermal cancer therapy in peripheral lungs,” *Nat. Commun. Eng.*, vol. 2, no. 50, pp. 1–13, 2023, doi: 10.1038/s44172-023-00098-9.

Chapter 4 Independent SMM Actuation

Chapter source: Independently Actuated Soft Magnetic Manipulators for Bimanual Operations in Confined Anatomical Cavities, Z Koszowska, M Brockdorff, T da Veiga, G Pittiglio, P Lloyd, T Khan-White, R A Harris, J W Moor, J H Chandler, and P Valdastrì, *Adv. Intell. Syst.*, 6: 2300062.

<https://doi.org/10.1002/aisy.202300062>

Abstract

Soft magnetic manipulators offer the prospect of improved surgical outcomes through their potential for miniaturization and inherently safe tissue interaction. However, independent actuation of multiple manipulators within the same confined workspace is limited by undesired simultaneous actuation and manipulator-manipulator interactions. This study proposes, for the first time, approaches for the independent magnetic actuation of two magnetic continuum manipulators within the same confined workspace. A novel modular magnetic soft robot segment design is proposed with modified geometry to provide preferential bending planes and high angles of deflection. This design is integrated into two dual-segment magnetic manipulators which, when arranged in parallel, can deliver independent bending in two planes of motion. Two distinct independent control strategies are proposed, based on orthogonal manipulator magnetization profiles and local field gradient control respectively. Each dual-manipulator configuration was characterized over a sequence of applied magnetic fields and gradients, induced via a dual robotically controlled external permanent magnet system. Manipulator independence, bending range of motion and twisting behaviors were evaluated as a function of control strategy and manipulator separation distance.

To demonstrate the system’s potential in clinical scenarios, a dual-manipulator configuration was adapted to carry an endoscopic camera and optic fiber respectively. The resultant bimanual system was deployed in the confined anatomy of a skull-base phantom to simulate minimally invasive ablation of a pituitary adenoma. Independent motion of the camera and tool within the confined workspace demonstrate the potential for an independent magnetic tool manipulation for surgical applications.

4.1 Introduction

Modern surgical platforms such as the da Vinci (Intuitive Surgical da Vinci Surgical System, USA), Versius (Cambridge Medical Robotics, UK) leverage robotic assistance for the precision control of multiple straight, rigid instruments [1]. This approach has delivered a step change in the provision of many minimally invasive procedures and has set a precedent for robotics in surgery. Driven by the aim of delivering improvements to anatomical conformation, achievable workspace and surgical access requirements, numerous flexible continuum robotic devices have since been proposed [2]. Mechanically driven approaches have realized actuation via cables (Intuitive Surgical da Vinci Surgical System, USA), rods [3] or concentric tube interactions [4], with complete robotic platforms having been proposed to deliver bimanual operations within confined anatomy [5], [6]. Although sophisticated and effective approaches, integration of continuum tools based on mechanical assemblies of hard metallic structures imposes a reliance on the controller and/or operator to deliver safe (ideally contact free) tissue interaction during deployment and use; something exacerbated within confined anatomy.

As an inherently safer alternative to mechanically driven designs, soft bodied surgical robots have also been proposed [7]. Due to their high structural compliance (similar to that of soft tissues)

interaction forces are limited and passive anatomical conformation is possible. Soft robots intrinsically actuated via pneumatics [8], [9] or hydraulics [10] have proven successful for endoscopic applications. However, due to the requirement for onboard actuation chambers and tubing connections, scaling designs down comes at the cost of reducing controllable degrees of freedom. Through the use of remote actuation, Soft Magnetic Manipulators (SMMs) overcome this limitation, delivering virtually unlimited miniaturization potential without loss of controllable degrees of freedom [11]. SMMs maintain the advantages of a compliant structure and can be magnetically pre-programmed to produce desired deformations under the effect of controlled external magnetic fields [12]. These advantages have been demonstrated in a wide range of medical applications including cardiovascular [13], [14], bronchoscopic [15], pancreatic [16] and vasculature navigation [17]–[19].

Driven by the requirements of precision, miniaturization and delicate tissue interactions, SMMs represent a promising candidate for the evolution of robotic surgery in delicate confined anatomy. To date, SMMs have been investigated in single-manipulator set-ups mainly targeting endoluminal applications, precluding the delivery of multiple independent magnetic manipulators within a shared workspace. As endoscopic and laparoscopic procedures typically require multiple tools to be present at the operating site, systems providing solutions to independent SMM control would enable to expand the reach of magnetic approaches beyond endoluminal applications to bimanual surgical procedures. However, utilizing magnetic actuation strategies makes multi-tool set up challenging due to the complexity in achieving control independence over the magnetic agents. Considering two identical SMMs in a shared workspace, application of uniform magnetic field conditions would lead to the same motion for both agents.

Multi-agent magnetic control was investigated at the micro-scale for control of untethered mobile micro-robots, swimmers and spheres. Suggested approaches utilize geometric [20]–[24] or magnetic [25], [26] heterogeneity between agents, as well as inter-agent magnetic interaction [27], [28], leading to different responses under application of a uniform magnetic field. Other approaches exploit sophisticated magnetic control such as systems of electromagnetic coils [29] of which some enable generation of non-uniform magnetic fields [30] or achieve independence in actuation of multiple magnetic Degrees of Freedom (DoFs) [31], [32]. All presented research in the area of independent magnetic control has investigated untethered robots at micro-scale actuated in a fluid medium. The issue of independent control of continuum SMMs within a confined workspace remains an open challenge.

In the presented work, we investigate for the first time the concept of parallel bi-manual SMMs under independent magnetic control within a shared confined workspace, as depicted in Figure 4.1. We develop a modular monolithic double-helix SMM design that promotes bending within a desired plane through mechanical constraint. Manipulator designs capable of bi-plane bending are developed through serial stacking of the modular SMM design, and are arranged into parallel dual-manipulator configurations with separations between 2-4 cm. To deliver independent control we present and compare two distinct approaches, based on orthogonal SMM magnetization profiles and local field gradient control respectively. Each dual-manipulator configuration is characterized in terms of independent bending and twisting behaviors under applications of magnetic fields and field gradients, as generated using our dual robotically controlled External Permanent Magnet system (dEPM) [33]. Interaction forces between manipulators and their effect on desired poses are

considered for a range of workspace configurations, and we determine the minimum operational workspace possible for bimanual operation using the presented manipulators.

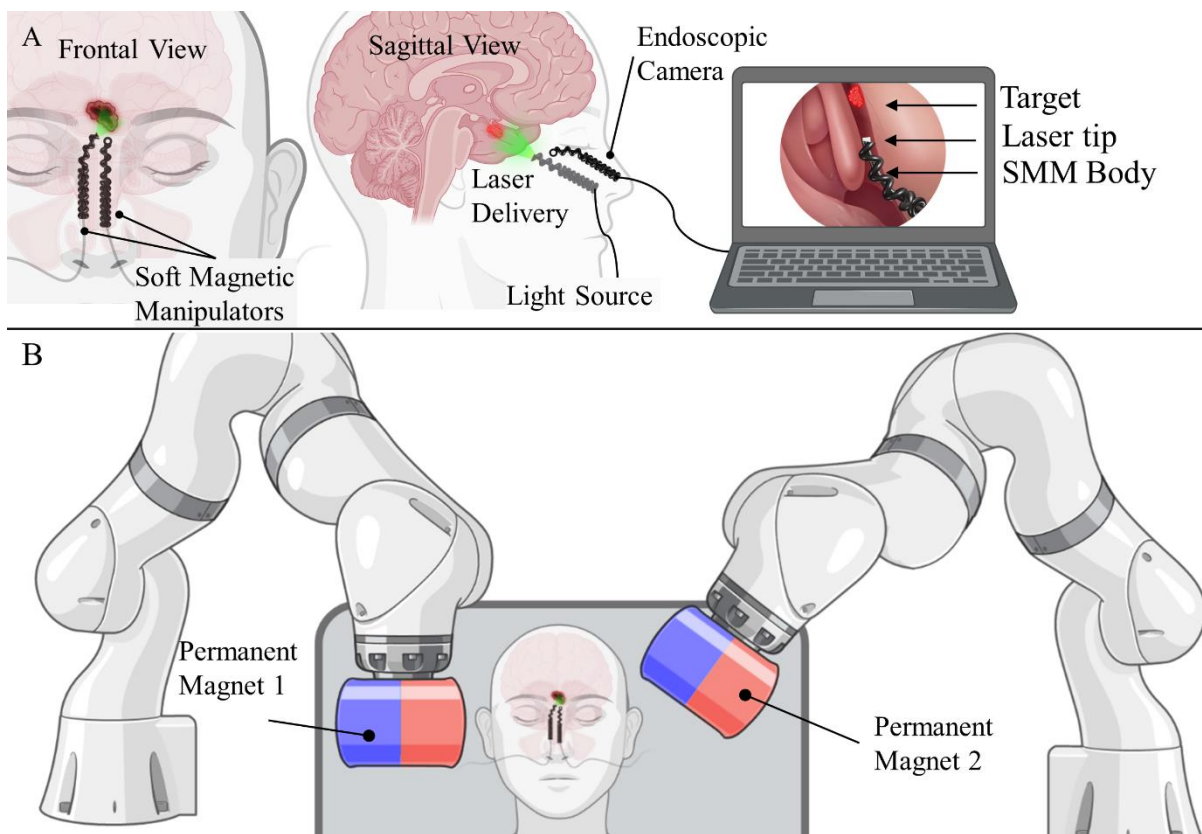


Figure 4.1. Overview of a magnetically actuated dual-manipulator set up. A. Actuated camera view – visible workspace and manipulator equipped with fiber. B. Proposed set up in an operating room, permanent magnets mounted on robotic arms for controlled field generation.

To demonstrate our bi-manual SMM system within a clinically relevant scenario, we consider the case of Endoscopic Endonasal Transsphenoidal (EET) procedures for surgical treatment of pituitary tumors (which account for up to 15% of all intracranial masses and exhibit an estimated prevalence of 17% within the general population [34]). EET procedures currently involve insertion of a slender rigid endoscope and surgical tools through the nostrils to access the base of the brain. Although offering advantages over access via craniotomy, risks of nasal septal perforation, impaired olfactory function and damage to nearby nerves and large blood vessels remain [35].

Many of these adverse outcomes are the result of manipulating multiple rigid instruments within the narrow, curved anatomy of the nasal cavity, and thus may be mitigated through the use of soft, compliant tools. Through configuration of our dual-manipulators to carry an endoscopic camera and optic fiber respectively, we present a concept of bimanual multi-tool magnetically actuated robotic system for minimally invasive ablation of a pituitary adenoma. We present independent motion of the camera and optic fiber within an anatomically accurate skull base phantom with simulated tumor, demonstrating for the first time the potential for independent magnetic tool manipulation within confined anatomy.

4.2 Results

Neglecting interaction forces between multiple SMMs, designs with equal magnetization profiles and controlled within a shared homogeneous magnetic field, will produce identical actuation outcomes. Independent control is possible through deployment of sophisticated magnetic field actuation (fields and gradients), and/or via optimization of the geometric or material properties of each SMM. The following considers the magnetic actuation principles involved in manipulator control to develop a modular geometric SMM segment design approach that promotes uniplanar bending. A multi-segment integration is subsequently presented based on this design, and coupled with magnetic field and gradient control strategies, enabled via the dEPM system, to promote independent control for application suitability.

4.2.1 Principle of Magnetic Actuation

A magnetic element with magnetization μ is subject to magnetic force \mathbf{f} and torque $\boldsymbol{\tau}$, under an applied field \mathbf{B} respectively as

$$\mathbf{f}(\mathbf{p}) = \nabla (\boldsymbol{\mu} \cdot \mathbf{B}(\mathbf{p})) \quad (4.1)$$

$$\boldsymbol{\tau}(\mathbf{p}) = \boldsymbol{\mu} \times \mathbf{B}(\mathbf{p}) \quad (4.2)$$

At position $\mathbf{p} \in R^3$ in space, where \mathbf{p} is referred to as the focal point, or the point in the workspace where we aim to control a specific field and gradient. Lower case bold letters represent vectors (e.g., $\mathbf{v} = [v_x \ v_y \ v_z]^T$) and the gradient operator ∇ represents partial derivatives in each of the three basis directions in the form $\nabla = \left[\frac{\partial}{\partial x} \ \frac{\partial}{\partial y} \ \frac{\partial}{\partial z} \right]^T$. Magnetic gradients allow for the generation of force, while magnetic field misalignments generate torques on a magnetic element. Considering a workspace with x, y and z axes, equations (4.1) and (4.2) could be further expanded as

$$\mathbf{f}(\mathbf{p}) = \begin{bmatrix} f_x \\ f_y \\ f_z \end{bmatrix} = \begin{bmatrix} \mu_x & \mu_y & \mu_z & 0 & 0 \\ 0 & \mu_x & 0 & \mu_y & \mu_z \\ -\mu_z & 0 & \mu_x & -\mu_z & \mu_y \end{bmatrix} \begin{bmatrix} \frac{\partial B_x(\mathbf{p})}{\partial x} \\ \frac{\partial B_x(\mathbf{p})}{\partial y} \\ \frac{\partial B_x(\mathbf{p})}{\partial z} \\ \frac{\partial B_y(\mathbf{p})}{\partial x} \\ \frac{\partial B_y(\mathbf{p})}{\partial y} \\ \frac{\partial B_y(\mathbf{p})}{\partial z} \end{bmatrix} \quad (4.3)$$

$$\boldsymbol{\tau}(\mathbf{p}) = \begin{bmatrix} \tau_x \\ \tau_y \\ \tau_z \end{bmatrix} = \begin{bmatrix} 0 & -\mu_z & \mu_y \\ \mu_z & 0 & -\mu_x \\ -\mu_y & \mu_x & 0 \end{bmatrix} \begin{bmatrix} B_x(\mathbf{p}) \\ B_y(\mathbf{p}) \\ B_z(\mathbf{p}) \end{bmatrix} \quad (4.4)$$

Magnetic actuation through the use of two external permanent magnets, such as the dEPM platform [33], allows for individual control of magnetically induced forces and torques on magnetic objects. Pittiglio et al. [33] showed how the dEPM platform could be used to independently control the wrench of a magnetic object. This was done by using homogenous fields to control the torque and

linear gradients to control the forces. In this study we propose an alternative method to generate magnetic torques in addition to using homogenous fields.

Consider that the general field at point \mathbf{p} can be expressed as

$$\mathbf{B}(\mathbf{p}) = \mathbf{B}(\mathbf{p}_o) + \frac{\partial \mathbf{B}(\mathbf{p})}{\partial \mathbf{p}} (\mathbf{p} - \mathbf{p}_o) \quad (4.5)$$

where \mathbf{p}_o is a position at a distance $\mathbf{r} \in \mathbb{R}^3$ away from \mathbf{p} . This is the center of the gradient, where the field changes its polarity. When $\mathbf{p} = \mathbf{p}_o$ and applying only linear gradients, the field at position \mathbf{p} is equal to 0. When $\mathbf{p} \neq \mathbf{p}_o$, a magnetic gradient is centered \mathbf{p}_o , while the object we aim to control is at the focal point \mathbf{p} . Therefore, at \mathbf{p} both, magnetic field and gradient, will be present. This equation is valid under the assumption that the gradient is constant over the workspace, that the divergence and curl of the magnetic field is zero and that we are operating in a current-free workspace.

Under these magnetic conditions, a magnetic agent such as a SMM with appropriate mechanical and magnetic design, could be manufactured to only exhibit torque when presented with certain combinations of magnetic fields and gradients simultaneously.

4.3 Segment Design

To balance the requirements for miniaturization, tool integration and high bending-to-torsional stiffness, a monolithic (single material) design consisting of a soft magnetic double helix wrapped around a soft magnetic core is proposed, Figure 4.2. The design aims to deliver variation in bending stiffness between the two bending planes (XZ and YZ), as depicted in Figure 4.2. The seam of the double helix intersecting points creates planar reinforcement, leading to significantly increased

bending stiffness along the XZ plane. Constraining the motion of the SMM in this way allows for separation of actuation planes for segments arranged orthogonally in series (Figure 4.2C), as required for independent control.

We explore two different designs of the double helix structure, investigating its effect on the stiffness in XZ and YZ planes of the manipulator. The helical thickness (h) and the number of helical revolutions per unit length (R) are chosen as variables in this study. The increase in R (symmetrically for left and right-handed helix) adds more intersecting points along the length, therefore increases stiffness along the XZ plane. The decrease in helical thickness, however, is expected to promote bending in YZ plane. Therefore, in this study we consider two designs with different h values, where both designs are characterized with maximum R (where further increase of this parameter would not create a double helix structure but a cylinder). Both designs are fabricated with an outer diameter of 3.5 mm, considering endonasal application, and inner diameter of 1 mm for incorporating an internal tool channel for further instrumentation of the manipulator. Two single-segment candidate SMM designs were evaluated in terms of their bending and twisting capacity in comparison to a baseline cylindrical SMM, in accordance with parameters presented in Table 1.

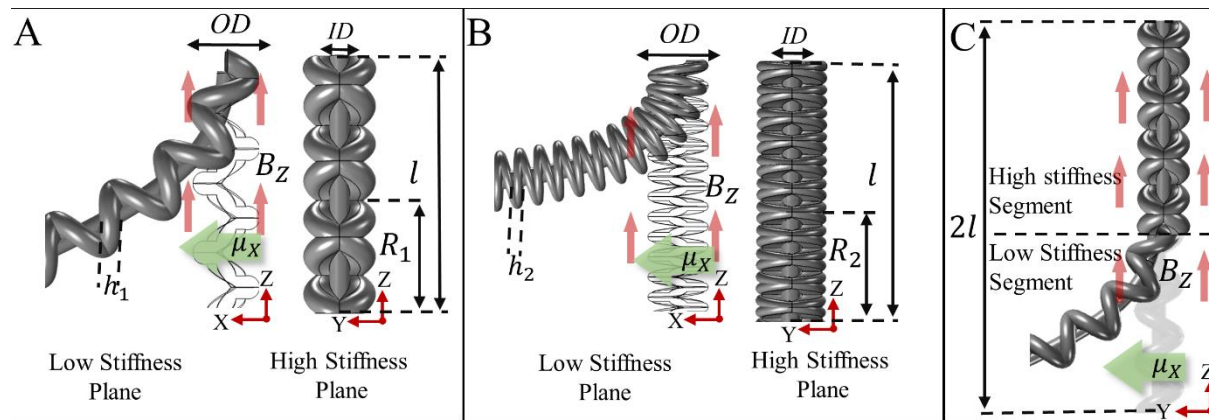


Figure 4.2. Examples of monolithic reinforcement designs, where h is the thickness

of the helical structure, R is number of revolutions per unit length, OD is outer diameter and ID the inner diameter, l is segment length, μ is magnetization direction and B_z applied field direction. (A) represents two orthogonal projections of design low density SMM, showcasing characteristic variety of the manipulator between YZ and XZ planes. (B) represents high density SMM. (C) shows an example of a two-segment manipulator using a low density SMM design.

Table 4.1. Design Parameters for tested designs of magnetic manipulators.

Design	OD (mm)	ID (mm)	L (mm)	R	h (mm)	w (mm)
Cylinder	3.5	<i>N/A</i>	20	<i>N/A</i>	<i>N/A</i>	<i>N/A</i>
Low Density SMM	3.5	1	20	5.5	1.5	1.25
High Density SMM	3.5	1	20	16	0.5	1.25

4.3.1 Segment Fabrication

Candidate helical designs and a cylinder (Table 4.1) were fabricated by casting with 3D printed molds (Grey V4 resin, Form III, Formlabs, USA). Silicone (Dragon Skin™ 10 ,Smooth-On, Inc., U.S.A.) was mixed with 100 wt% (percentage by weight) of hard magnetic microparticles (Nd-FeB with an average 5 μm diameter, MQFP-B+, Magnequench GmnH, Germany). The magnetic slurry was then mixed in a high vacuum mixer (ARV- 310, THINKYMIXER, Japan) for 90 seconds at a speed of 1400 rpm and a pressure of 20.0 kPa. The degassed slurry was injected into closed molds and cured at 45°C for 30 minutes.

Each design was fabricated twice to be magnetized in two directions for testing: along their X and Y axes, respectively, allowing for comparison of stiffness variability between the axes. The

monolithic approach is fully soft and can be miniaturized further for access to the narrowest anatomical features.

4.3.2 Segment Design Evaluation

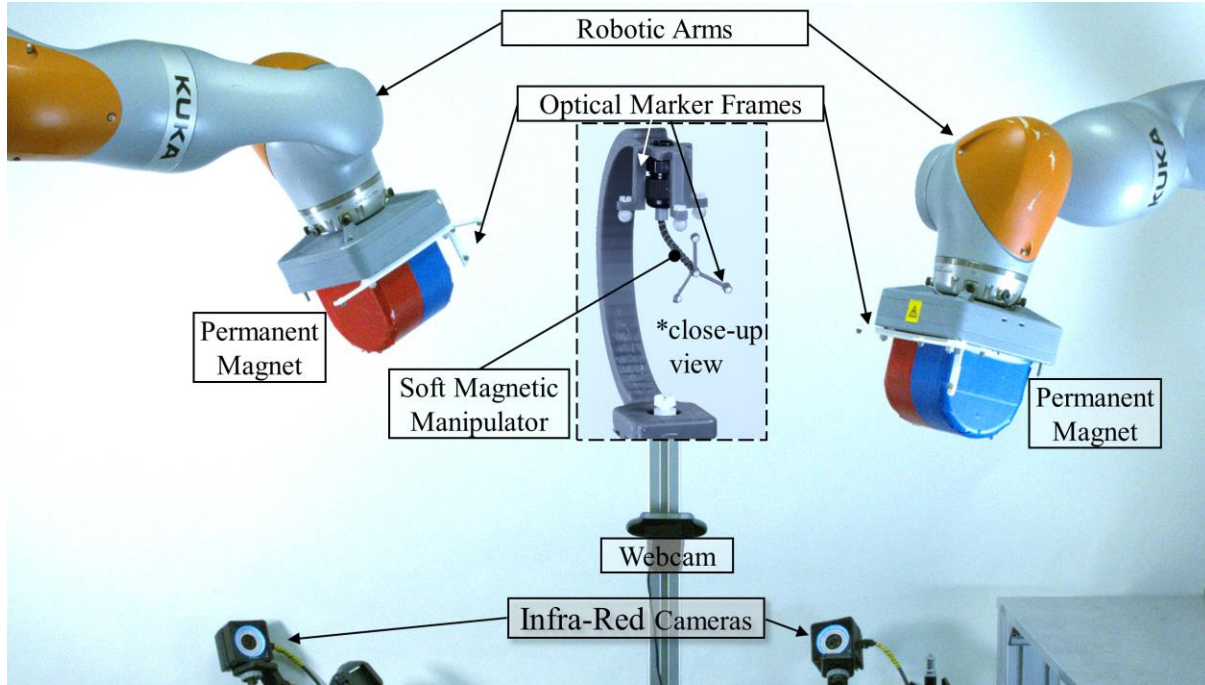


Figure 4.3. Experimental set-up including dual External Permanent Magnet (dEPM) platform, infra-red cameras and Soft Magnetic Manipulator (SMM) with optical marker frame at the base and tip.

To understand the mechanical stability of the designs and the maximum expected bending under varying field conditions, fabricated designs magnetized in X and Y axes (Figure 4.2) were evaluated by recording manipulator deformation under application of homogenous magnetic field conditions as detailed in Table 4.2.

Table 4.2. Magnetic field conditions in time applied during testing of three candidate designs in dEPM platform.

Time	0 s - 20 s	20 s - 40 s	40 – 60 s	60 – 80 s	80 – 100 s	100 – 120 s
Field Direction (10 mT)	X	-X	Z	-Z	Y	-Y

To generate homogeneous magnetic fields, the robotic arms of the dEPM system (Figure 4.3) positioned two external permanent magnets (101.6 mm x 101.6 mm) symmetrically with respect to each other and the sample's workspace. The experimental set up also included four Optitrack (OptiTrack, NaturalPoint, Inc., USA) infra-red cameras for 3D motion tracking and for calibration of magnets in space. The tip poses of manipulators were recorded via the optical tracking system through optical markers attached to the manipulator during testing. Bending angles around X, Y (γ_x and γ_y , respectively) and the torsional rotation angle around Z (γ_z) were computed from the rigid body rotations of the marker frame (0.33 g). Since we aim at minimizing torsion (γ_z) with respect to bending (γ_x and γ_y), we consider ratio:

$$\rho_x = \frac{\gamma_x}{\max \gamma_z}; \rho_y = \frac{\gamma_y}{\max \gamma_z} \quad (6)$$

where ρ_x corresponds to the low stiffness axis (Figure 4.4A) and ρ_y to the high stiffness axis (Figure 4.4B). For an ideal design, the ratio ρ_y would be lower than ρ_x as this implies a desired difference in bending response between XZ and YZ planes.

Analyzing bending behavior in both directions is motivated by the objective of maximizing the bending angle of a manipulator on one plane, while providing stability on the other.

In Figure 4.4A, low density SMM shows a greater ratio ρ_x than a cylinder of the same diameter. In addition, in Figure 4.4A, the ratio ρ_x value for high density SMM is lower than the value for both cylinder and low density SMM. In Figure 4.4B, cylindrical SMM shows the highest ratio ρ_y of all three samples. However, when analyzing both plots, only the low density SMM shows the desired behavior in both magnetization cases. In the case of magnetization along X axis, the optimal design is expected to have the high ratio ρ_x and relatively low ratio ρ_y .

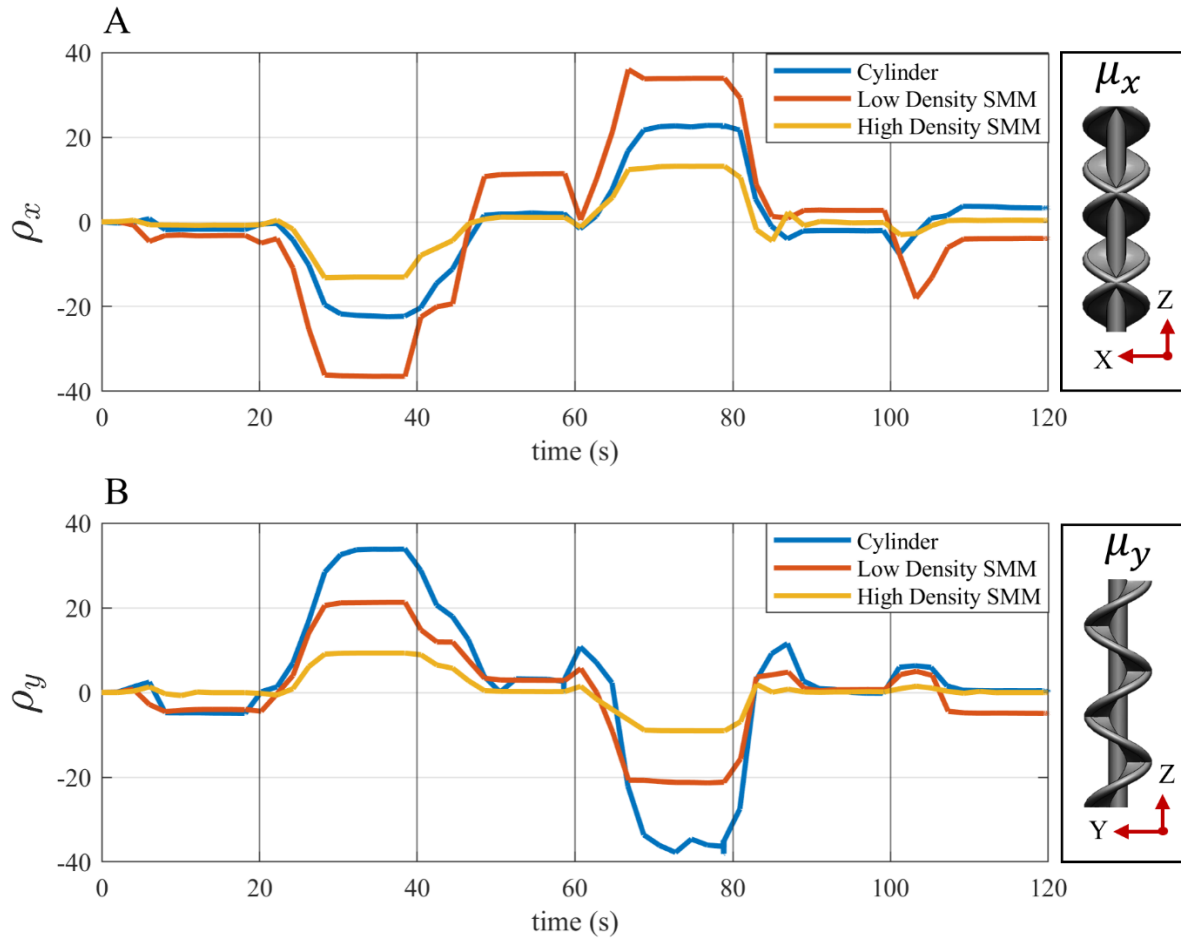


Figure. 4.4 Results of testing three candidate designs under varied magnetic field conditions as a ratio of deflection to torsion. A. Ratio of deflection about Y axis to torsion for SMMs magnetized in X direction. B. Ratio of deflection about X axis to torsion for samples magnetized in Y direction.

The collected results confirm that both structurally modified designs experience higher bending angle in YZ under a directionally varied 10 mT field, with respect to a cylinder. The XZ plane in

the design concept is constrained by overlapping helices, creating a planar reinforcement. This provides increased stiffness in that plane, leading to reduced bending under the same actuating field, in comparison to YZ plane. Therefore, the bending performance of designs with a double helix feature is better than that of a typical cylindrical SMM.

Based on the analysis of experimental data, the low density SMM presents the most suitable candidate for the objective of maximized bending in YZ plane and increased stiffness in XZ plane and was thus utilized for integration into more complex multi-segment designs.

4.4 Modular Design for Independent Control

The double helix SMM segment design promotes bending motion of the manipulator in one axes. Combining segments in series and in orthogonal direction allows for enhanced separation of bending primitives under independent segment actuation (Figure 4.2C, Figure 4.5C).

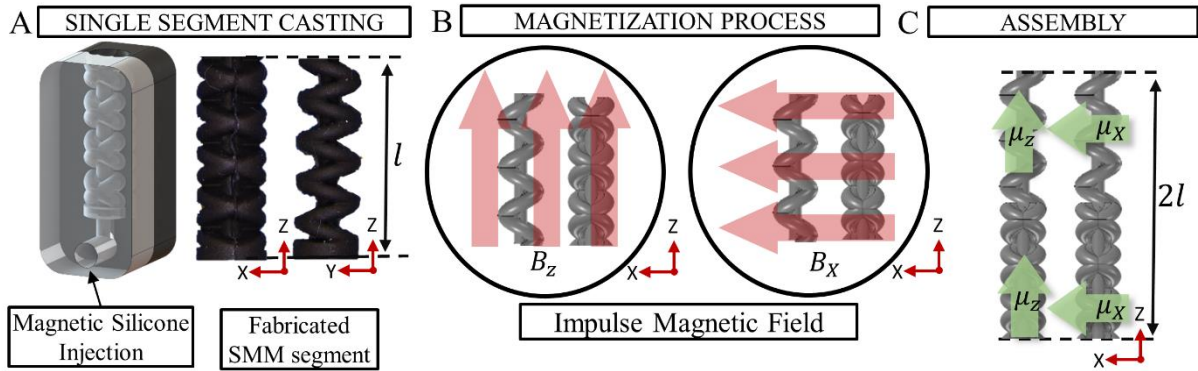


Figure 4.5. Fabrication process of SMMs. A. Single segment casting. B. Magnetization process of segments along their Z and X axes. C. An example of magnetized and assembled dual-segment manipulators.

To realize independent actuation of multiple segments in the same workspace, specific combinations of magnetization profiles and actuating fields are required. As depicted in the Figure

4.5, we propose to achieve this using a modular design with two manipulators in parallel (four SMM segments in total). Two strategies for independent control of the two manipulators within the same confined workspace are proposed, as depicted in Figure 4.6 and 4.7 respectively. The first, Orthogonal Magnetization (OM) strategy (Figure 4.6), utilizes segments with both axial and non-axial magnetic moments in conjunction with either applied homogenous fields or linear field gradients. This is based on Pittiglio et. al [33] , where it is shown that when considering multiple magnetic objects, each having their own magnetization μ , maximum independent DoF control is achieved when the dipole direction of the two magnetic agents is orthogonal.

The second is referred to as, Parallel Magnetization (PM) strategy (Figure 4.7) and employs axially magnetized segments in conjunction with magnetic gradients only, as detailed below.

4.4.1 Orthogonal Magnetization Strategy

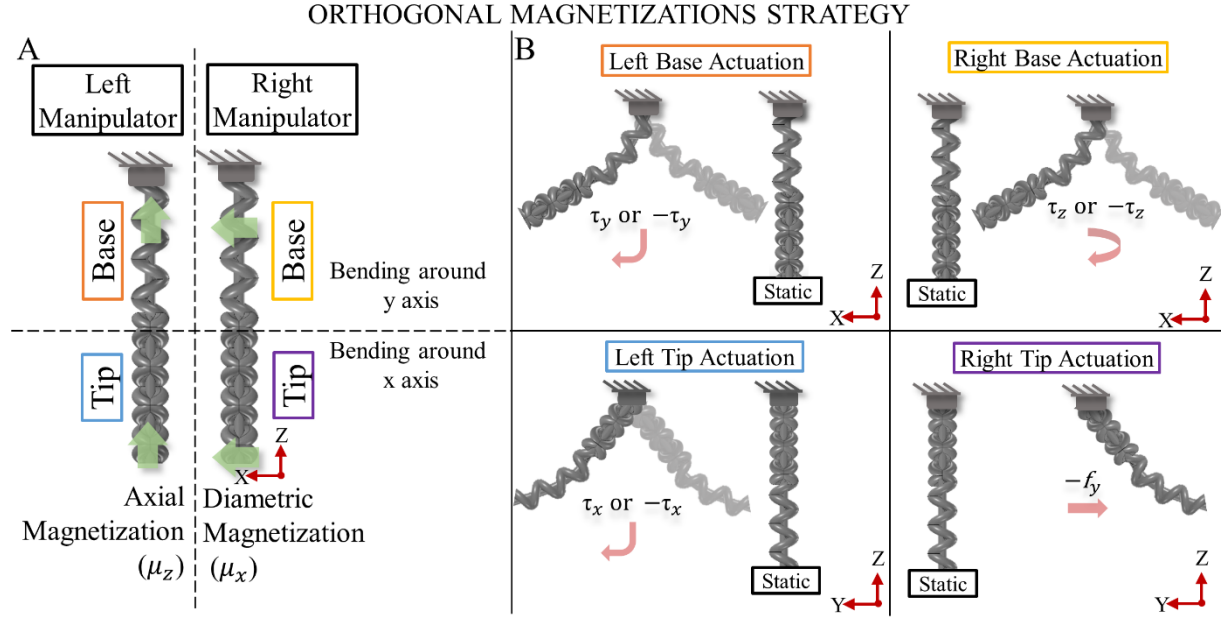


Figure 4.6. A case of two manipulators magnetized orthogonally; A. Left Manipulator (base and tip) magnetized along its main axis (Z). Right Manipulator (base and tip) magnetized along its X axis. B. Representation of available DoFs in this configuration and wrenches needed to actuate each segment.

In the OM strategy, the left manipulator base and tip segments, SMM_{LB} and SMM_{LT} respectively, are magnetized along the z-axis ($\mu_{SMM_{LB}} = \mu_{SMM_{LT}} = \mu_z$), while for the right manipulator the base and tip segments, SMM_{RB} and SMM_{RT} respectively, are magnetized along the x-axis ($\mu_{SMM_{RB}} = \mu_{SMM_{RT}} = \mu_x$), see Figure 4.6A. The required magnetic fields and gradients for independent control of each manipulator were determined based on Equation (4.5), and reported in Table 4.3. Figure 4.6B showcases bending modalities of segments and required wrenches for each motion. Analysis of Table 4.3 shows that while moving the left manipulator along the y-axis, an undesired rotation of the right manipulator around the Z axis occurs. Further analysis of this phenomenon is discussed in section 2.3.3.

Table 4.3. Wrench applied on agents 1 and 2 under applied field and gradients and their bending response in Orthogonal Magnetization case.

		Wrench applied on agent		Direction of Bending	
		Left Manipulator	Right Manipulator	Left Manipulator	Right Manipulator
Fields and Gradients	B_x	τ_y	0	+ x axis	None
	$-B_x$	$-\tau_y$	0	- x axis	None
	B_y	$-\tau_x$	τ_z	- y axis	τ_z
	$-B_y$	τ_x	$-\tau_z$	+ y axis	$-\tau_z$
	B_z	0	$-\tau_y$	None	- x axis
	$-B_z$	0	τ_y	None	+ x axis
	$\frac{\partial B_x}{\partial y}$	0	f_y	None	+ y axis
	$-\frac{\partial B_x}{\partial y}$	0	$-f_y$	None	- y axis

4.4.2 Parallel Magnetization Strategy

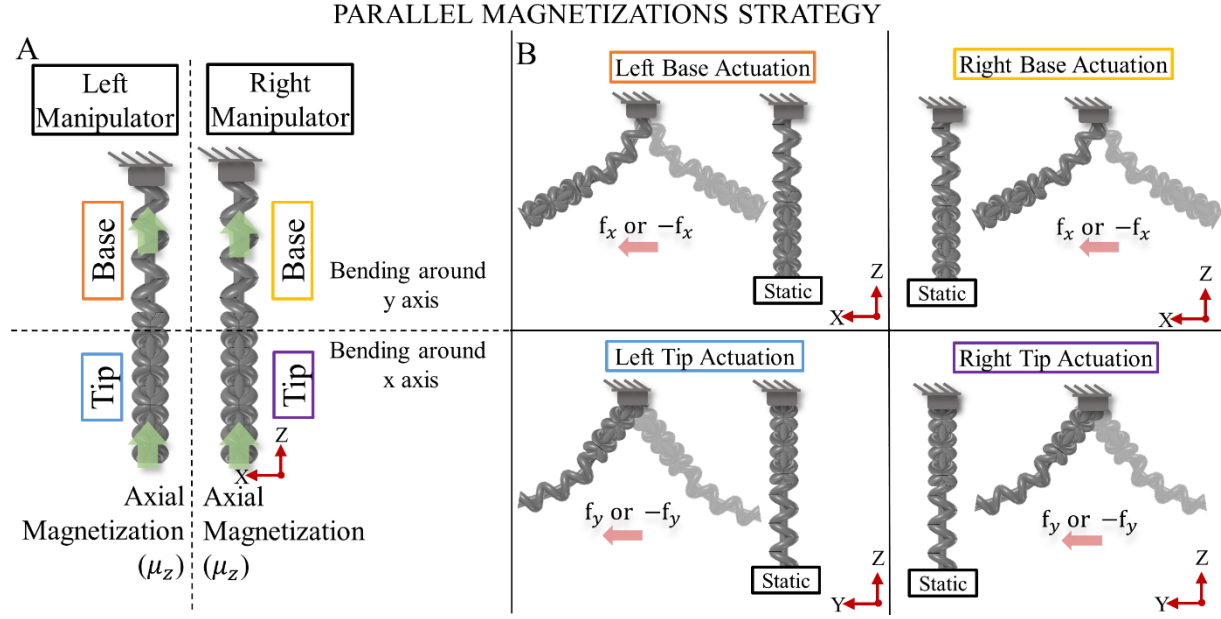


Figure 4.7. A case of two manipulators magnetized axially; A. Left and Right Manipulators (base and tip) magnetized along its main axis Z. B. Representation of available DOFs in this configuration and wrenches needed to actuate each segment.

Another method to independently control two SMMs could be achieved by using the actuation method proposed previously in section 2.1. In this scenario a magnetic gradient is applied at position \mathbf{p}_o . The magnetic actuation at position \mathbf{p} will be equal to the magnetic gradient applied at \mathbf{p}_o as well as an induced magnetic field as described by Equation (4.6). This method allows for independent control between two manipulators, by setting \mathbf{p}_o to the position of the static SMM (depicted at ‘static’ in Figure 4.7B), and \mathbf{p} to the position of the SMM that is meant to be actuated in a given case.

Unlike when using homogenous fields to control the torque, with this method we can achieve independent control of the SMMs regardless of the magnetization profile of the ‘static’ SMM. This is because keeping the SMM stationary relies on having no field present at the position of the

stationary SMM. This is in contrast to using homogenous fields, where in order for the SMM not to exhibit any torque, its magnetization must be aligned with applied magnetic field direction.

To evaluate this strategy, two SMMs were magnetized along Z axis ($\mu_{SMM_{LB}} = \mu_{SMM_{LT}} = \mu_{SMM_{RB}} = \mu_{SMM_{RT}} = \mu_z$), see Figure 4.7A. The distance γ is set to the distance between the two SMMs, such that $\gamma = [0 \quad D \quad 0]^T$. Table 4 shows the magnetic field and gradient applied to independently control the two SMMs, along with the focal point selected.

It is evident that when controlling either manipulator to bend along the Y axis, the applied gradient also causes a force along Z axis on both manipulators. However, this force is much smaller than the desired torque and thus may be considered to have negligible influence on the resultant manipulator motion. The resultant direction of bending for the proposed applied field gradients is summarized in Table 4.4.

Table 4.4. Wrench applied on left and right manipulators under applied gradients and their bending response with the Parallel Magnetization strategy.

		Focal Point	Wrench applied on agent		Direction of Bending	
			Left Manipulator	Right Manipulator	Left Manipulator	Right Manipulator
Fields and Gradients	$\frac{\partial B_x}{\partial y}$	p_2	τ_y	0	+ x axis	None
	$-\frac{\partial B_x}{\partial y}$	p_2	$-\tau_y$	0	- x axis	None
	$\frac{\partial B_y}{\partial y}$	p_2	$-f_z - \tau_x$	$-f_z$	- y axis and pulled downwards	Pulled downwards

	$-\frac{\partial B_y}{\partial y}$	p_2	$f_z + \tau_x$	f_z	+ y axis and pushed upwards	Pushed upwards
	$\frac{\partial B_x}{\partial y}$	p_1	0	τ_y	None	+ x axis
	$-\frac{\partial B_x}{\partial y}$	p_1	0	$\tau -_y$	None	- x axis
	$\frac{\partial B_y}{\partial y}$	p_1	$-f_z$	$-f_z - \tau_x$	Pulled downwards	- y axis and pulled downwards
	$-\frac{\partial B_y}{\partial y}$	p_1	f_z	$f_z + \tau_x$	Pushed upwards	+ y axis and pushed upwards

4.4.3 Independent Control Characterization

The motion independence of the parallel multi-segment designs (Figure 4.6 and Figure 4.7) was initially evaluated through testing with the dEPM platform. As well as motion independence, the tests also evaluated the maximum achievable range of motion and the smallest possible distance between the two manipulators before magnetic self-attraction causes adherence, an inherent risk with mechanically independent magnetized elements. The testing protocol was repeated for the OM and PM strategies to allow direct comparison between the two.

For each experiment, the two manipulators under test were positioned within the magnetic workspace with a separation distance D , in mechanical configurations as shown in Figure 4.8. An

optical tracking system (OptiTrack, NaturalPoint, USA) was used to track the tip position and orientation of both manipulators at all times. The frames with optical markers weigh 0.27 g and 0.17 g for left and right manipulator, respectively. For the OM manipulators, magnetic fields identified in Table 5 were applied in sequence to actuate segments SMM_{LB} , SMM_{LT} , SMM_{RB} , SMM_{RT} consecutively. This actuation process was repeated for decreasing separation distances D ranging from 4 cm to 2 cm in steps of 0.5 cm. This testing process was repeated for the PM manipulators through sequential application of the field gradients identified in Table 4.6.

Table 4.5. Conditions of magnetic fields, their direction and magnitude applied in experiments for Orthogonal Magnetization strategy.

	Direction of Bending	Magnetic Field Conditions (mT and mT/m)
Left Manipulator	-x; x	$Bx = [-3; -4; -5; -6; -7; 3; 4; 5; 6; 7]$
	-y; y	$By = [-3; -4; -5; -6; -7; 3; 4; 5; 6; 7]$
Right Manipulator	-x; x	$Bz = [-3; -4; -5; -6; -7; 3; 4; 5; 6; 7]$
	-y	$dBx/dy = [-50; -75; -100; -125; -150]$
	y	$dBx/dy = [50; 75; 100; 125; 150]$

Table 4.6. Conditions of magnetic field gradients, their direction and magnitude applied in experiments for Parallel Magnetization strategy.

	Direction of Bending	Magnetic Field Conditions (mT/m)
Left Manipulator	-x, x	$dBx/y = [-50; -75; -100; -125; -150; 50; 75; 100; 125; 150]$
	-y; y	$dBx/y = [-50; -75; -100; -125; -150; 50; 75; 100; 125; 150]$
Right Manipulator	-x, x	$dBx/y = [-50; -75; -100; -125; -150; 50; 75; 100; 125; 150]$
	-y, y	$dBx/y = [-50; -75; -100; -125; -150; 50; 75; 100; 125; 150]$

The tracked tip positions for the two manipulators during sequential field and/or gradient application for the OM and PM strategies are shown in Figure 4.9 and 4.10 respectively. The data

illustrate that a level of independent motion is achievable using the two control strategies at a range of separation distances. Undesired manipulator motions (those recorded on the un-actuated manipulator) are also present and show dependence on control strategy, actuated DoF and separation distance. These motions are induced through a combination of influence from the applied field (cross-activation) and through magnetic interaction between manipulators (cross-talk). The latter may extend to a failure point, defined as the minimum distance D between the two manipulators at which the attraction force between them cannot be overcome by the application of fields or gradients. It is apparent from the manipulator motions (Figure 4.8) that as separation distance D is reduced, the cross-talk influence increases (even prior to reach the failure point). This is most apparent for actuation scenarios where manipulators bend towards each other, thus temporarily reducing their effective separation distance and increasing cross-talk.

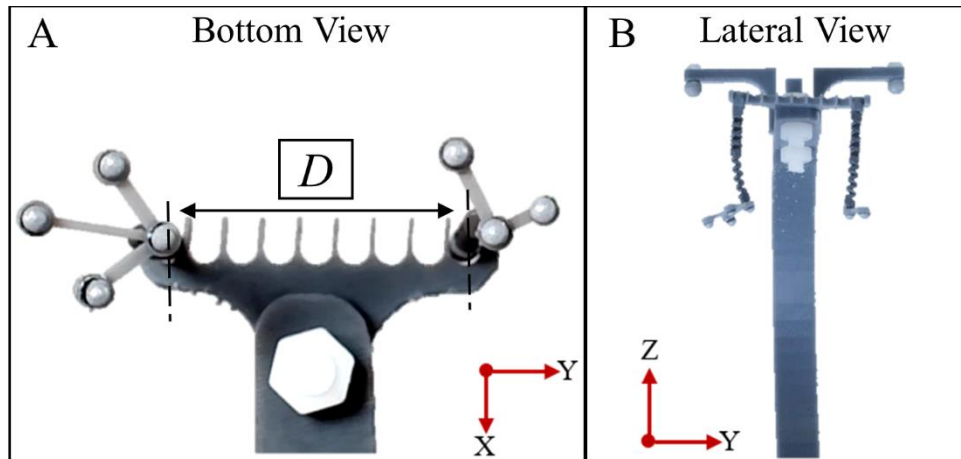


Figure 4.8. Experimental set-up; A. Bottom view of SMMs with optical marker frames at their tips, with highlighted D . B. Lateral View.

Table 4.7. Average error of position (mm) from linear trajectory (dashed lines in Figure 4.9) for Orthogonal Magnetization strategy.

ORTHOGONAL MAGNETIZATION						
Position Error of Actuated SMM from Linear Trajectory (mm)						
	Direction of Bending	D = 4 cm	D = 3.5 cm	D = 3 cm	D = 2.5 cm	D = 2 cm
Left SMM actuated	+x, -x	0.7	0.8	1.2	1.0	1.0
	+y, -y	0.8	0.8	0.7	1.1	1.1
Right SMM actuated	-x, +x	2.9	5.0	4.0	4.65	3.4
	-y, +y	1.7	0.9	0.7	0.5	0.6

Table 4.8. Average error of position (mm) from linear trajectory (dashed lines in Figure 4.10) for Parallel Magnetization strategy.

PARALELL MAGNETIZATION						
Position Error of Actuated SMM from Linear Trajectory (mm)						
	Direction of Bending	D = 4 cm	D = 3.5 cm	D = 3 cm	D = 2.5 cm	D = 2 cm
Left SMM actuated	+x, -x	3.95	3.8	4.2	1.3	0.5
	+y, -y	0.6	0.6	0.3	0.3	0.4
Right SMM actuated	-x, +x	1.3	0.8	0.9	1.8	0.7
	+y	0.4	0.8	1.25	0.6	0.2

Table 4.9. Numerical value of workspace for left and right manipulator approximated based on maximum bending in tested directions as depicted in Figure 4.9 and 4.10.

	Area (cm^2)			
	Orthogonal Magnetization		Parallel Magnetization	
D (cm)	Left SMM	Right SMM	Left SMM	Right SMM
2	0.56	0.29	0.08	0.16
2.5	0.58	0.46	0.17	0.28
3	0.55	0.23	0.27	0.33
3.5	0.55	0.23	0.33	0.43
4	0.55	0.32	0.45	0.56

Table 4.10. Error values for position of the static SMMs (cross-activation) for Orthogonal Magnetization.

ORTHOGONAL MAGNETIZATION						
Position Error for static SMM (%)						
	Direction of Bending	D = 4 cm	D = 3.5 cm	D = 3 cm	D = 2.5 cm	D = 2 cm
Left SMM actuated	+x	5.3	12.8	12.6	8.8	9.7
	-x	15.0	2.0	15.2	16.65	17.65
	+y	198.5	8.2	6.85	50.3	25.1
	-y	7.15	1.98	5.1	19.0	4.1
Right SMM actuated	-x	23.75	7.7	9.1	37	72
	-x	6.8	9.5	7.03	9.8	9.6
	+y	8.4	64.8	54.4	80.65	39.3
	-y	50.4	7.7	7.03	76.7	72.2

Table 4.11. Error values for position of the static SMMs (cross-activation) for Parallel Magnetization.

PARALELL MAGNETIZATION						
Position Error for static SMM (%)						
	Direction of Bending	D = 4 cm	D = 3.5 cm	D = 3 cm	D = 2.5 cm	D = 2 cm
Left SMM actuated	+x	9.3	0.65	16.95	56.1	46.3
	-x	9.2	23.2	6.09	26.9	13.2
	+y	21.0	30.0	72.2	57	70
	- y	4.1	5.3	14.6	8.4	12.4
Right SMM actuated	-x	27.6	26.4	30.6	36.6	35.0
	+y	15.3	11.7	15.3	18.8	29.2
	-y	69	5.5	6.8	10.1	12.3

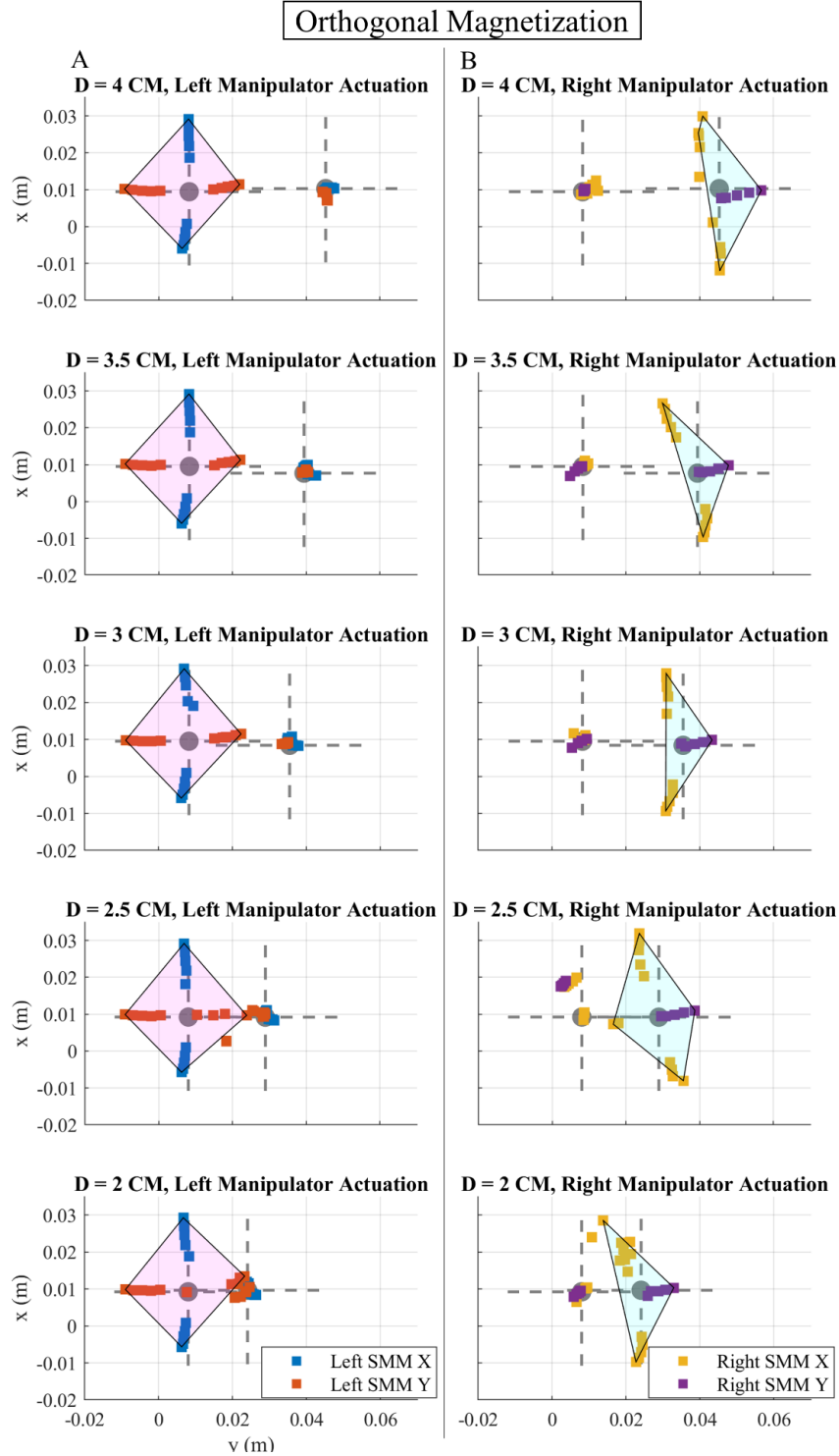


Figure 4.9. Combined results of independence testing at distance D for OM strategy. The colors indicate each segment's motion, and corresponding colors on the opposing manipulator shows its motion, while expected to be static. Dashed lines represent ideal linear trajectory. A. Activation of right manipulator. B. Activation of left manipulator. Polygons drawn between maximum bending in each direction, represent approximation of the reachable workspace of manipulator

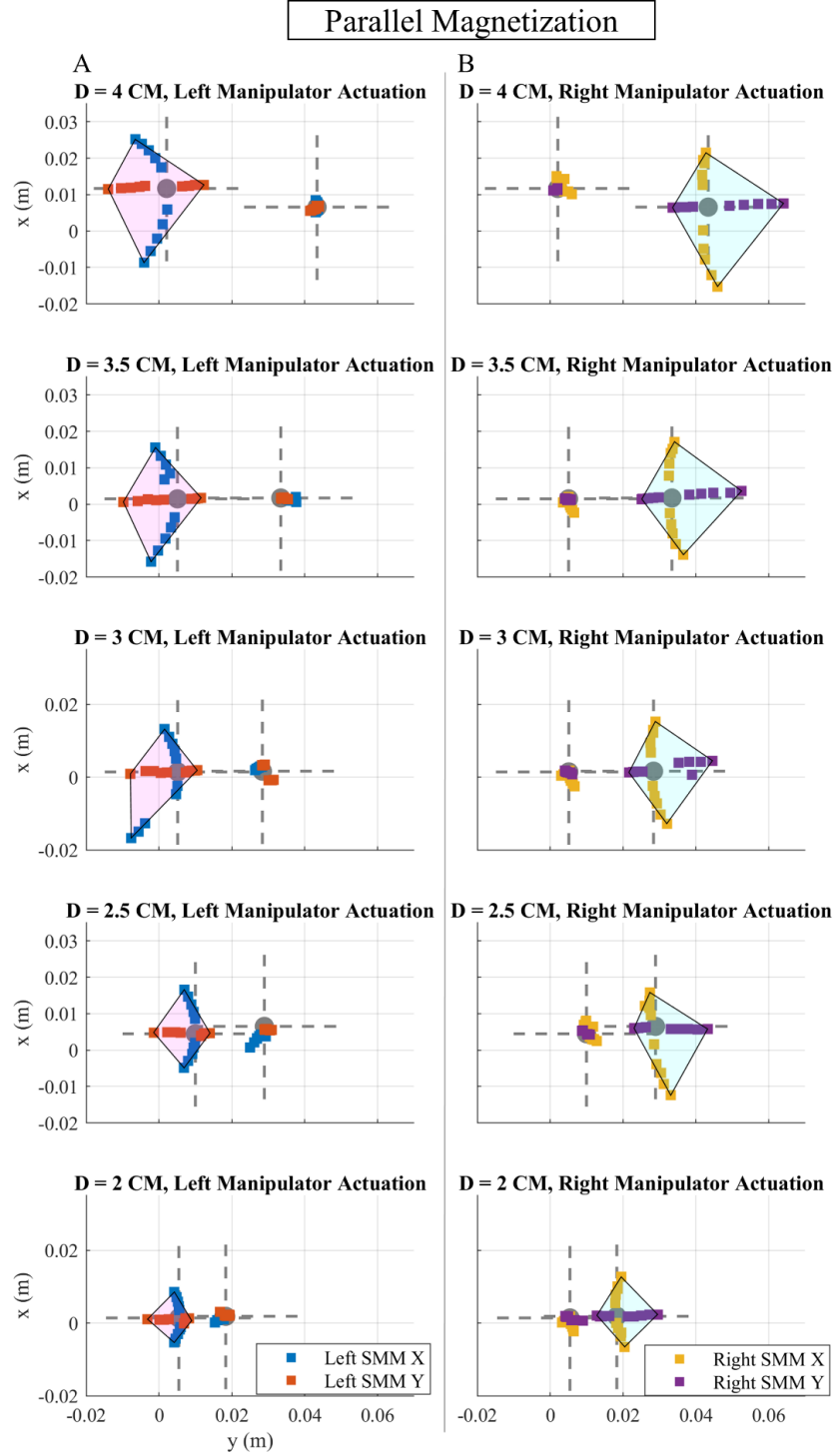


Figure 4.10. Combined results of independence testing at distance D for PM strategy. The colors indicate each segment's motion, and corresponding colors on the opposing manipulator shows its motion, while expected to be static. Dashed lines represent ideal linear trajectory; A. Activation of right manipulator. B. Activation of left manipulator. Polygons drawn between maximum bending in each direction, represent approximation of the reachable workspace of manipulator.

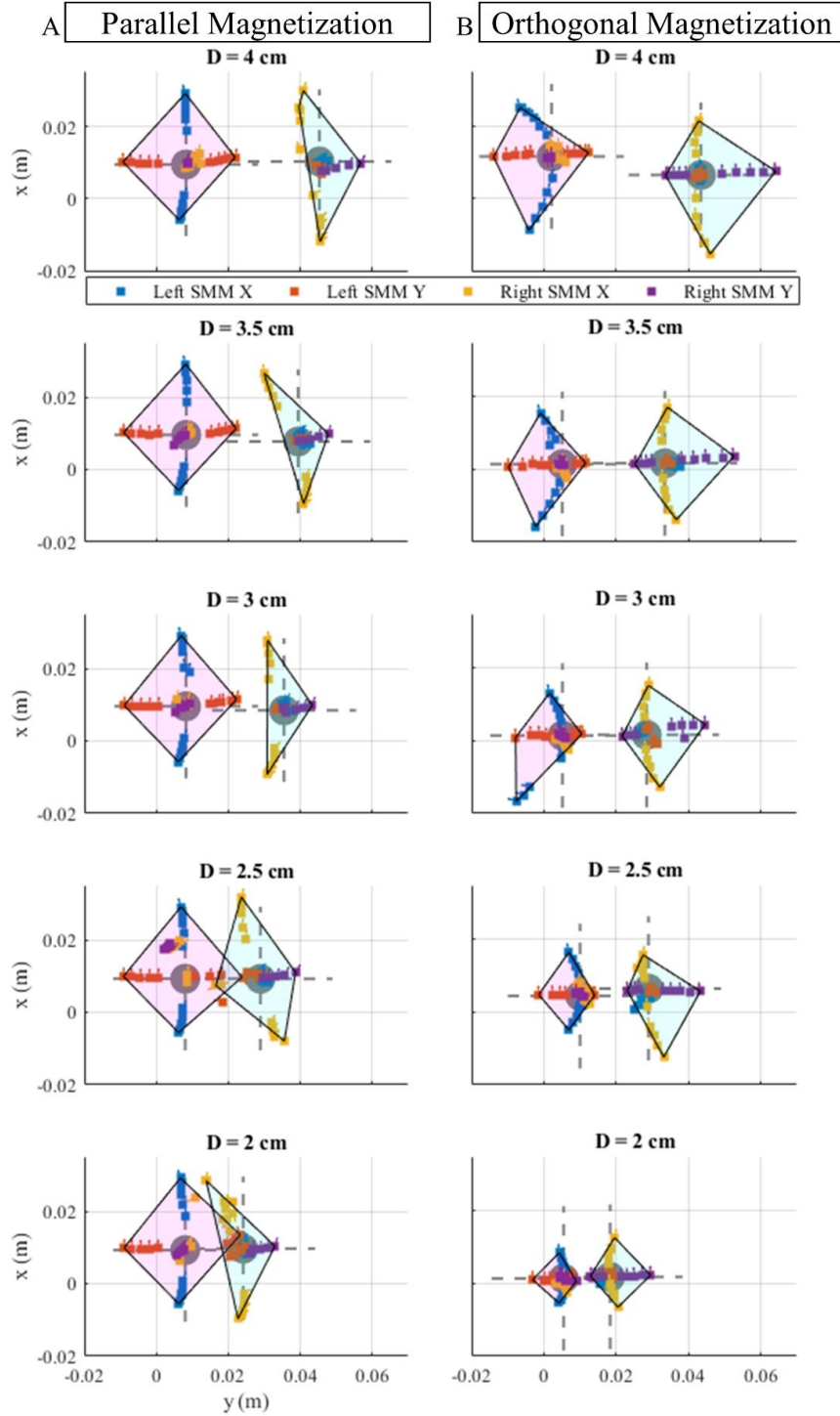


Figure 4.11. Combined results of independence testing at distance D . The colors indicate each segment's motion, and corresponding colors on the opposing manipulator shows its motion, while expected to be static. A. Orthogonal Magnetizations strategy. B. Parallel Magnetizations strategy. Polygons drawn between maximum bending in each direction, represent approximation of the reachable workspace of each manipulator in all evaluated cases.

Figures 4.9 and 4.10 show the results for the independent actuation tests for the left (Figure 4.9A and 4.10A) and right (Figure 4.9B and 4.10B) manipulators under the OM and PM strategies respectively, for five different separation distances. For comparison, Figure 4.11 shows the combined manipulator characterization results for both presented magnetization strategies. Pose information collected via motion tracking is projected in the X-Y plane, alongside the ideal manipulator trajectory, represented as dashed lines. The data points representing maximum deflection in each direction ($-x$, x , y , $-y$) are connected to represent the approximated reachable area/workspace of each manipulator. Tables 4.7 and 4.8 present position error values for OM and PM strategy respectively, calculated through averaging error values in positive and negative directions ($-x$, $+x$ and $-y$, $+y$), apart from right manipulator in the PM strategy which was actuated only in $+y$ due to workspace limitations, as explained further in the section 4.5.

Manipulators utilizing the PM strategy (Figure, 4.10, 4.11B) show the greatest range of motion at the largest separation distance ($D = 4$ cm) and show a reduction in range of motion as the separation distance decreases. This effect is a consequence of the PM strategy. As the proximity of the actuated manipulator with respect to the un-actuated manipulator (located at the focal point \mathbf{p}) reduces, the field induced at the actuated manipulator will be lower, as expressed by Equation 4.5. Additionally, we observe an asymmetry in the reachable workspace between left and right manipulator at the same separation distances in the PM strategy (Figure 4.10, 4.11B). This is due to limitations in the calibration accuracy, i.e. if the center of the magnetic workspace is not exactly located in the middle of the two manipulators, the magnitude of the magnetic field applied on the left and right SMMs will not be the same, leading to asymmetrical bending behaviors (Figure 4.11, Table 4.9).

These effects are not present for the OM strategy (Figure 4.9, 4.11A), where the calculated area for actuation of the left manipulator in OM case is similar for all tested distance, and area for the right manipulator fluctuates due to the cross-talk at smaller separation distances.

Specifically, distances $D = 2.5$ cm and $D = 2$ cm (Figure 4.9), show disturbance in expected motion as well as instability of the non-actuated manipulators, for both left and right manipulator actuation. These inaccuracies are caused by attraction between manipulators, which can be observed in the Supplementary Video 1. In the same case, inward motion (direction $-y$) with right manipulator was not possible with application of gradient $-\frac{\partial B_x}{\partial y}$ as expected from Table 4.5. This field condition caused torsion about main axis, flipping magnetization direction of the manipulator, leading to bending in y direction (outwards), which is actuated by application of gradient $\frac{\partial B_x}{\partial y}$.

From analysis of all collected data and videos, in some field conditions, the right SMM in the orthogonally magnetized strategy experiences torsional forces (Supplementary Video 1), when expected to be static. This is caused by the unstable condition being realized between the magnetization vector (μ_x) applied field (B_y) in this case, aiming to actuate left SMM (described in section 2.1).

Due to axial magnetization of both SMMs in the second strategy, no unstable actuation conditions are imposed, hence manipulators do not experience torsional deformation (Table 4.5, Supplementary Video 2).

Analysis of Figures 4.9-11 and Videos 1 and 2 showed that independent control of left and right SMMs was possible at all tested distances for both actuation strategies. Therefore, we can conclude that ‘the smallest possible distance’ for OM and PM strategies is 2cm.

4.4.4 Phantom Testing

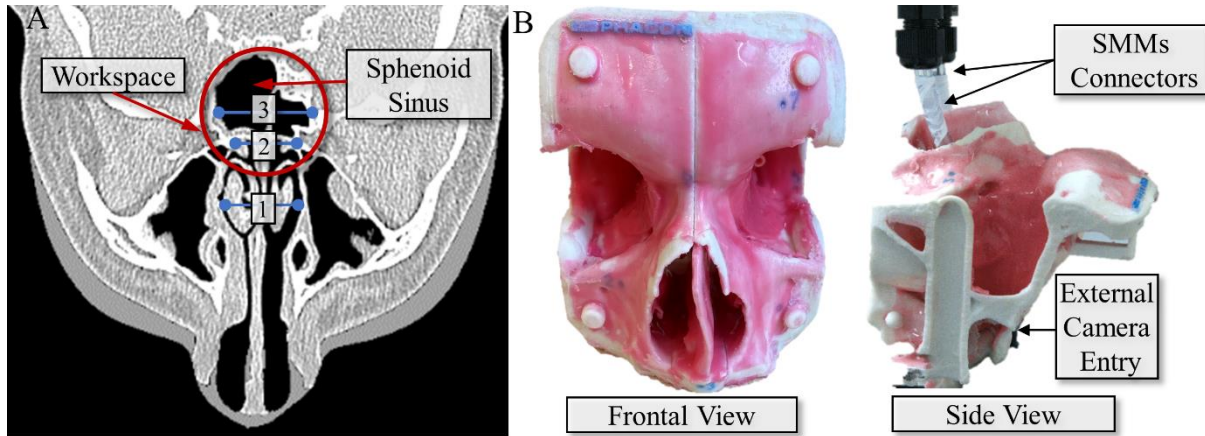


Figure 4.12. A horizontal slice of a CT scan from patient ‘Meyer’ used to manufacture skull phantom used in this study (source: phacon.de) with highlighted workspace of interest. B. Photographs of the phantom including frontal and side view with highlighted entry for an external camera with light source.

Table 4.12. Approximated workspace size in the skull base phantom based on the CT scan.

	Distal nostrils width (1)	Distal nasal cavity, opening to the sphenoid sinus (2)	Workspace width (sphenoid sinus) (3)
Size (mm)	24.7	22.8	31.4

Analysis of characterization results shows pros and cons of the two presented actuation strategies. Suitability of each strategy should be considered depending on the intended application, including requirements range of motion and size of the anatomical cavity. Considering anatomical constraints (Figure 4.12) and the desire to maximize range of motion, priority was given to the increased range of motion at smaller separation distances offered by the OM strategy (Figure 4.9), over providing bending modalities in four directions.

To produce concept bimanual surgical tools for the endonasal application, two dual-segment manipulators based on the OM strategy (Figure 4.6) were integrated with functional components. The fabrication technique detailed in Figure 4.5 was adapted to accommodate a 2 mm camera

(0.003 g) (160k WLC CMOS, Fujikura, Japan) in the left manipulator and an optical fiber (FG105UCA, Thorlabs, USA) in the right manipulator (Figure 4.14).

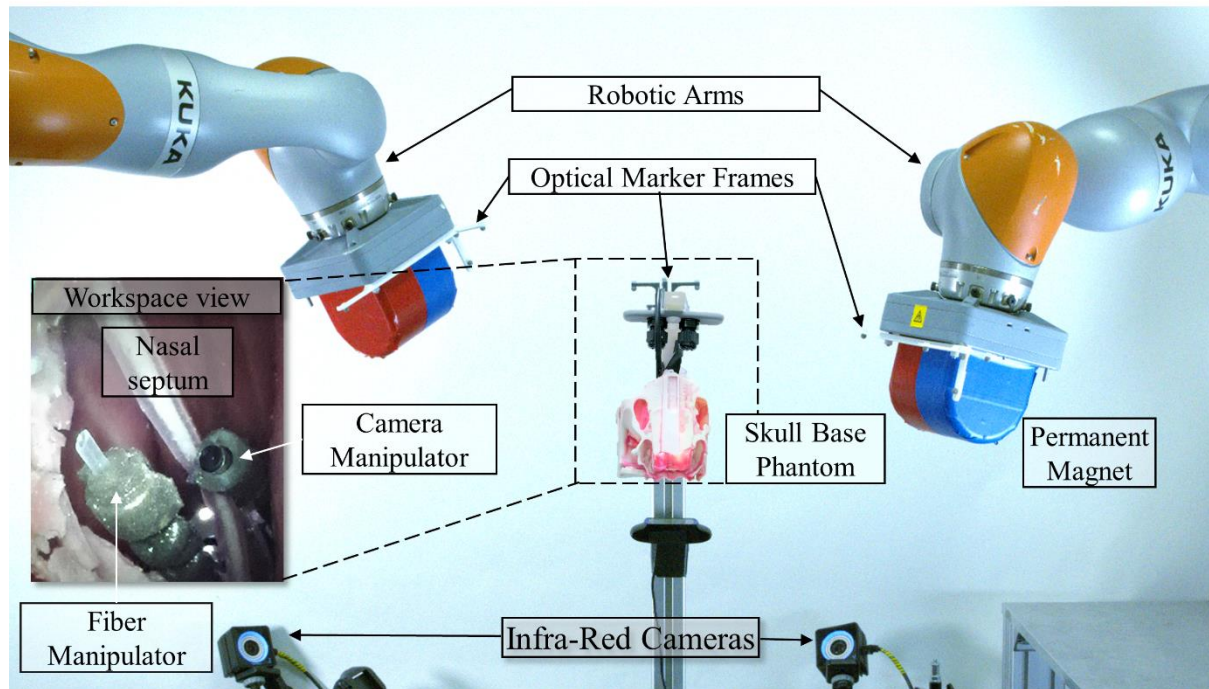


Figure 4.13. Experimental set up for phantom testing, with a close-up view of a workspace accessed with a camera and a light source through an opening in the sella bone.

Using our large workspace dual-arm robotic magnetic field control system (Figure 13), we assessed independent manipulators within an anatomically accurate skull phantom manufactured using real patient Computer Tomography (CT) scan data (Phacon, Germany) and mechanically realistic materials. Our design requirements for this system were based on currently used EES tools, as well as analysis of anatomical pathways and workspace within the nasal cavities of basing on the CT scan data.

The phantom was prepared according to the surgical standards for EES procedures by an ENT surgeon, by partial removal of nasal turbinates, distal septum, and a part of sphenoid bone to widen the workspace for manipulators and for access to access the pituitary socket. A silicone target was

placed in the workspace on the wall of sella turcica, the bone of the pituitary fossa as indicated in Figure 4.14.

Manipulators with camera, fiber and their connections were attached to flexible tubes and fixed on a 3D printed holder above the phantom. The distal ends of the manipulators were inserted into the nostrils and advanced to position within the target workspace, as seen in Figure 4.14. Once in place, the left manipulator with embedded camera was first independently actuated to allow inspection of the workspace (Supplementary Video 3). Subsequently, the right manipulator with embedded fiber was independently actuated to test its range of motion while the camera (left manipulator) was held still. After evaluating that sufficient range of motion can be provided to reach the target with the light source, the manipulator was actuated to an optimal pose, the light source was turned on and magnetic field was modulated multiple times from 5 mT to 7 mT in X direction to create repeated linear motion on the target, mimicking a laser beam ablating an adenoma (Supplementary Video 3). In the Video 3, the position of the laser tip was evaluated as a part of post-processing analysis. Each point was determined through identification of the middle (maximum brightness) of the laser tip as the manipulator moves in the view of the external camera. We found the average error to be 0.13 mm with standard deviation of 9.8 % and the highest positional error of 0.34 mm. In this experiment, the manipulators were positioned at the distance D between 22.8 to 31.4 mm (based on the CT scan (Table 4.12)). Considering results for OM testing (Figure 4.9, Supplementary Video 1), attraction in case of inward bending was expected with lowest magnitude conditions (3 mT). However, the anatomical features of the workspace provided increased mechanical separation of the manipulators and attraction occurred only with higher field magnitude of 7 mT. In this case application of $-B_y$ caused reciprocal attraction and the opposite field (B_y) was applied to induce their separation (Supplementary Video 4).

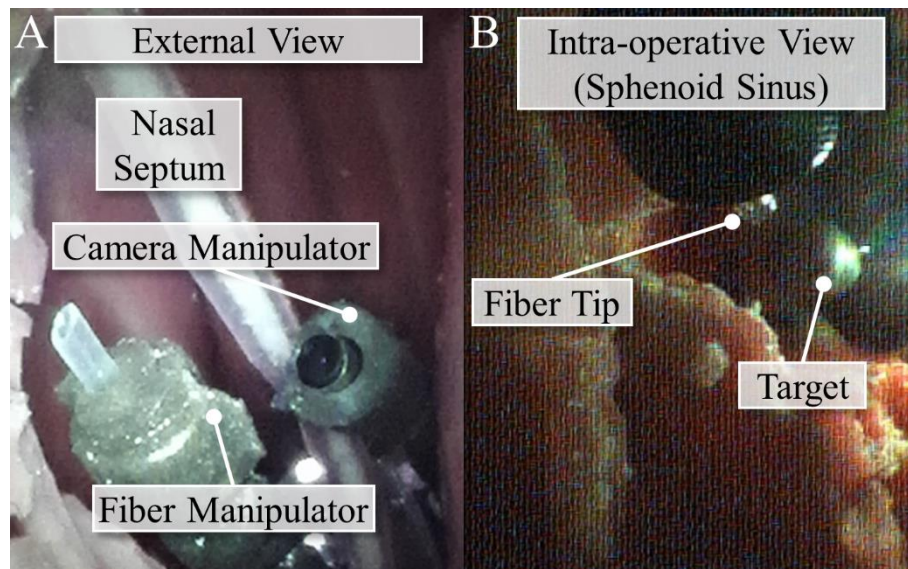


Figure 4.14. A. View from the endoscopic camera attached in the phantom for bottom view of the site. B. Intra-operative view of the camera embedded into one of the manipulators.

4.5 Discussions and Conclusions

In this paper, we present for the first time a dual-magnetic manipulator system for medical applications in confined workspaces. We developed a geometrically optimized design of a SMM to provide preferential bending planes and high angles of deflection. When configured into two parallel manipulators (Figure 4.6 and 4.7), independent magnetic manipulation is possible via two distinct actuation strategies. These utilize specific manipulator magnetization profiles (OM strategy) and local magnetic field gradient control (PM strategy) respectively and are implemented using our dEPM robotic platform.

Characterizing the two strategies as a function of manipulator separation, assessing the range of motion and the effect of manipulator interacting forces during independent manipulator actuation, identified associated advantages and disadvantages for each. The presented PM strategy (Figure 4.10) shows consistent bi-planar actuation with minimal manipulator cross-talk for all separation distances. However, this strategy suffers from a reduction in bending range of motion (and thus workspace) for smaller separations due to weaker induced magnetic fields on the actuated manipulator. It is also notable that achieving independent actuation via this method is highly coupled to the calibration accuracy of the dEPM system and identification and alignment of the focal point, with even a small movement in the focal point causing both agents to be simultaneously actuated. Additionally, the calibration accuracy can also affect the symmetry in the reachable workspace of the left and right manipulator. To resolve these accuracy issues, the calibration methods for the dEPM platform can be improved through implementing more accurate optical tracking system in the future. This issue is far less significant for the presented OM strategy (Figure 4.9), where actuation is induced primarily via homogeneous magnetic fields, relaxing the

accuracy requirements of the dEPM system. Using the OM strategy, the non-actuated manipulator will ideally remain stationary until a certain unique magnetic field is applied. However, as evidenced through the presented OM independent actuation tests, (Figure 4.9 and Figure 4.11A), separation distance influences the level of independent motion achievable due to the effects of magnetic interaction (cross-talk) between the manipulators. Furthermore, under the application of gradient $-\frac{\partial B_x}{\partial y}$ to the right manipulator, the desired inward motion (direction $-y$) is not achieved. This is due to the induced magnetic field's orientation with respect to the manipulator's magnetization causing torsion about its main axis, effectively flipping the magnetization direction of the manipulator and leading to undesired bending in $+y$ direction (outwards) instead (Supplementary Video 1).

Independent control was possible at all tested distances, with different levels of cross-talk and cross-activation, depending on the actuation strategy and separation distance, where the smallest tested separation distance was 2 cm. The smallest possible distance (function of cross-talk) will vary with change in manipulator length, diameter, elastomeric properties and amount of magnetic material. Therefore, depending on the exact application of the dual-manipulator system, SMM's dimensions will vary and with those – the amount of cross talk and smallest distance at which SMMs can still achieve independent control.

Regardless of the identified limitations of the proposed strategies, independent motion of the two parallel manipulators was possible over a large area for both (up to 0.55 cm^2 and 0.32 cm^2 for OM strategy and up to 0.45 cm^2 and 0.56 cm^2 for PM strategy). Although the achievable range of motion would increase with the removal of the marker frames (required for tracking), successful actuation with this payload indicates potential suitability for surgical tool manipulation with confined anatomy. This proposed system was thus evaluated for the scenario of EES (Figure 4.13,

4.14), and independent actuation of two manipulators (with camera and optical fiber, respectively). This was qualitatively tested in the confined endonasal space of a 3D printed base skull phantom. Evaluation of laser tip position showed the average positional error of 0.13 mm. Further feasibility tests in terms of clinical application should be performed in future works. Evaluation of maximum payload possible to manipulate at the tip is of interest for surgical applications requiring tool-tissue interaction such as the use of cutting tools, ultrasound probes or forceps. Moreover, the quantification and optimization of speed of tasks performed with the presented bi-manual manipulator system will be of interest for any practical application to surgical scenarios.

Future adaptations may leverage the discrete modular approach proposed to deliver different configurations of multiple short segments for increased maneuverability and/or range of motion, or to facilitate controlled navigation approaches. To enhance the stability of the system when the OM strategy is applied, approaches to increase torsion stiffness of one of both manipulators may be explored ([36], [16]). Additionally, integration of proprioceptive and localization feedback would aid navigating in visually obscured clinical scenarios (based on pre-operative anatomical scans) and allow for stable focal point tracking and independent closed loop manipulator control.

The proposed design approach and actuation strategies demonstrate independent actuation of two magnetic continuum manipulators within the same confined workspace. This opens a new approach to magnetically controlled surgical tools suited to application within confined, delicate anatomy. Coupling the scalability of monolithic magnetic manipulators with independent local actuation offers prospects for improving endoscopic procedures currently served by large and rigid tools, with associated benefit to the patient and surgeon.

Bibliography

- [1] P. E. Dupont et al., “A decade retrospective of medical robotics research from 2010 to 2020,” *Sci. Robot.*, vol. 6, no. 60, 2021, doi: 10.1126/scirobotics.abi8017.
- [2] T. Da Veiga et al., “Challenges of continuum robots in clinical context: A review,” *Prog. Biomed. Eng.*, vol. 2, no. 3, 2020, doi: 10.1088/2516-1091/ab9f41.
- [3] A. Bajo and N. Simaan, “Hybrid motion/force control of multi-backbone continuum robots,” *Int. J. Rob. Res.*, vol. 35, no. 4, pp. 422–434, 2016, doi: 10.1177/0278364915584806.
- [4] H. B. Gilbert, D. C. Rucker, and R. J. Webster, “Concentric tube robots: The state of the art and future directions,” *Springer Tracts Adv. Robot.*, vol. 114, pp. 253–269, 2016, doi: 10.1007/978-3-319-28872-7_15.
- [5] R. Wirz et al., “An experimental feasibility study on robotic endonasal telesurgery,” *Neurosurgery*, vol. 76, no. 4, pp. 479–484, 2015, doi: 10.1227/NEU.0000000000000623.
- [6] N. Simaan et al., “Design and Integration of a Telerobotic System for Minimally Invasive Surgery of the Throat,” *Int. J. Rob. Res.*, vol. 28, no. 9, pp. 1134–1153, 2009, doi: 10.1177/0278364908104278.
- [7] M. Runciman, A. Darzi, and G. P. Mylonas, “Soft Robotics in Minimally Invasive Surgery,” *Soft Robot.*, vol. 6, no. 4, pp. 423–443, 2019, doi: 10.1089/soro.2018.0136.
- [8] M. McCandless, A. Perry, N. DiFilippo, A. Carroll, E. Billatos, and S. Russo, “A soft robot for peripheral lung cancer diagnosis and therapy,” *Soft Robot.*, vol. 9, no. 04, 2021, doi: 10.1089/soro.2020.0127.
- [9] M. Brancadoro, M. Manti, F. Grani, S. Tognarelli, A. Menciassi, and M. Cianchetti, “Toward a variable stiffness surgical manipulator based on fiber jamming transition,” *Front. Robot. AI*, vol. 6, no. MAR, pp. 1–12, 2019, doi: 10.3389/frobt.2019.00012.

-
- [10] F. Campisano et al., “Teleoperation and Contact Detection of a Waterjet-Actuated Soft Continuum Manipulator for Low-Cost Gastroscopy,” *IEEE Robot. Autom. Lett.*, vol. 5, no. 4, pp. 6427–6434, 2020, doi: 10.1109/LRA.2020.3013900.
- [11] T. Da Veiga et al., “Material characterization for magnetic soft robots,” 2021 IEEE 4th Int. Conf. Soft Robot. RoboSoft 2021, pp. 335–342, 2021, doi: 10.1109/RoboSoft51838.2021.9479189.
- [12] G. Z. Lum et al., “Shape-programmable magnetic soft matter,” *Proc. Natl. Acad. Sci. U. S. A.*, vol. 113, no. 41, pp. E6007–E6015, Oct. 2016, doi: 10.1073/pnas.1608193113.
- [13] Y. Kim et al., “Telerobotically Controlled Magnetic Soft Continuum Robots for Neurovascular Interventions,” *Proc. - IEEE Int. Conf. Robot. Autom.*, pp. 9600–9606, 2022, doi: 10.1109/ICRA46639.2022.9812168.
- [14] Y. Kim et al., “Telerobotic neurovascular interventions with magnetic manipulation,” *Sci. Robot.*, vol. 7, no. 65, 2022, doi: 10.1126/scirobotics.abg9907.
- [15] G. Pittiglio et al., “Patient-Specific Magnetic Catheters for Atraumatic Autonomous Endoscopy,” *Soft Robot.*, vol. 00, no. 00, pp. 1–14, 2022, doi: 10.1089/soro.2021.0090.
- [16] P. Lloyd, O. Onaizah, G. Pittiglio, D. K. Vithanage, J. H. Chandler, and P. Valdastri, “Magnetic Soft Continuum Robots With Braided Reinforcement,” *IEEE Robot. Autom. Lett.*, vol. 7, no. 4, pp. 9770–9777, 2022, doi: 10.1109/LRA.2022.3191552.
- [17] T. Wang et al., “Adaptive wireless millirobotic locomotion into distal vasculature,” *Nat. Comms*, 13:4465, 2022, doi: 10.1038/s41467-022-32059-9.
- [18] V. K. Michiel Richter, Mert Kaya, Jakub Sikorski, Leon AbelmannVenkiteswaran and S. Misra, “Magnetic Soft Helical Manipulators with Local Dipole Interactions for Flexibility and Forces,” *Soft Robotics*, vol. 10, no. 03, pp. 1–13, 2022, doi: 10.1089/soro.2022.0031.

-
- [19] C. M. Heunis, Y. P. Wotte, J. Sikorski, G. P. Furtado, and S. Misra, “The ARMM System - Autonomous Steering of Magnetically-Actuated Catheters: Towards Endovascular Applications,” *IEEE Robot. Autom. Lett.*, vol. 5, no. 2, pp. 704–711, 2020, doi: 10.1109/LRA.2020.2965077.
- [20] S. Tottori, L. Zhang, K. E. Peyer, and B. J. Nelson, “Assembly, disassembly, and anomalous propulsion of microscopic helices,” *Nano Lett.*, vol. 13, no. 9, pp. 4263–4268, 2013, doi: 10.1021/nl402031t.
- [21] E. Diller, J. Giltinan, and M. Sitti, “Independent control of multiple magnetic microrobots in three dimensions,” *Int. J. Rob. Res.*, vol. 32, no. 5, pp. 614–631, 2013, doi: 10.1177/0278364913483183.
- [22] I. S. M. Khalil et al., “Independent Actuation of Two-Tailed Microrobots,” *IEEE Robot. Autom. Lett.*, vol. 3, no. 3, pp. 1703–1710, 2018, doi: 10.1109/LRA.2018.2801793.
- [23] J. Giltinan, P. Katsamba, W. Wang, E. Lauga, and M. Sitti, “Selectively controlled magnetic microrobots with opposing helices,” *Appl. Phys. Lett.*, vol. 116, no. 13, 2020, doi: 10.1063/1.5143007.
- [24] P. Katsamba and E. Lauga, “Micro-Tug-of-War: A Selective Control Mechanism for Magnetic Swimmers,” *Phys. Rev. Appl.*, vol. 5, no. 6, 2016, doi: 10.1103/PhysRevApplied.5.064019.
- [25] E. Diller, S. Floyd, C. Pawashe, and M. Sitti, “Control of multiple heterogeneous magnetic micro-robots on non-specialized surfaces,” *Proc. - IEEE Int. Conf. Robot. Autom.*, vol. 28, no. 1, pp. 115–120, 2011, doi: 10.1109/ICRA.2011.5979785.

-
- [26] S. Miyashita, E. Diller, and M. Sitti, “Two-dimensional magnetic micro-module reconfigurations based on inter-modular interactions,” *Int. J. Rob. Res.*, vol. 592, no. 32 (5), 2013, doi: 10.1177/0278364913479837.
- [27] M. Salehizadeh and E. Diller, “Two-agent formation control of magnetic microrobots in two dimensions,” *J. Micro-Bio Robot.*, vol. 12, no. 1–4, pp. 9–19, 2017, doi: 10.1007/s12213-017-0095-5.
- [28] M. Salehizadeh and E. Diller, “Optimization-Based Formation Control of Underactuated Magnetic Microrobots via Inter-Agent Forces,” in *International Conference on Manipulation, Automation and Robotics at Small Scales (MARSS)*, IEEE, 2017. doi: doi: 10.1109/MARSS.2017.8001910.
- [29] J. Rahmer, C. Stehning, and B. Gleich, “Spatially selective remote magnetic actuation of identical helical micromachines,” *Sci. Robot.*, vol. 2, no. 3, pp. 1–10, 2017, doi: 10.1126/scirobotics.aal2845.
- [30] F. Ongaro, S. Pane, S. Scheggi, and S. Misra, “Design of an Electromagnetic Setup for Independent Three-Dimensional Control of Pairs of Identical and Nonidentical Microrobots,” *IEEE Trans. Robot.*, vol. 35, no. 1, pp. 174–183, 2019, doi: 10.1109/TRO.2018.2875393.
- [31] E. Diller, J. Giltinan, G. Z. Lum, Z. Ye, and M. Sitti, “Six-degree-of-freedom magnetic actuation for wireless microrobotics,” *The International Journal of Robotics Research*. 2016;35(1-3):114-128, 2016, doi: 10.1177/0278364915583539.
- [32] S. Salmanipour and E. Diller, “Eight-degrees-of-freedom remote actuation of small magnetic mechanisms,” *Proc. - IEEE Int. Conf. Robot. Autom.*, pp. 3608–3613, 2018, doi: 10.1109/ICRA.2018.8461026.

-
- [33] G. Pittiglio, M. Brockdorff, T. da Veiga, J. Davy, J. H. Chandler, and P. Valdastrì, “Collaborative Magnetic Manipulation via Two Robotically Actuated Permanent Magnets,” *IEEE Trans. Robot.*, pp. 1–12, 2022, doi: 10.1109/TRO.2022.3209038.
- [34] T. Terada, K. Kovacs, L. Stefaneanu, and E. Horvath, “Incidence, pathology, and recurrence of pituitary adenomas: Study of 647 unselected surgical cases,” *Endocr. Pathol.*, vol. 6, no. 4, pp. 301–310, 1995, doi: 10.1007/BF02738730.
- [35] E. R. Constantino, R. Leal, C. C. Ferreira, M. A. Acioly, and J. A. Landeiro, “Surgical outcomes of the endoscopic endonasal transsphenoidal approach for large and giant pituitary adenomas: Institutional experience with special attention to approach-related complications,” *Arq. Neuropsiquiatr.*, vol. 74, no. 5, pp. 388–395, 2016, doi: 10.1590/0004-282X20160042.
- [36] P. Lloyd et al., “Feasibility of Fiber Reinforcement Within Magnetically Actuated Soft Continuum Robots,” *Front. Robot. AI*, vol. 8, no. July, pp. 1–10, 2021, doi: 10.3389/frobt.2021.715662.

Chapter 5 Double Helix Optimization

Chapter source: Selective Geometric Modification for Independent Actuation of Multiple Soft Magnetic Manipulators," Z Koszowska, A Bacchetti, P Lloyd, G Pittiglio, J H Chandler and P Valdastri, 2023 IEEE International Conference on Robotics and Biomimetics (ROBIO), Koh Samui, Thailand, 2023, pp. 1-6, ©[2023] IEEE
doi: 10.1109/ROBIO58561.2023.10354735

Abstract

Soft Magnetic Manipulators (SMM) have the potential to improve current endoscopic procedures through extreme miniaturization and inherently safe tissue interaction. This relatively new field of soft robots is being extensively researched for various medical applications. However, utilization of two or more SMMs under stable control within the same workspace is challenging due to their exposure to similar or identical applied magnetic fields and field gradients. To improve stable independent control of SMMs in a shared workspace, we explore geometric variations to the SMM design, consisting of elastomeric double helices wrapped around a cylindrical core. The influence of geometrical properties on stiffness in two bending planes is investigated, as well as torsional stability across six tested designs. Experimentally acquired data on bending and twisting of proposed designs is compared to equivalent soft magnetic cylinders. Finally, to demonstrate the capability of independent actuation, two selected designs are tested in multi-SMM parallel configurations, consisting of two and three parallel SMMs within the same workspace

5.1 Introduction

Endoscopic approaches to surgery present with benefits of reduced trauma and fewer complications. However, challenges remain due to technological limitations, which can preclude endoscopic access to deep anatomical structures. In cases where diagnosis or treatment is needed in deeper anatomy, the tool requirements do not only include miniaturization, but also capability of high deflection angles and maneuverability within a limited workspace. The field of soft robotics may offer solutions to some of the issues faced in endoscopic surgical approaches, providing small compliant manipulators with increased Degrees of Freedom (DoF) for superior maneuverability and inherently safe tissue interactions [1], [2]. Of these robotic designs, the relatively new field of Soft Magnetic Manipulators (SMMs) presents some notable advantages with respect to other approaches (e.g. cable driven or pneumatically actuated soft robots) when designing for small scales [3], [4].

SMMs containing microscopic magnetic particles are entirely soft and can be magnetically pre-programmed to produce desired deformations under exposure to specific and controlled external magnetic fields [5] (Fig. 5.1). External, remote actuation of this type thus enables extreme miniaturization without loss of controllable DoFs [6]. This is often impossible to achieve with other approaches due to the accommodation of onboard actuation (wiring, tubing, tendons etc.). Due to these advantages, magnetically actuated devices can be beneficial in the medical environment and have been proposed for many applications [7]–[12].

Even though magnetic actuation presents several benefits, applications in surgery can be still challenging when procedures require collaborative control of multiple instruments, such as camera, forceps, cutting device, suction etc. Two or more identical magnetic agents in one workspace respond in the same manner when exposed to external magnetic fields.

To allow independent actuation between magnetic agents, researchers utilize geometric [13]–[17] or magnetic [18], [19] heterogeneity between agents or inter-agent magnetic interaction [20], [21] leading to different responses under application of a uniform magnetic field. Alternatively, two homogenous agents can be independently actuated through advanced magnetic control, utilizing magnetic field gradients [22]. Research on independent magnetic control up to date has primarily focused on untethered microrobots, leaving control of multiple continuum SMMs an open challenge.

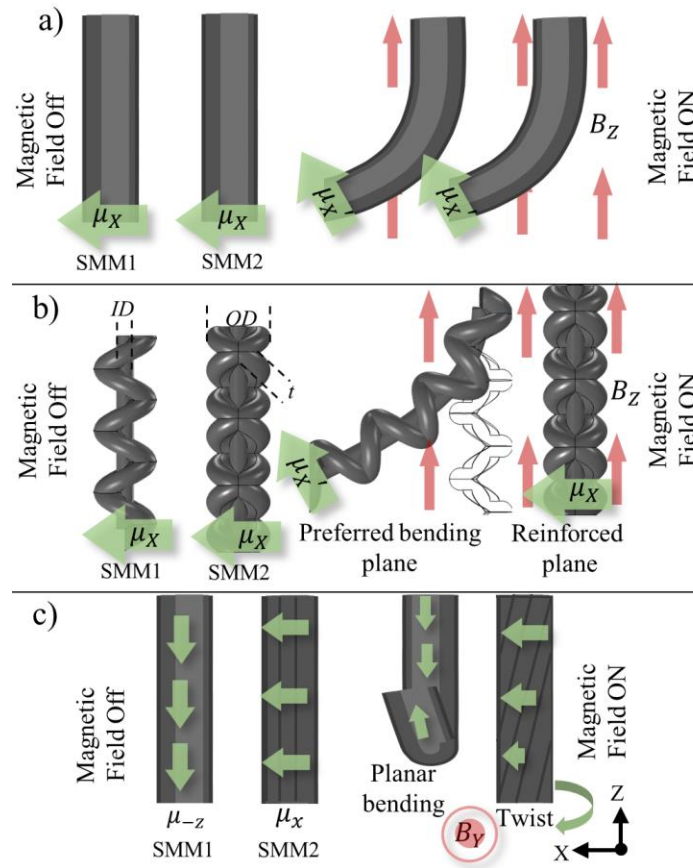


Figure 5.1. a) Two soft magnetic cylinders with identical magnetization experience the same deflection in a homogenous magnetic field, in any orientation. b) Independent actuation based on geometrical heterogeneity of agents; two soft magnetic manipulators with helical reinforcement and identical magnetization, when arranged orthogonally in one workspace will respond differently to the applied homogenous magnetic field. c) Unstable scenario in a case of magnetic heterogeneity of agents, where magnetization vector of SMM2 creates a 90° angle with applied magnetic field vector leading to a twist along the longitudinal axis.

In our recent work [23], we proposed a system where application of two manipulators in the same workspace is enabled through specific magnetic profiles and mechanical constraints to allow actuation independence at a millimeter scale, using our dual arm external permanent magnet (dEPM) system for field generation [24]. The proposed design is a monolithic elastomeric structure consisting of a double helix wrapped around a cylindrical core.

The seam of the double helix structure acts as a planar constraint, leading to a difference in bending stiffness between manipulator's axes (Fig 5.2). This mechanical constraint, together with specific magnetization direction, enables selective independent control of available DoFs when exposed to the same magnetic field conditions. The previous work included broad characterization of independent actuation modes and available workspace, only briefly investigating the effect of the double helix design parameters on the desired behavior.

In this work we investigate the effect of geometrical parameters of presented helical reinforcement on bending stiffness and torsional stability (twist) under a homogenous external magnetic field. The aim of this study is specifically focused on finding monolithic designs with an optimal trade-off between high deflection angle in desired actuation planes, and reduced twist in unstable scenarios, thus maximizing the potential for independent SMM control in one confined workspace.

5.2 Double Helix Reinforced SMM

5.2.1 Principles of Magnetic Actuation

A magnetic agent with magnetization μ is subject to magnetic force (f) and torque (τ) under an applied field B , respectively as

$$\mathbf{f} = \nabla (\boldsymbol{\mu} \cdot \mathbf{B}) \quad (5.1)$$

$$\boldsymbol{\tau} = \boldsymbol{\mu} \times \mathbf{B} \quad (5.2)$$

The magnetization vector(s) of an SMM is a crucial element in magnetic actuation of soft structures. As seen in (equation 5.2) when the magnetization $\boldsymbol{\mu}$ direction of the magnetic body aligns with the applied external magnetic field direction, the cross product decays to zero and no resultant torque occurs (no actuation). If the direction of $\boldsymbol{\mu}$ is misaligned with the external magnetic field vector \mathbf{B} , a resultant magnetic torque will be present on the body; expressed as the cross product of magnetization direction and applied external magnetic field (equation 5.2). Using this phenomenon, an SMM can be pre-programmed in a manner to achieve desired motion, when exposed to specific external magnetic fields. In cases where the angle between the magnetization vector of the SMM and the applied magnetic field reaches beyond 90° , an undesired torsional response may occur. That is, the SMMs twist around their longitudinal axis to align with the actuating field, rather than producing the desired bending deformation (Fig. 5.1C).

Mitigation of this effect is possible through constraints on the magnetization profile and/or actuating fields, or through introduction of anisotropic stiffness, as e.g. in [25], through addition of two helical fibers into the robot design or as in [26], by embedding a braid. Designs with enhanced torsional stability can improve actuation independence of manipulators in multi – SMM configurations by allowing for stable actuation over a wider range of manipulator-field conditions. For example, in scenarios where the direction of applied magnetic field, meant to actuate SMM1 (e.g. Fig. 5.1C), would create an unstable condition with the SMM's 2 magnetization vector, high torsional stability and planar reinforcement would ensure little to no movement.

Another scenario in which the SMM aimed to remain static is magnetized axially; to achieve no response under application of perpendicular magnetic field vector, some form of reinforcement is

required. This could potentially be achieved by stiffening on demand [27], however, to date, stiffening solutions for SMMs have been a challenge due to either scaling [28] or temperature issues [29].

Depending on the method of magnetic field generation and the manipulator requirements, in simple actuation cases it is possible to design a set up that purposefully omits unstable scenarios or simply relies on magnetic heterogeneity of agents, leading to a different response. However, considering complex configurations with multiple SMMs comprised of a large number of DoFs, the utilization of geometrical or magnetic heterogeneity or both, would be greatly beneficial. In those cases, geometric reinforcement is fundamental to achieve actuation independence, and the design features of the SMMs are critical for torsional stability and planar reinforcement.




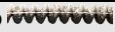

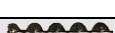

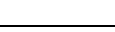
5.2.2 Design and Fabrication

In this section, we explore six helical designs (Table 5.1) with varied parameters of helix geometry including helix thickness (t) and number of revolutions per unit length (R) (Fig. 5.1). Maximum number of revolutions is considered a value at which further increase in R would form a cylinder instead of a double helix structure, which is specific to each investigated helix thickness (t). The inner core diameter (ID) and outer core diameter (OD) were kept constant for all designs. The outer diameter of 3.5 mm is close to currently used endoscopic manipulators, while 1 mm ID is sufficiently large to allow creation of a tool channel in the helical structure. As a control case, we also investigate cylinders of 3.5 mm and 1 mm in diameter.

The rationale behind the helical designs (Table 5.1) is as follows: The thinnest t value of 0.5 was determined by fabrication limits, as it represents the smallest feature we could mold with acceptable resolution. On the other end of the spectrum, a t value of 1.5 was selected based on initial experiments, which showed that this was the largest size capable of forming the desired

helix structure at the maximum R . Further increases in the t value would result in a structure resembling a cylinder rather than an intricate helix. The R values were chosen similarly, based on the maximum number of revolutions per unit length that could still produce a distinct double-helix structure. For each design, we also tested the structure at half the maximum R value.

Table 5.1. Design parameters of SMMs tested in this study.

Design	OD (mm)	ID (mm)	L (mm)	R	t (mm)
A 	3.5	1	15	15	0.5
B 	3.5	1	15	30	0.5
C 	3.5	1	15	8.14	1
D 	3.5	1	15	16.28	1
E 	3.5	1	15	4.71	1.5
F 	3.5	1	15	9.42	1.5
G 	3.5	N/A	15	N/A	N/A
H 	1	N/A	15	N/A	N/A

Candidate monolithic helical designs and cylinders (Table 5.1) were fabricated in a single-step casting process by using 3D printed molds (Grey V4 resin, Form III, Formlabs, USA). Silicone (Dragon Skin™ 10, Smooth-On, Inc., U.S.A.) was mixed with 100 wt% (percentage by weight) of hard magnetic microparticles (NdFeB with an average 5 μm diameter, MQFP-B+, Magnequench GmnH, Germany). The magnetic silicone was then mixed in a high vacuum mixer (ARV- 310, THINKYMIXER, Japan) for 90 seconds at a speed of 1400 rpm and a pressure of 20.0 kPa and injected into closed molds and cured at 45°C for 30 minutes (Fig. 5.2a). Each design was fabricated twice to allow magnetization in an impulse magnetic field of 4 T in two directions: along their Z and Y axes respectively, for independent and torsional stability testing. To verify resultant magnetization vectors, samples were analyzed using a magneto-optical sensor (MagView, Matesy, Germany) (Fig. 5.2b).

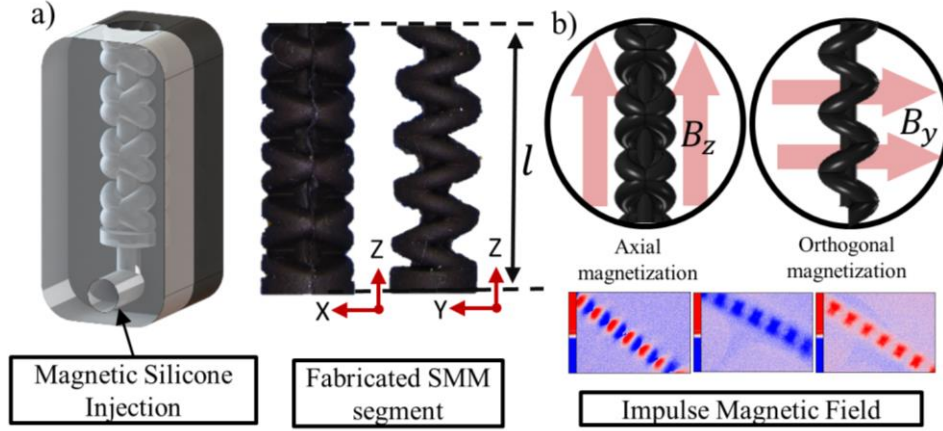


Figure 5.2. a) Fabrication process. b) Magnetization process, including axial and orthogonal magnetization; Magview images confirming desired magnetization profiles post-magnetization.

5.3 Results

5.3.1 Design Evaluation

Fabricated designs (Table 5.1) magnetized axially (Z) and orthogonally (Y) were evaluated by recording data on manipulator deformation under externally applied magnetic field at 2.5 mT, 5 mT and 7 mT using a uni-directional Helmholtz coil (DXHC10-200, Dexing Magnet Tech. Co., Ltd., Xiamen, China). The samples' long axes in the experimental set up were parallel with gravity (Z). Bottom and side view cameras allowed for collecting data on twist and bending angles respectively. All designs were evaluated for bending and twisting performance and the best two candidate designs are further evaluated in terms of payload and independent actuation.

5.3.1.1 Bending Stiffness

The samples for deflection testing were magnetized along their longitudinal axis (Z) and subjected to a uniform magnetic field B_x . To test SMMs deflection capabilities in XZ and YZ planes, we first aligned the XZ plane of an SMM with the magnetic torque and subsequently rotated the sample by 90° such that the magnetic torque was aligned with the YZ plane of the SMM.

This was repeated for all samples, separately. Collected data was analyzed as a ratio $R_{xy} = \gamma_x/\gamma_y$ where γ_x is the bending angle in the preferred direction and γ_y is bending angle in constrained direction, and as is presented in Fig 5.2.

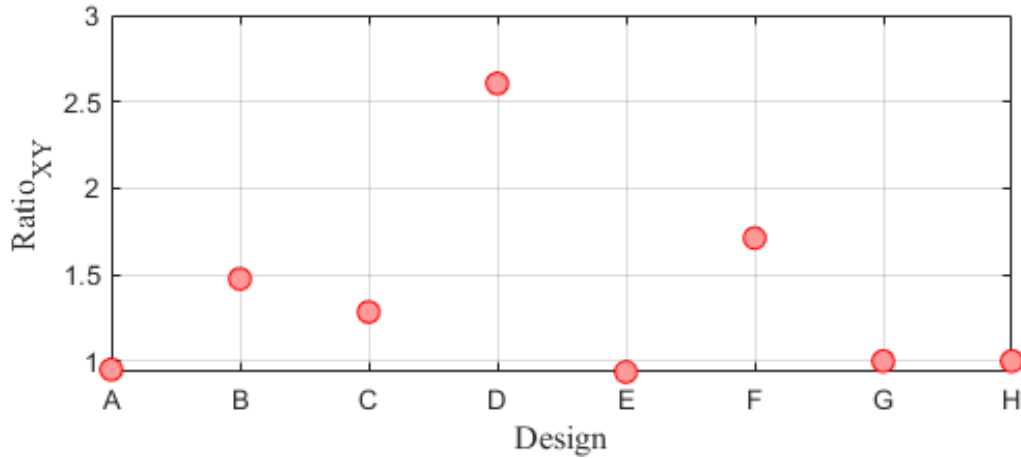


Figure 5.3. Ratio R_{xy} across all tested designs.

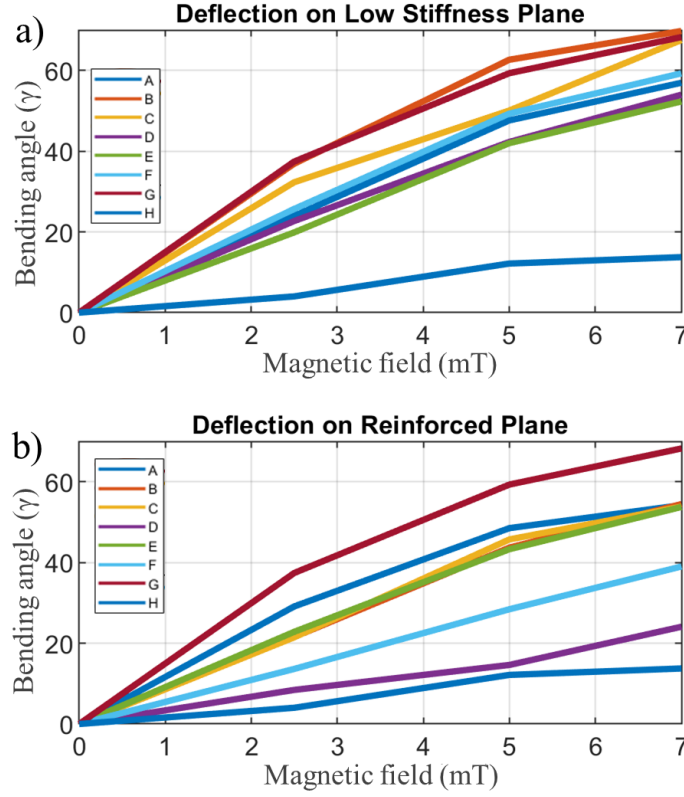


Figure 5.4. a) Bending angle γ_x on the low stiffness plane. (b) Bending angle γ_y on the reinforced plane.

Designs A and E showed ratio R_{xy} close to cylinders (G and H), showing negligible difference in bending stiffness between their XZ and YZ planes. Design D shows the highest ratio R_{xy} of all tested samples, approximately 2.5 times higher than two tested cylinders ($R_{xy} = 1$ (Fig. 5.3)). Additionally, all designs with helical features (A-F) experienced higher bending angle than cylinder of the same diameter (H) (Fig. 5.4A). The lowest bending angle at $B = 7 \text{ mT}$ of all helical designs was achieved with design E at 52.3° , which was still 3.8 times higher than the cylinder H (13.75°); the highest bending angle was achieved with design B at 68.2° , which is 5 times greater than cylinder H, and only 1° higher than cylinder G.

In Figure 5.4B at field $B = 7mT$, we observe designs A, B, C and E to reach approximately the same deflection of 54° on their reinforced plane, while designs D and F showed higher XZ stiffness achieving 24.1° and 39° respectively.

5.3.1.2 Torsional Stability

To collect information on twisting behavior, the samples magnetized along their Y axes were placed in the workspace and a magnetic field in direction perpendicular to magnetization vector of the tested sample was applied (B_x). This created a scenario of pure instability (twist without deflection).

Twist angle analysis on its own is not a valuable factor for characterization, since we consider an optimal SMM to be capable of high deflection angle while experiencing minimal twist. Hence, we additionally consider a ratio $R_{xz} = \gamma_x / \gamma_z$ where γ_x is bending in a preferred direction and γ_z is a twist angle in a purely unstable scenario, as presented in Fig. 5.5

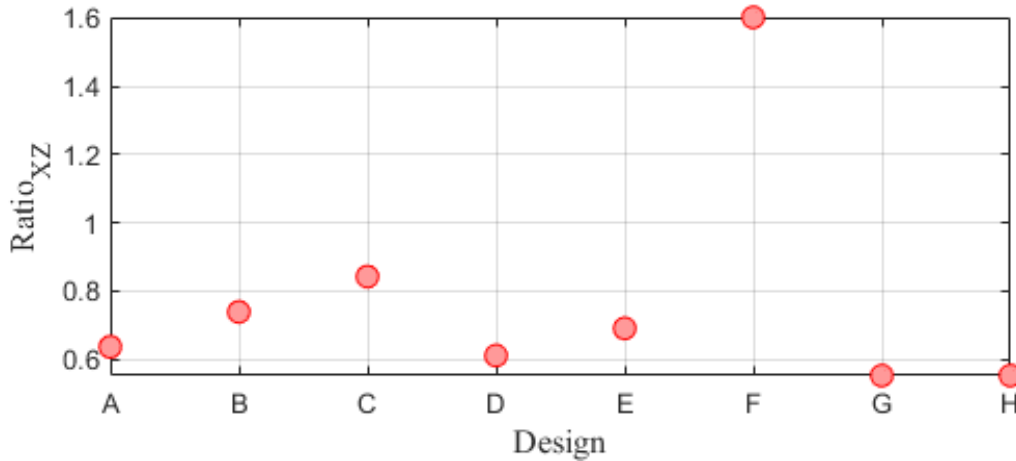


Figure 5.5. Ratio R_{xz} across all tested designs.

We consider R_{xz} of the two cylinders as a baseline for this comparison (0.55), in this case meaning no torsional reinforcement. Designs A and D showed ratio R_{xz} close to cylinders. Design F shows the highest ratio R_{xz} of 1.6, which is 2.9 times higher than R_{xz} of the cylinders (Fig. 5.5).

Analysis of collected data facilitated selection of two designs with desired mechanical features. *Design D* experiences the highest variability in bending stiffness between XZ and YZ axes (R_{xy}), while its torsional stability (R_{xz}) is close to a cylinder. Design F shows the greatest torsional stability (R_{xz}) of all samples and relatively high bending stiffness variability.

5.3.1.3 Payload

Additionally, the two selected designs (D and F) were tested with weights attached to their tips (0.1 g, 0.2 g, 0.3 g, 0.4 g, 0.5 g) and actuated at 2.5 mT, 5 mT and 7 mT on their preferred bending plane. Bending angles achieved with loaded tips were compared to bending angles extracted from tests with no payload. We observed similar trends in bend reduction in the two designs with addition of load at the tip. The maximum deflection achieved with maximum load (0.5 g) at the tip was 16° and 19° respectively for designs D and F, while unloaded cylinder H achieved maximum deflection of 14° under the same magnetic field (Fig 5.6).

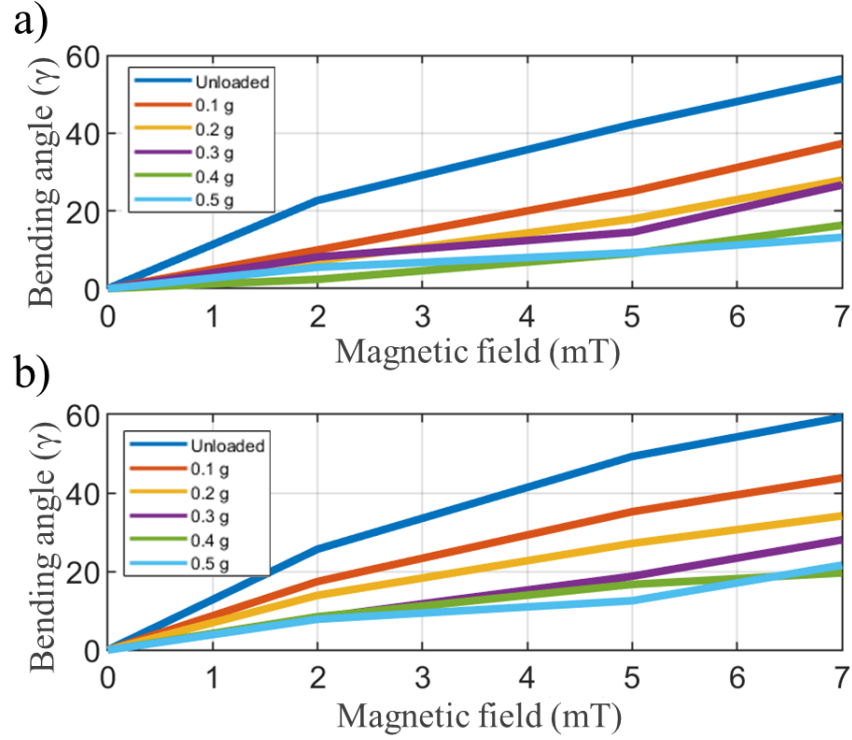


Figure 5.6. Bending angle in the low stiffness axis of designs D (a) and F (b) with payload at tip from 0 g to 0.5 g.

5.3.1.4 Independent Actuation

Selected Designs *D* and *F* were tested in parallel configurations to demonstrate capability of independent actuation under uniform magnetic field conditions in the same workspace. The two SMMs were placed in the workspace of 1D Helmholtz coil at 2.2 cm distance (center to center) and a uniform magnetic field was applied in X direction (Fig.5.7). We tested two actuation cases for both designs. The first case demonstrated instability of one manipulator (orthogonally magnetized) and bending on its high stiffness plane, while the second case included the same instability combined with bending on low stiffness plane in the same workspace.

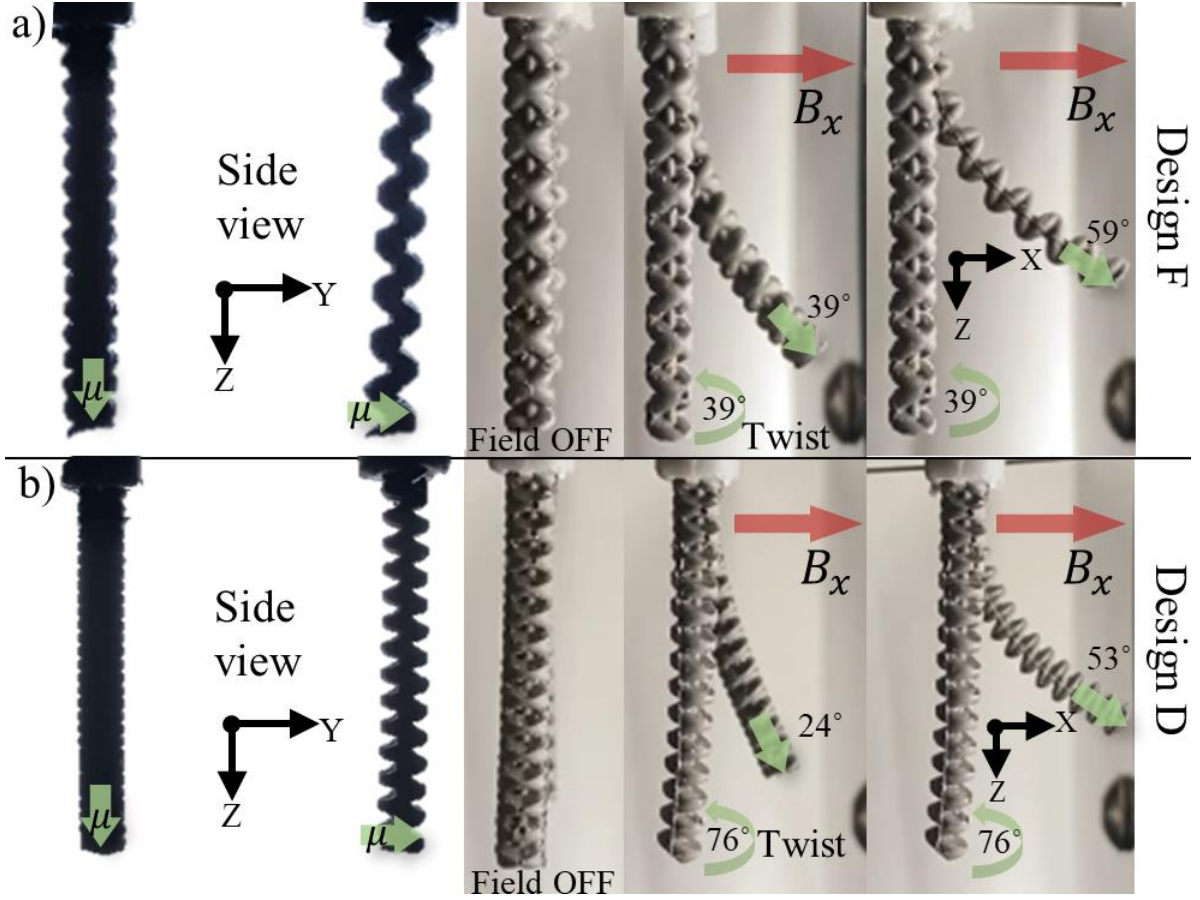


Figure 5.7. Dual Manipulator configuration. a) Design F; b) Design D; black frames represent global reference frame; green arrows represent direction of SMM's magnetization vector; red arrows represent applied magnetic field direction. The left side presents view on the YZ plane, showing the separation distance in the workspace, while right side of the figure shows view on the XZ plane of the workspace where bending is easier to observe.

We additionally demonstrated a configuration of three manipulators in one workspace, where two of the three manipulators were magnetized axially with their reinforcing planes arranged orthogonally (Fig. 5.8). This configuration demonstrates all three basic actuation modes of a reinforced SMM in the same workspace: bending on the reinforced plane, pure twist and bending on preferred plane. Similarly, as in dual manipulator configuration (Fig 5.7), we observe no inter-manipulator attraction at this separation distance. We excluded static SMM mode from this demonstration, where its magnetization vector aligns with applied magnetic field.

Due to no magnetic interaction at tested distance and assumption of uniformity of magnetic field in the workspace, the bending angles tested in multi-SMM configurations in this section are assumed to be the same as in single-SMM tests in sections IIIA 1) and IIIA 2).

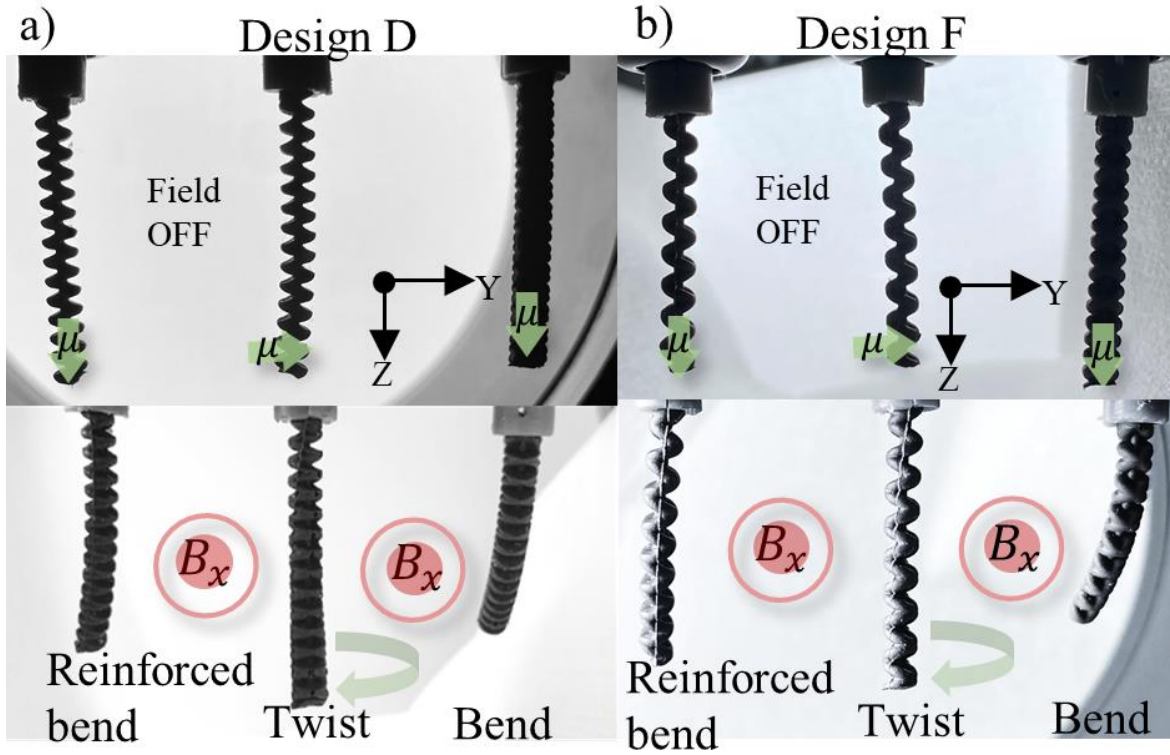


Figure 5.8. Triple manipulator configuration, showcasing three basic actuation modes in the same workspace. Black arrows represent global reference frame.

5.4 Discussion and Future Work

All SMMs reinforced with a double helix showed improved bending capabilities in one of the axes, in comparison to a cylindrical SMM of the same diameter (Fig. 5.4). Designs D and F both exhibit desired mechanical features showing their suitability to be applied in multiple SMM scenarios. Design D was characterized with 2.6 times higher ratio R_{xy} than a cylinder, meaning the deflection angle on the non-constrained plane is on average 2.6 higher than on the constrained plane.

Design F showed the highest ratio R_{xz} of 1.6, meaning that on average this design experiences 1.6 higher deflection in the preferred direction than it experiences twist about its longitudinal axis. Moreover Design F is 2.9 times more torsionally stable than cylinders (designs G and H). Both of the selected designs feature maximum R values (Table 5.1, Fig. 5.1), leading to the conclusion that only designs with high helix density should be considered in future works. Additionally, the two selected designs tested with tips loaded with 0.1 g – 0.5 g showed higher deflection than an unloaded cylinder of the same diameter under the same magnetic field exposure.

Demonstration of dual SMM configurations of designs D and F confirmed properties tested in single-segment studies, showing a better planar reinforcement in Design D and better torsional reinforcement in Design F.

We observed no attraction at the tested separation distance; however, it is expected that reducing the spacing will cause some level of attraction between the manipulators, especially when bending towards each other (as previously shown in work presented in Chapter 4).

Additionally, depending on the magnetic profile directions of the SMMs and on their arrangement in space, the possibility of attraction might increase e.g. in cases where the south pole of one agent will be directly facing north pole of the other. Such interactions will have crucial influence on independent actuation when scaling down, as well as in scenarios with small separation distance. Understanding and mitigating these inter-manipulator relationships will be a subject of further work.

Since the aim of this study was to characterize the influence of geometrical parameters on SMM performance, we have focused on separating motions of bending and twisting.

However, in complex actuation scenarios, twists can occur out of plane while the SMM is deflecting and therefore a design with both features would be expected to improve overall stability. Additionally, to fully characterize the designs, it would be of benefit to investigate bending capabilities when magnetic field is applied at a different angle and direction than tested in this paper, since this study was limited to uni-directional field application.

We chose to use a 1D Helmholtz coil for the characterization tests due to its ease of use and straightforward setup. However, this system had limitations, particularly a smaller workspace compared to more advanced systems like the dEPM. As a result, we were unable to test all bending primitives within this experimental setup. Further studies exploring available workspace area with all available DoFs with dual and triple SMM set ups should be explored with more advanced magnetic field and gradient generating system such as dEPM or 3D electromagnetic coil.

We also plan to develop a simulation-based optimization to create a more exhaustive search of possible designs when arranged in series and in parallel.

5.5 References

- [1] M. McCandless, A. Perry, N. DiFilippo, A. Carroll, E. Billatos, and S. Russo, “A soft robot for peripheral lung cancer diagnosis and therapy,” *Soft Robot.*, vol. 9, no. 04, 2021, doi: 10.1089/soro.2020.0127.
- [2] P. E. Dupont et al., “A decade retrospective of medical robotics research from 2010 to 2020,” *Sci. Robot.*, vol. 6, no. 60, 2021, doi: 10.1126/scirobotics.abi8017.
- [3] T. Da Veiga et al., “Challenges of continuum robots in clinical context: A review,” *Prog. Biomed. Eng.*, vol. 2, no. 3, 2020, doi: 10.1088/2516-1091/ab9f41.
- [4] M. Runciman, A. Darzi, and G. P. Mylonas, “Soft Robotics in Minimally Invasive Surgery,” *Soft Robot.*, vol. 6, no. 4, pp. 423–443, 2019, doi: 10.1089/soro.2018.0136.
- [5] G. Z. Lum et al., “Shape-programmable magnetic soft matter,” *Proc. Natl. Acad. Sci. U. S. A.*, vol. 113, no. 41, pp. E6007–E6015, Oct. 2016, doi: 10.1073/pnas.1608193113.
- [6] A. Bacchetti et al., “Optimization and fabrication of programmable domains for soft magnetic robots: A review,” *Front. Robot. AI*, vol. 9, no. November, pp. 1–10, 2022, doi: 10.3389/frobt.2022.1040984.
- [7] Y. Kim et al., “Telerobotically Controlled Magnetic Soft Continuum Robots for Neurovascular Interventions,” *Proc. - IEEE Int. Conf. Robot. Autom.*, pp. 9600–9606, 2022, doi: 10.1109/ICRA46639.2022.9812168.
- [8] G. Pittiglio et al., “Patient-Specific Magnetic Catheters for Atraumatic Autonomous Endoscopy,” *Soft Robot.*, vol. 9, no. 6, pp. 1120–1133, 2022, doi: 10.1089/soro.2021.0090.
- [9] V. K. Michiel Richter, Mert Kaya, Jakub Sikorski, Leon Abelmann, Venkiteswaran and S. Misra, “Magnetic Soft Helical Manipulators with Local Dipole Interactions for Flexibility and Forces,” *Soft Robotics*, vol. 10, no. 03, pp. 1–13, 2022, doi: 10.1089/soro.2022.0031.

-
- [10] C. M. Heunis, Y. P. Wotte, J. Sikorski, G. P. Furtado, and S. Misra, “The ARMM System - Autonomous Steering of Magnetically-Actuated Catheters: Towards Endovascular Applications,” *IEEE Robot. Autom. Lett.*, vol. 5, no. 2, pp. 704–711, 2020, doi: 10.1109/LRA.2020.2965077.
- [11] D. Lin, J. Wang, N. Jiao, Z. Wang, and L. Liu, “A Flexible Magnetically Controlled Continuum Robot Steering in the Enlarged Effective Workspace with Constraints for Retrograde Intrarenal Surgery,” *Adv. Intell. Syst.*, vol. 3, no. 10, p. 2000211, 2021, doi: 10.1002/aisy.202000211.
- [12] G. Pittiglio et al., “Personalized magnetic tentacles for targeted photothermal cancer therapy in peripheral lungs,” *Nat. Commun. Eng.*, vol. 2, no. 50, pp. 1–13, 2023, doi: 10.1038/s44172-023-00098-9.
- [13] S. Tottori, L. Zhang, K. E. Peyer, and B. J. Nelson, “Assembly, disassembly, and anomalous propulsion of microscopic helices,” *Nano Lett.*, vol. 13, no. 9, pp. 4263–4268, 2013, doi: 10.1021/nl402031t.
- [14] E. Diller, J. Giltinan, and M. Sitti, “Independent control of multiple magnetic microrobots in three dimensions,” *Int. J. Rob. Res.*, vol. 32, no. 5, pp. 614–631, 2013, doi: 10.1177/0278364913483183.
- [15] I. S. M. Khalil et al., “Independent Actuation of Two-Tailed Microrobots,” *IEEE Robot. Autom. Lett.*, vol. 3, no. 3, pp. 1703–1710, 2018, doi: 10.1109/LRA.2018.2801793.
- [16] J. Giltinan, P. Katsamba, W. Wang, E. Lauga, and M. Sitti, “Selectively controlled magnetic microrobots with opposing helices,” *Appl. Phys. Lett.*, vol. 116, no. 13, 2020, doi: 10.1063/1.5143007.

-
- [17] P. Katsamba and E. Lauga, “Micro-Tug-of-War: A Selective Control Mechanism for Magnetic Swimmers,” *Phys. Rev. Appl.*, vol. 5, no. 6, 2016, doi: 10.1103/PhysRevApplied.5.064019.
- [18] E. Diller, S. Floyd, C. Pawashe, and M. Sitti, “Control of multiple heterogeneous magnetic micro-robots on non-specialized surfaces,” *Proc. - IEEE Int. Conf. Robot. Autom.*, vol. 28, no. 1, pp. 115–120, 2011, doi: 10.1109/ICRA.2011.5979785.
- [19] S. Miyashita, E. Diller, and M. Sitti, “Two-dimensional magnetic micro-module reconfigurations based on inter-modular interactions,” 2013, doi: 10.1177/0278364913479837.
- [20] M. Salehizadeh and E. Diller, “Two-agent formation control of magnetic microrobots in two dimensions,” *J. Micro-Bio Robot.*, vol. 12, no. 1–4, pp. 9–19, 2017, doi: 10.1007/s12213-017-0095-5.
- [21] M. Salehizadeh and E. Diller, “Optimization-Based Formation Control of Underactuated Magnetic Microrobots via Inter-Agent Forces,” in *International Conference on Manipulation, Automation and Robotics at Small Scales (MARSS)*, IEEE, 2017. doi: doi: 10.1109/MARSS.2017.8001910. Independent Control of Two Magnetic Robots using External Permanent Magnets: A Feasibility Study," 2023 International Symposium on Medical Robotics (*ISMR*), Atlanta, GA, USA, 2023, pp. 1-7, doi: 10.1109/ISMR57123.2023.10130246.
- [23] Z. Koszowska et al., “Independently Actuated Soft Magnetic Manipulators for Bimanual Operations in Confined Anatomical Cavities.”, *Adv. Intell. Syst.*, 6: 2300062, 2023
- [24] G. Pittiglio, M. Brockdorff, T. da Veiga, J. Davy, J. H. Chandler, and P. Valdastrì, “Collaborative Magnetic Manipulation via Two Robotically Actuated Permanent Magnets,” *IEEE Trans. Robot.*, pp. 1–12, 2022, doi: 10.1109/TRO.2022.3209038.

-
- [25] P. Lloyd et al., “Feasibility of Fiber Reinforcement Within Magnetically Actuated Soft Continuum Robots,” *Front. Robot. AI*, vol. 8, no. July, pp. 1–10, 2021, doi: 10.3389/frobt.2021.715662.
- [26] P. Lloyd, O. Onaizah, G. Pittiglio, D. K. Vithanage, J. H. Chandler, and P. Valdastrì, “Magnetic Soft Continuum Robots With Braided Reinforcement,” *IEEE Robot. Autom. Lett.*, vol. 7, no. 4, pp. 9770–9777, 2022, doi: 10.1109/LRA.2022.3191552.
- [27] M. Manti, V. Cacucciolo, and M. Cianchetti, “Stiffening in soft robotics: A review of the state of the art,” *IEEE Robot. Autom. Mag.*, vol. 23, no. 3, pp. 93–106, 2016, doi: 10.1109/MRA.2016.2582718.
- [28] Y. J. Kim, S. Cheng, S. Kim, and K. Iagnemma, “A novel layer jamming mechanism with tunable stiffness capability for minimally invasive surgery,” *IEEE Trans. Robot.*, vol. 29, no. 4, pp. 1031–1042, 2013, doi: 10.1109/TRO.2013.2256313.
- [29] C. Chautems, A. Tonazzini, Q. Boehler, S. H. Jeong, D. Floreano, and B. J. Nelson, “Magnetic Continuum Device with Variable Stiffness for Minimally Invasive Surgery,” *Adv. Intell. Syst.*, vol. 2, no. 6, p. 1900086, 2020, doi: 10.1002/aisy.201900086.

Chapter 6 Stability in SMMs

Chapter source: A Pneumatic Anchoring Mechanism for Improved Stability in Soft Magnetic Manipulators for Surgery; Z Koszowska, M Brockdorff, P R Lloyd, J H Chandler and P Valdastri; 2024, Manuscript submitted to Robosoft, IEEE

Abstract

This paper presents a synergistic soft robotic actuation approach, whereby pneumatically induced anchoring is applied to a Soft Magnetic Manipulator (SMM) to enable improved post navigation stability and tip manipulation accuracy. A SMM is equipped with an integrated pneumatic expansion chamber (anchor) and tool channel to enhance stability during interventional procedures. The pneumatic anchor is tested for its position-locking effectiveness during SMM tip loading. Additionally, tip manipulation stability with and without the anchoring system activated is assessed by measurement of the SMM's ability to trace a parametric circle using an integrated laser fiber. The anchoring mechanism showed a mean improvement in tip actuation accuracy of 73.26%. The system is further demonstrated in the case study of a brain phantom, with the prototype equipped with a laser fiber. The SMM was navigated through a brain fold through application of external magnetic fields exploiting the dual External Permanent Magnet (dEPM) platform. Upon arrival at target site, the anchor was deployed to stabilize the SMM's tip while laser targeting was performed, demonstrating the potential of this approach for procedures requiring high precision.

6.1 Introduction

Minimally Invasive surgery (MIS) when accessing brain lesions provides major benefits over an open skull surgery. MIS approaches work well for brain tumors or aneurysms located near the brain surface or where access is possible via a straight path. However, in cases where tumors are in areas of the brain where straight tool trajectory would lead to penetration of brain tissues crucial in function, this approach is not feasible. In such cases, surgeons either opt for a traditional open craniotomy approach or simply deem the tumor inaccessible [1].

The field of soft robotics is facilitating expansion of keyhole surgery in the brain, for deeper brain access [2], [3]. Soft continuum robots, usually driven by means of pneumatics [4]–[6] or hydraulics [7], [8], and manufactured with elastomeric materials offer greater flexibility and less traumatic tissue interaction over current endoscopic tools [9]. This can open the possibility of navigating to the targeted area, between brain folds (known as sulci and fissures), as opposed to penetrating through the brain volume, allowing access to brain tumors located in difficult areas and significantly minimizing invasiveness of such procedures. This ensures that collateral damage to brain areas responsible for vital functions is minimized during surgery. While the concept of utilizing elastomeric devices is promising to overcome limitations in neurosurgery, there are numerous outstanding challenges. The available DoFs using popular actuation methods in soft structures are limited, especially at the required scale. Miniaturization of such devices to millimeter scale is challenging due to the limits of scaling down the components of actuating systems such as air connections, tubing, wires etc. This becomes even more significant in devices requiring high maneuverability, where more components are implemented in the design [10].

Stimuli-responsive materials can induce shape deformation under external actuation trigger such as magnetic field, pH gradient, ultrasonication or temperature. The significant advantage of such

materials is in miniaturization potential, since they often eliminate the need for onboard actuation components such as motors, wires, pressure connections or tubing. An example of a smart material that can be applied in medical devices is in Soft Magnetic Manipulators (SMMs), where the addition of magnetic particles to an elastomeric matrix makes them responsive to external magnetic fields. This has been explored in medical applications by multiple research groups [11]–[13]. The miniaturization potential of SMMs combined with the material modulus close to that of soft tissue present clinical benefits including minimized interaction with the surrounding anatomy and deep access to human body [9], [14]. SMMs can be divided into two categories: tip magnetized and continuously magnetized. Magnetization along the length of the manipulator's body can be either axial or off-axis, providing a signature magnetic profile, e.g. suited for a specific anatomy or patient as in [15], [16], making them a good fit for navigating in complex paths. Tip magnetized manipulators, however, are better suited for applications in less tortuous pathways, where tip maneuverability and/or simplicity of operation is prioritized. The advantage of this approach is that due to the simple magnetic profile the tip can be easily controlled in multiple Degrees Of Freedom (DoFs) with magnetic gradients, even with a handheld magnet as in [17]. This multi-DoF tip actuation is challenging for continuously magnetized SMMs, due to the fundamental connection between internal magnetization and external applied field. Movement of the whole SMM's length when attempting tip only actuation is inevitable. Even if magnetic separation were possible, the movement of the tip would lead to uncontrollable movement of the more proximal region of the body due to their mechanical connection. Due to this phenomenon, applying stiffening approaches in SMMs would not only improve stability for high-payload tasks but also enable the highly desirable separation of the tip actuation from actuation of the SMM's body.

Structural compliance and softness are beneficial during navigation in delicate tissues, however, in cases where a procedure requires localized and accurate tip control could present itself as a disadvantage. Due to the compliant nature of elastomeric robotic devices, tasks such as biopsy can also pose challenges due to material buckling under load. Addressing this pivotal challenge in soft robotics has led to numerous efforts aimed at stiffening soft robots on demand. Temperature responsive materials [18], various material jamming and locking techniques [19]–[22] and even embedded chain mail [23] have all been demonstrated but invariably suffer from difficulties either related to unsafe transition temperatures or challenges in miniaturization [24]. For devices to gain needed stability to transmit forces essential to perform surgical tasks, researchers have also explored mechanical anchoring approaches such as pneumatic balloon [25], mechanical expandable structure [26] or magnetic anchoring [27], [28].

In this work, we present a novel design of a soft magnetic manipulator (SMM) aimed at improving movement stability and independent tip control during magnetic actuation. We modified a previously presented SMM design [16] by adding a fully integrated pneumatic chamber, inspired by balloon catheters used to anchor within anatomical structures. This monolithic design facilitates smooth navigation and deployment of the anchor on demand. The inflated anchor allows for independent control of the tip, stabilizing the rest of the device in the anatomy, when the tip is in motion (Figure 1). Additionally, the tip can be actuated with precision, as the balloon functions as a stiffened section, comparable to approaches presented above. This prevents movements from the proximal SMM body from being transmitted beyond the balloon to the tip, which would otherwise cause disturbances in standard actuation scenarios without an anchoring mechanism.

Hence, by combining pneumatic anchoring with magnetic manipulation, our approach improves post-navigation stability and tip accuracy, offering a more controlled and stable magnetic actuation solution.

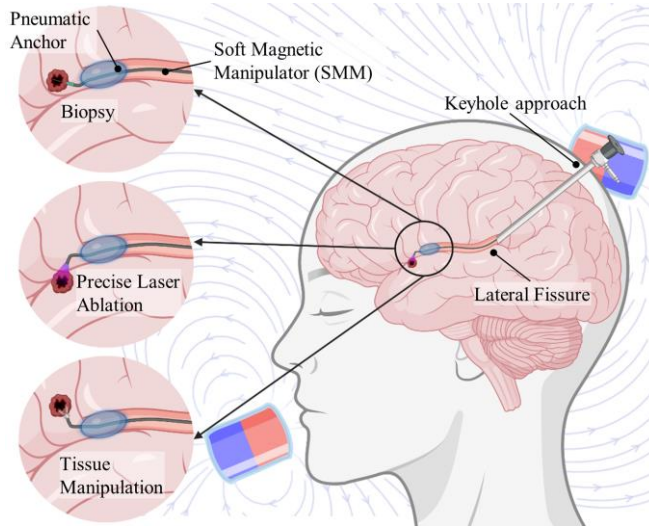


Figure 6.1. Proposed Soft Magnetic Manipulator (SMM) with an anchor, in a dEPM set up, enabling potential applications in Minimally Invasive Surgery such as biopsy, precise laser ablation and tissue manipulation.

6.2 Pneumatic-Magnetic Multi-Modal SMM Approach

The presented prototype is 4 mm in diameter, with a thinner tip (2 mm) for improved deflection. The length of the tip is 15 mm, and the whole manipulator is 30 mm long. Design parameters of this prototype are guided by the clinical application of navigating through and anchoring in the lateral fissure of the brain, which varies between ~5.5 mm to 9 mm in a surgical training simulator used in this work (UpSurgeOn, Italy). However, the length of maneuverable tip, as well as balloon diameter and wall thickness can be adjusted at the design stage depending on specific application, and the size of lumen/cavity in which the anchor will be deployed.

6.3 Operational Principles

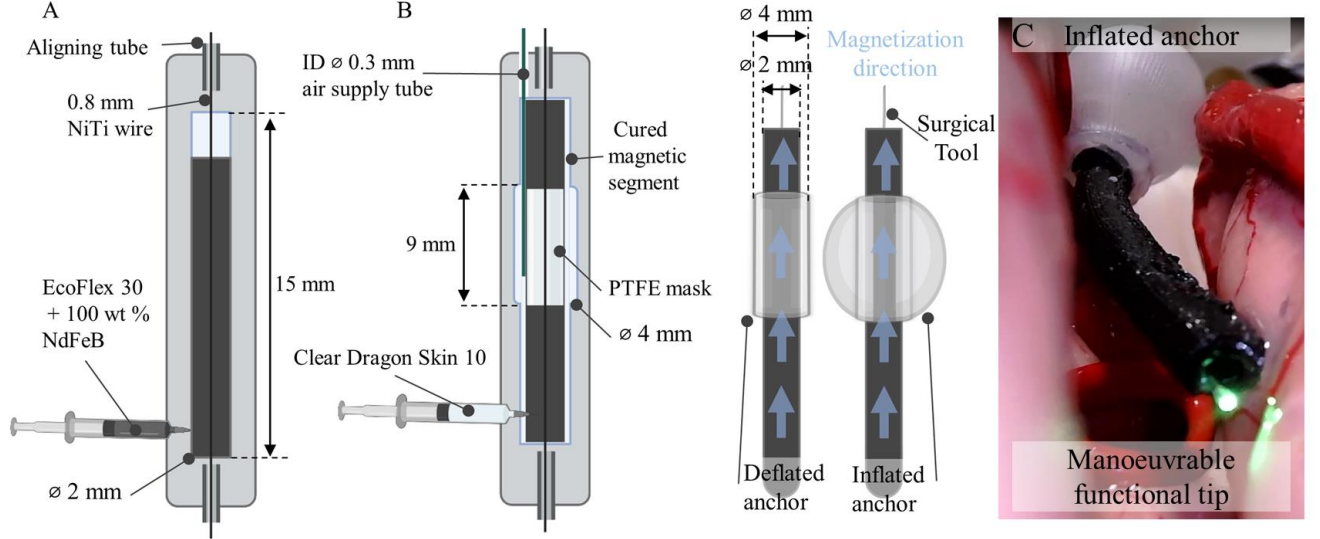


Figure 6.2. A. Molding process of the 2 mm magnetic core with a tool channel. B. Molding process of the pneumatic chamber, by injecting a layer of clear silicone over the cured magnetic core, in a secondary mold with cavity for chamber of 4 mm in diameter. C. Prototyped SMM with the deployed anchor and laser fiber in the tool channel.

6.3.1 Principles of Magnetic Actuation

A magnetic agent with magnetization $\boldsymbol{\mu} \in \mathbb{R}^3$ is subject to a magnetic force ($\boldsymbol{f} \in \mathbb{R}^3$) and torque ($\boldsymbol{\tau} \in \mathbb{R}^3$) under an applied field $\boldsymbol{B} \in \mathbb{R}^3$, respectively as:

$$\boldsymbol{f} = \nabla (\boldsymbol{\mu} \cdot \boldsymbol{B}) \quad (6.1)$$

$$\boldsymbol{\tau} = \boldsymbol{\mu} \times \boldsymbol{B} \quad (6.2)$$

where ∇ is the gradient operator. The magnetization vector(s) of an SMM is a crucial element when it comes to magnetic actuation of soft structures. According to Equation (6.2) when the magnetization $\boldsymbol{\mu}$ of the magnetic body aligns with the applied external magnetic field direction, it is subject to no resultant torque (no actuation). If the direction of $\boldsymbol{\mu}$ is not parallel with the external magnetic field vector \boldsymbol{B} a resultant magnetic torque will be present on the body; expressed as the cross product of the magnetization direction and applied external magnetic field (2). Using this

phenomenon, a SMM can be pre-programmed in a manner to achieve desired deformation, when exposed to specific external magnetic fields.

6.3.2 Pneumatic Chamber Design and Fabrication

Pneumatic actuators commonly feature chambers in the form of hollow silicone structures, utilizing their axial space for inflation. However, in the context of functionalizing the core of the SMMs a different approach is required. Here, to pass surgical tools, the inflating chamber must be either offset from center or placed concentrically around the device.

Fabricating the chamber separately from the SMM and assembling it with prefabricated magnetic segments poses multiple challenges in terms of the process and assembly.

Therefore, a standard fabrication technique for magnetic segment with tool channels as in e.g. [16] was adapted to cast the balloon around the SMM. This modification additionally enhances the versatility of the proposed system, enabling its integration with various types of SMMs.

The anchor consisting of a pneumatic chamber was designed to fit around a 2 mm magnetic segment. The anchor is fully integrated into SMM, meaning that the diameter of the core segment defines the diameter of the chamber core. The first step involved fabricating a magnetic segment of 2 mm diameter and 15 mm in length, by casting, with 3D printed molds (Grey V4 resin, Form III, Formlabs III, USA). Equal parts of elastomer (EcoFlex 30, Smooth-On, Inc., U.S.A.) A and B were mixed with 100 wt\% of hard magnetic micro-particles (Nd-FeB with an average 5 μm diameter and intrinsic coercivity of $H_{ci} = 9.65 \text{ kOe}$, MQFP-B+, Magnequench GmnH, Germany). The magnetic slurry was then mixed in a high vacuum-mixer (ARV- 310, ThinkyMixer, Japan) for 90 seconds at a speed of 1400 rpm and pressure of 20.0 kPa. The degassed mixture was injected

into closed cylindrical molds with a 0.8 mm NiTi wire fixed concentrically along the length of the cavity to create a tool channel. The part was cured at 45°C for 30 minutes.

PTFE tape (75 μm thick by 9 mm wide) was wrapped around the mid part of the magnetic segment to act as a mask in a second stage of the molding process, as in [25]. The silicone- silicone bond can only be achieved in areas where no PTFE is applied, creating a chamber where the mask is present, as depicted in Figure 6.2.

The magnetic segment with applied mask was aligned in the secondary mold, ensuring that the vertical NiTi wire was placed in the alignment slots on both sides of the mold. Alignment is crucial to create a chamber with even wall thickness, allowing for uniform inflation and concentric balloon profile. This was ensured by printing molds with alignment slots using 25 μm resolution in 3D printer settings. Additionally steel tubes with (ID) of 0.9 mm were pressure fit into the alignment cavities in the molds. The steel tubes accommodate the 0.8 mm NiTi, passing through the segment providing concentric alignment of the core in the mold (Figure 6.2). A silicone tube (0.3 mm ID and 0.5 mm OD) was aligned on top of the magnetic segment as an air inlet and secured with an extra layer of PTFE. This was passed through a hole designed in the mold beforehand. 0.2 mm NiTi wire was inserted into the air inlet tube to prevent silicone blocking the tube while injecting. The mold was closed and clamped, followed by injection with a clear (undoped) layer of DragonSkin 10 Slow (Smooth-On, Inc., U.S.A). Upon careful demolding, NiTi wires were removed from the air supply tube and from the core.

EcoFlex 30 was chosen as the material for the core and tip because of its low elastic modulus and consequent capability to achieve high deflection angles, even when mixed with 100% NdFeB [29]. The balloon was molded with DragonSkin 10 due to improved durability upon inflation, as compared to EcoFlex materials.

This fabrication process resulted in a 4 mm SMM with a 2 mm magnetic core, 0.8 mm tool channel and inflatable chamber with a wall thickness of 1 mm as shown in Figure 6.2. This process can be easily adapted to suit various surgical demands for the SMM, including total diameter, tool channel size, as well as different geometries of the balloon.

6.4 Results

6.4.1 The Anchor Experiment

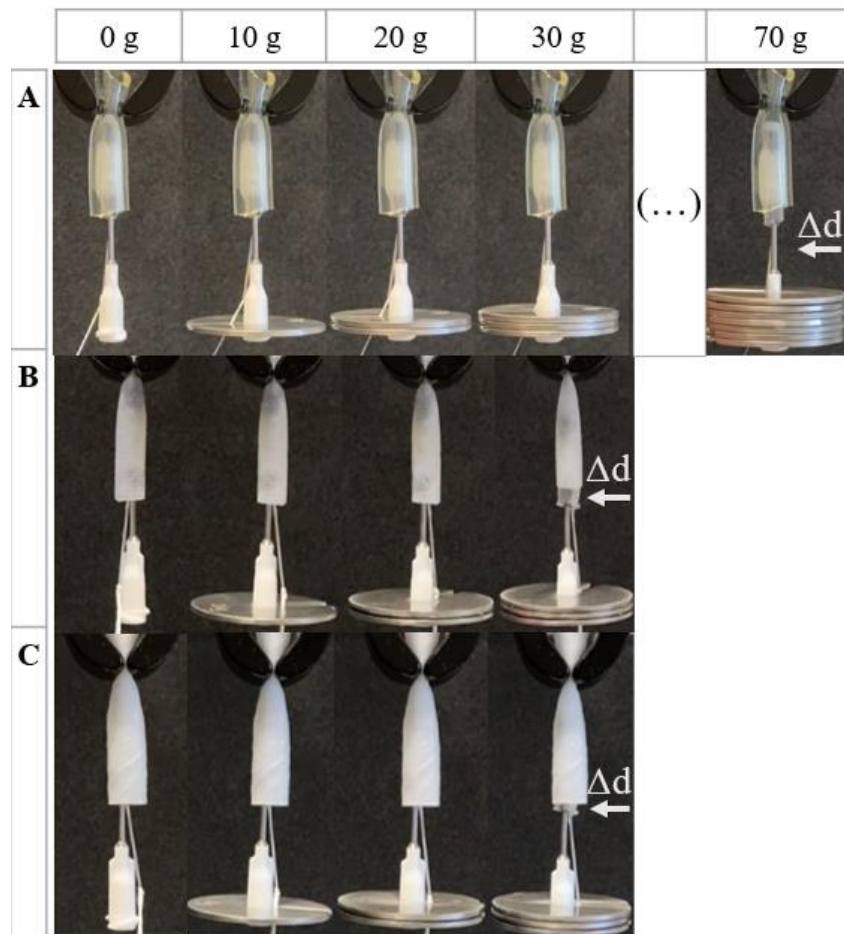


Figure 6.3. A mass was hung from the inflated SMM anchored in tubes of different diameters and lubrication. Results of anchoring evaluation tests where Δd is SMM's displacement; A. Dry 6 mm silicone tube. B 6 mm (ID) Carotid Artery Phantom. C. 10 mm (ID) Saphenous Vein Phantom.

A representative prototype was evaluated for its anchoring strength by incrementally loading the inflated SMM. To simulate clinically relevant experimental conditions, the prototype was tested in phantoms with mechanical properties resembling those of human tissues, including a 6 mm (ID) Carotid Artery Phantom and 10 mm (ID) Saphenous Vein Phantom (Syndaver.com), as well as a dry silicone tube with 6mm ID. The phantoms were kept in water with dish soap as per manufacturers guide, creating a slippery surface on the inside. In each experiment, a phantom was secured vertically, and the anchor was deployed by supplying the chamber with 12 ml of air volume. The pneumatic connections were maintained the same throughout all experiments. Incremental loads (10 g) were added to the tip of the SMM until anchor displacement, Δd (Figure 6.3).

Figure 6.3 shows that the tested prototype supported the most mass at the tip in a dry tube of 6 mm. The anchor failed at 70 g load. Lower friction in the phantoms in comparison to a dry tube caused the balloon to slip out of the lumens at 30 g load in both tested phantoms.

6.4.2 Tip Independence

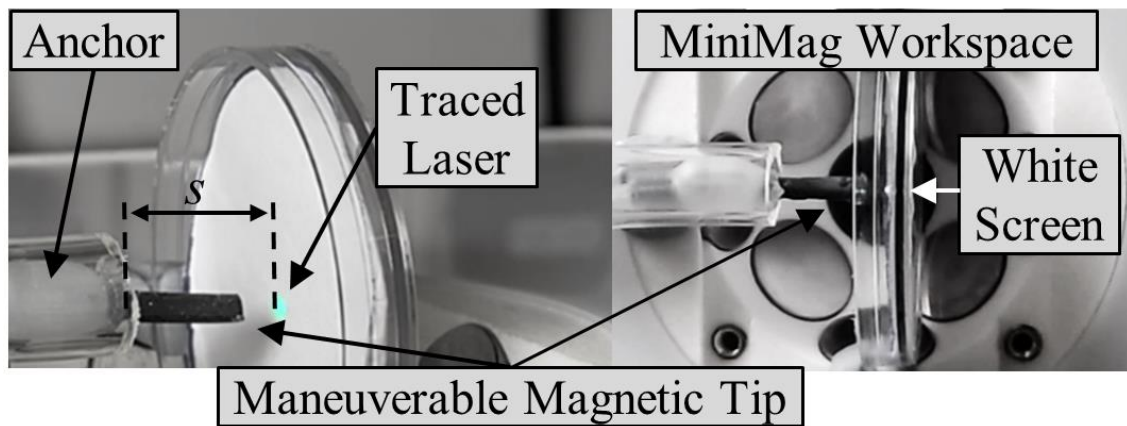


Figure 6.4. Experimental set-up for testing manipulation independence of the SMM's tip, including MiniMag Workspace, phantom tube, SMM with an inflated anchor and screen for laser tracing.

To assess the independence of magnetically manipulating the SMM's tip with the inflated anchor, a series of tests were performed under transient, homogeneous magnetic actuation. The prototype manipulator was equipped with a multimode laser fiber with a total diameter of 0.5 mm (0.39 NA TECS-Clad Multimode Optical Fiber, ThorLabs, USA).

The SMM was placed in lumens (as in *Section IV A*) aligned in omnidirectional magnetic field generation platform (MGF-100, MagnebotiX, Switzerland) [30] originally along the X axis of the platform. An orthogonal field (in the Y-Z plane) was rotated about the SMM's long axis ($|\mathbf{B}| = 20$ mT, 0.5 Hz), a field which should theoretically draw a circle with the laser on a flat target oriented in the YZ plane.

The anticipated diameter of the circle was calculated based on a balance between magnetic torque (left hand side of equation 6.3) and beam bending torque (right hand side of equation 6.3), adapted from [31]

$$\mathbf{m} \times \mathbf{B} = \frac{EI}{L} \theta \quad (6.3)$$

Where \mathbf{m} is the magnetic moment of the manipulator (Am^2), \mathbf{B} the applied field (T), E the elastic modulus of the beam (Nm^{-2}), L the unconstrained length of the beam (15 mm) and I the second moment of area of the bending beam (m^4), defined as:

$$I = \frac{\pi d^4}{64} \quad (6.4)$$

The stiffness of the entire beam is the sum of the stiffnesses of the component parts, namely, the elastomer ($d_{\text{outer}} = 2$ mm, $d_{\text{inner}} = 0.8$ mm, $E = 360$ kPa [29]), the laser ($d = 0.2$ mm, $E = 50$ GPa [32]) and the Teflon sheath surrounding the laser ($d = 0.5$ mm, $E = 500$ MPa [33]). Theta is the

bending angle of the beam giving, assuming linearity, the resultant radius of the laser sketched circle of:

$$r_{circle} = s \cdot \sin \left(m \times B \cdot \left(\frac{L}{EI} \right) \right) \quad (6.5)$$

With s the distance from the base of the SMM's tip to the screen (Fig. 6.4). The data on the laser position was continuously captured with a camera (Basler, Germany) and repeated with the deflated and inflated anchor (12 ml air volume), in 3 ph antom lumens. Figure 6.5 presents the analysis of collected data, comparing laser points captured with camera to an expected circle based on Equation 6.5. It can be observed that the unanchored SMM was unable to draw a circle in all three tested cases. Collected data with unanchored SMM for “Silicone tube 6 mm” condition shows the drawn shape being the closest to the target circle from all tested cases. The Root Mean Square Error (RMSE) for the “Anchor OFF” condition was 1.72 mm while for the “Anchor ON” it was 0.46 mm, showing reduction of the RSME of 73.26%.

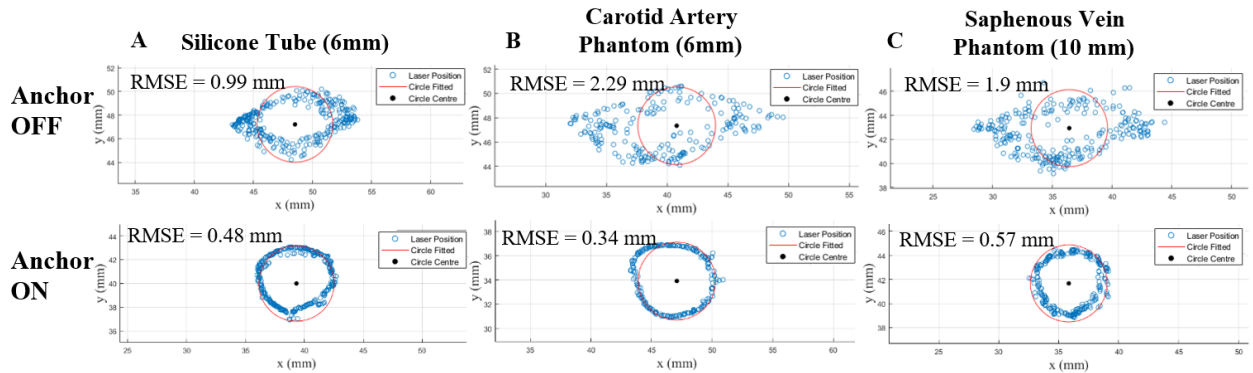


Figure 6.5. Results of a circle drawing task by anchored and unanchored SMMs in the MiniMag workspace under the same rotating magnetic field conditions $B_z = 20$ mT, 0.5 Hz. A. Silicone Tube 6 mm ID – dry. B. Lubricated Carotid Artery Phantom 6mm ID. C. Lubricated Saphenous Vein Phantom 10 mm ID.

6.5 Case Study: Demonstration in a Brain Phantom

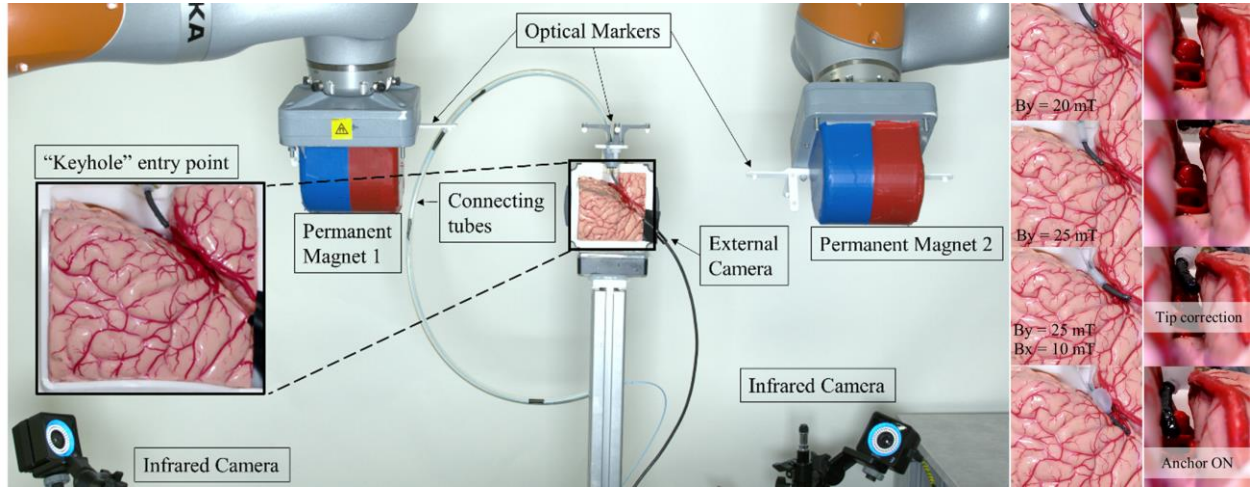


Figure 6.6. A. Experimental set-up including dual External Permanent Magnet (dEPM) platform, optical tracking system for calibration, brain phantom and SMM with its connections. B. Results of SMM testing in the brain phantom. From the top: navigation into the brain fold with manual insertion and magnetic field application, tip correction and inflation. More details in Supplementary Video 1.

To demonstrate clinical applicability of the proposed prototype, the system was tested in a brain phantom. The clinical assumption was made such that in a real case scenario, the SMM would enter through a keyhole in the skull, drilled aligned to a plane of the targeted brain fold, as the concept drawing in Figure 6.1 [1]. Following clinical requirements to access brain fold workspace, the manipulator in most cases follows a similar trajectory, navigating along the brain fold then bending inwards. In this paper we use a simulator of the brain with exposed lateral fissure. Hence, in this case we opted for a standard magnetic profile, magnetizing the SMM along its length (Fig. 6.2). Axial magnetic profile in this case is sufficient, providing needed deflection to bend along the lateral fissure and maneuver the tip upon anchor inflation. The magnetic profile, however, could readily be generalized for more complex navigations, where off-axis magnetization would be required.

A neurosurgical brain simulator (upsurgeon.com; model: AneurysmBox) was fixed in the dual External Permanent Magnet (dEPM) set up (Figure 6.6). Frames with optical markers were mounted at the top of the simulator, and on the permanent magnets, to facilitate calibration of the dEPM platform [34]. An external camera was mounted pointing into the fissure for visual feedback during the experiment. The SMM with anchor and laser fiber passing through the tool channel, was attached to a silicone tube with Silpoxy adhesive (Smooth-On, Inc., U.S.A.). The SMM was manually inserted into the workspace while applying magnetic field conditions: $B_y = [20 \text{ mT}; 25 \text{ mT}]$, (Figure 6.5B) (Table 6.1). At the last insertion step, additional field $B_x = [10 \text{ mT}]$ was applied to straighten the tip into required position (this can be seen in the Supplementary Video 1).

After insertion, the inflating mechanism was deployed by supplying the chamber with 12 ml of air, to stabilize the SMM to achieve actuation independence of the tip. The tip was then actuated by applying magnetic field conditions as in Table 6.1. This demonstration showed tip actuation as desired, without movement of the rest of SMM body. This can be seen in the Supplementary Video 1.

Table 6.1. Magnetic field conditions applied in the phantom workspace during the three stages of the experiment: Insertion, Tip Correction and Tip Actuation.

	B_x	B_y	B_z
Insertion	0	20 mT	0
	0	25 mT	0
Tip correction	10 mT	25 mT	0
Tip actuation	- 5 mT	0	0
	- 5 mT	15 mT	0
	- 5 mT	25 mT	0
	- 5 mT	10 mT	0
	- 5 mT	15 mT	0
		15 mT	0
	-10 mT	15 mT	0
	5 mT	15 mT	0
	-5 mT	15 mT	0

6.6 Discussion and Future Work

In this work, we presented a novel anchoring mechanism for SMMs, aiming at stabilizing a manipulator's body during surgical procedures, to allow independent and accurate actuation of the tip.

The experimental testing to evaluate anchoring strength of the presented approach showed that the design can support up to 70 g load at the tip for a dry tube and up to 30 g in lubricated phantom lumens. This shows a potential to use the anchor in medical settings where high payload at the tip is applied. In the future this capability should be further investigated and exploited by performing tasks requiring a payload at the tip, such as biopsy and penetration tasks (e.g. injections) in soft tissues. Additionally, the phantoms should be tested for their tribological properties to accurately evaluate anchoring properties depending on surface friction. It could be also beneficial to measure tissue deformation while the anchor is on.

The results provided for independent tip evaluation show improved accuracy of targeted motion in all tested cases with anchored SMM. Inaccuracies in control without anchor vary depending on the size of the lumen, as expected. However, in all presented cases, the anchor improved the accuracy of tip motion, 73.26 % on average. The RMSE is larger for unanchored SMM in phantom tubes. This is likely caused by the lubrication of lumens, creating more challenging conditions for anchoring, as opposed to the dry silicone tube.

The uneven shape of resultant tracked motion for the “Anchor OFF” condition observed in Figure 6.4 is caused by rotation of the body length of the SMM under the rotating field. Due to the lack of anchor, the whole body of the SMM twists in the tube, allowing for magnetic gradient to pull it towards bottom left side of the workspace, while it is turning clockwise and thus creates a skewed and noisy shape.

It should be noted that all results presented in this work correspond to one design of the SMM, featuring specific design parameters such as length, diameter, base material, and concentration of magnetic particles. Variation of these parameters will likely affect the maneuverability as well as stability when the anchor is on.

Clinical applicability was further demonstrated in a case study of a brain simulator, showing successful navigation with magnetic actuation, inflation in the lateral fissure and independent tip actuation.

For feedback while navigating in clinical scenarios, future research should involve using Fiber-Bragg sensors or similar running along the main axis of the manipulator. This can provide non-visual shape-feedback when navigating deep in the brain tissue, and therefore beyond visual range. Additionally, since NdFeB particles are cytotoxic, further investigation should involve either biocompatible coatings of the whole SMM or magnetic components prior to the fabrication process, or an alternative biocompatible hard magnetic material [35].

This system shows potential to be applied in a broad range of medical procedures, where stability is important, such as laser ablation, biopsies and tissue retrieval. The design is easy to modify, depending on application requirements. The placement of the anchor can be adjusted to suit the length requirements of segments that need to be separated. For applications where longer SMMs would be more beneficial, multiple balloons can be implemented for improved stability in a longer body. It would be of interest to implement multiple balloons and depending on required tip length in specific application, selectively activate, thus controlling the length of the unconstrained tip. The chamber design can be adjusted to anchor in various lumen diameters.

6.7 Acknowledgements

Research reported in this article was supported by the Engineering and Physical Sciences Research Council (EPSRC) under grants number EP/R045291/1 and EP/V009818/1, and by the European Research Council (ERC) under the European Union's Horizon 2020 research and innovation programme (grant agreement No 818045). Any opinions, findings and conclusions, or

recommendations expressed in this article are those of the authors and do not necessarily reflect the views of the EPSRC or the ERC.

6.8 References

- [1] W. S. Cho, J. E. Kim, H. S. Kang, Y. J. Son, J. S. Bang, and C. W. Oh, “Keyhole approach and neuroendoscopy for cerebral aneurysms,” *J. Korean Neurosurg. Soc.*, vol. 60, no. 3, pp. 275–281, 2017, doi: 10.3340/jkns.2017.0101.002.
- [2] M. Runciman, A. Darzi, and G. P. Mylonas, “Soft Robotics in Minimally Invasive Surgery,” *Soft Robot.*, vol. 6, no. 4, pp. 423–443, 2019, doi: 10.1089/soro.2018.0136.
- [3] T. Amadeo et al., “Soft Robotic Deployable Origami Actuators for Neurosurgical Brain Retraction,” *Front. Robot. AI*, vol. 8, no. January, pp. 1–12, 2022, doi: 10.3389/frobt.2021.731010.
- [4] J. H. Chandler, M. Chauhan, N. Garbin, K. L. Obstein, and P. Valdastri, “Parallel Helix Actuators for Soft Robotic Applications,” *Front. Robot. AI*, vol. 7, no. September, pp. 1–17, 2020, doi: 10.3389/frobt.2020.00119.
- [5] M. McCandless, A. Perry, N. DiFilippo, A. Carroll, E. Billatos, and S. Russo, “A soft robot for peripheral lung cancer diagnosis and therapy,” *Soft Robot.*, vol. 9, no. 04, 2021, doi: 10.1089/soro.2020.0127.
- [6] I. De Falco, M. Cianchetti, and A. Menciassi, “A soft multi-module manipulator with variable stiffness for minimally invasive surgery,” *Bioinspiration and Biomimetics*, vol. 12, no. 5, 2017, doi: 10.1088/1748-3190/aa7ccd.
- [7] F. Campisano et al., “Teleoperation and Contact Detection of a Waterjet-Actuated Soft Continuum Manipulator for Low-Cost Gastroscopy,” *IEEE Robot. Autom. Lett.*, vol. 5, no. 4, pp. 6427–6434, 2020, doi: 10.1109/LRA.2020.3013900.

-
- [8] J. Fras, Y. Noh, M. Macias, H. Wurdemann, and K. Althoefer, “Bio-Inspired Octopus Robot Based on Novel Soft Fluidic Actuator,” *Proc. - IEEE Int. Conf. Robot. Autom.*, pp. 1583–1588, 2018, doi: 10.1109/ICRA.2018.8460629.
- [9] T. Da Veiga et al., “Challenges of continuum robots in clinical context: A review,” *Prog. Biomed. Eng.*, vol. 2, no. 3, 2020, doi: 10.1088/2516-1091/ab9f41.
- [10] P. E. Dupont et al., “A decade retrospective of medical robotics research from 2010 to 2020,” *Sci. Robot.*, vol. 6, no. 60, 2021, doi: 10.1126/scirobotics.abi8017.
- [11] G. Z. Lum et al., “Shape-programmable magnetic soft matter,” *Proc. Natl. Acad. Sci. U. S. A.*, vol. 113, no. 41, pp. E6007–E6015, Oct. 2016, doi: 10.1073/pnas.1608193113.
- [12] Z. Li, O. Youssefi, and E. Diller, “Magnetically-guided in-situ microrobot fabrication,” *IEEE Int. Conf. Intell. Robot. Syst.*, vol. 2016-Novem, pp. 5131–5136, 2016, doi: 10.1109/IROS.2016.7759753.
- [13] J. Hwang et al., “An Electromagnetically Controllable Microrobotic Interventional System for Targeted, Real-Time Cardiovascular Intervention,” *Adv. Healthc. Mater.*, vol. 11, no. 11, 2022, doi: 10.1002/adhm.202102529.
- [14] Z. Li, J. Li, Z. Wu, Y. Chen, M. Yeerbulati, and Q. Xu, “Design and Hierarchical Control of a Homocentric Variable-Stiffness Magnetic Catheter for Multiarm Robotic Ultrasound-Assisted Coronary Intervention,” *IEEE Trans. Robot.*, vol. 40, pp. 2306–2326, 2024, doi: 10.1109/TRO.2024.3378442.
- [15] P. Lloyd et al., “A learnt approach for the design optimisation of magnetically actuated shape forming soft tentacle robots,” 2019.

-
- [16] G. Pittiglio et al., “Personalized magnetic tentacles for targeted photothermal cancer therapy in peripheral lungs,” *Nat. Commun. Eng.*, vol. 2, no. 50, pp. 1–13, 2023, doi: 10.1038/s44172-023-00098-9.
- [17] Y. Kim, G. A. Parada, S. Liu, and X. Zhao, “Ferromagnetic soft continuum robots,” 2019. [Online]. Available: <http://robotics.sciencemag.org/>
- [18] Y. Piskarev et al., “Fast-Response Variable-Stiffness Magnetic Catheters for Minimally Invasive Surgery,” vol. 2305537, pp. 1–14, 2024, doi: 10.1002/advs.202305537.
- [19] M. Brancadoro, M. Manti, F. Grani, S. Tognarelli, A. Menciassi, and M. Cianchetti, “Toward a variable stiffness surgical manipulator based on fiber jamming transition,” *Front. Robot. AI*, vol. 6, no. MAR, pp. 1–12, 2019, doi: 10.3389/frobt.2019.00012.
- [20] D. S. Shah, E. J. Yang, M. C. Yuen, E. C. Huang, and R. Kramer-Bottiglio, “Jamming Skins that Control System Rigidity from the Surface,” *Adv. Funct. Mater.*, vol. 31, no. 1, 2021, doi: 10.1002/adfm.202006915.
- [21] B. Yang et al., “Reprogrammable soft actuation and shape-shifting via tensile jamming,” *Sci. Adv.*, vol. 7, no. 40, pp. 1–11, 2021, doi: 10.1126/sciadv.abh2073.
- [22] J. Liu, L. Yin, J. H. Chandler, X. Chen, P. Valdastrì, and S. Zuo, “A dual-bending endoscope with shape-lockable hydraulic actuation and water-jet propulsion for gastrointestinal tract screening,” *Int. J. Med. Robot. Comput. Assist. Surg.*, vol. 17, no. 1, pp. 1–13, 2021, doi: 10.1002/rcs.2197.
- [23] Y. Wang, L. Li, D. Hofmann, J. E. Andrade, and C. Daraio, “Structured fabrics with tunable mechanical properties,” *Nature*, vol. 596, no. 7871, pp. 238–243, 2021, doi: 10.1038/s41586-021-03698-7.

-
- [24] M. Manti, V. Cacucciolo, and M. Cianchetti, “Stiffening in soft robotics: A review of the state of the art,” *IEEE Robot. Autom. Mag.*, vol. 23, no. 3, pp. 93–106, 2016, doi: 10.1109/MRA.2016.2582718.
- [25] D. Van Lewen, T. Janke, H. Lee, R. Austin, E. Billatos, and S. Russo, “A Millimeter-Scale Soft Robot for Tissue Biopsy Procedures,” *Adv. Intell. Syst.*, vol. 5, no. 5, 2023, doi: 10.1002/aisy.202200326.
- [26] J. Rogatinky et al., “A multifunctional soft robot for cardiac interventions,” *Sci. Adv.*, 2023, doi: 10.1126/sciadv.adi5559.
- [27] W. Li, T. Cheng, M. Ye, C. S. H. Ng, P. W. Y. Chiu, and Z. Li, “Kinematic Modeling and Visual Servo Control of a Soft-Bodied Magnetic Anchored and Guided Endoscope,” *IEEE/ASME Trans. Mechatronics*, vol. 25, no. 3, pp. 1531–1542, 2020, doi: 10.1109/TMECH.2020.2978538.
- [28] T. Cheng, X. Zhang, C. S. H. Ng, P. W. Y. Chiu, and Z. Li, “Design and Evaluation of a Soft-Bodied Magnetic Anchored and Guided Endoscope,” *J. Med. Robot. Res.*, vol. 03, no. 03n04, p. 1841007, 2018, doi: 10.1142/s2424905x18410076.
- [29] T. Da Veiga et al., “Material characterization for magnetic soft robots,” 2021 IEEE 4th Int. Conf. Soft Robot. RoboSoft 2021, pp. 335–342, 2021, doi: 10.1109/RoboSoft51838.2021.9479189.
- [30] B. E. Kratochvil et al., “MiniMag: A Hemispherical Electromagnetic System for 5-DOF Wireless Micromanipulation,” *Springer Tracts Adv. Robot.*, vol. 79, pp. 317–318, 2014, doi: 10.1007/978-3-642-28572-1.
- [31] P. Lloyd, G. Pittiglio, J. H. Chandler, and P. Valdastri, “Optimal Design of Soft Continuum Magnetic Robots under Follow-the-leader Shape Forming Actuation,” in *International Symposium on Medical Robotics (ISMR)*, 2020, pp. 111–117. doi: 10.1109/ismr48331.2020.9312943.

-
- [32] Schott Advanced Optics, “Mechanical and thermal properties of optical glass,” Tie-31, no. October, pp. 1–8, 2018.
- [33] Ideal-tek, “Engineering plastic type PTFE, Technical data sheet,” pp. 1–2.
- [34] G. Pittiglio, M. Brockdorff, T. da Veiga, J. Davy, J. H. Chandler, and P. Valdastrì, “Collaborative Magnetic Manipulation via Two Robotically Actuated Permanent Magnets,” *IEEE Trans. Robot.*, pp. 1–12, 2022, doi: 10.1109/TRO.2022.3209038.
- [35] A. Pena-Francesch et al., “Macromolecular radical networks for organic soft magnets,” *Matter*, 2024, doi: 10.1016/j.matt.2023.12.015.

Chapter 7 Discussion and Future Directions

This chapter provides a summary and discussion of the contributions presented in this thesis, as well as future directions for the research.

Summary of contributions

This thesis explores methods to overcome the limitations of endoscopic surgeries by enhancing endoscopic technologies using Soft Magnetic Manipulators (SMMs). Through a novel technique involving monolithic double helix reinforcement, torsional behavior in unstable actuation scenarios is mitigated. Additionally, methods for simultaneous actuation of two SMMs within a single anatomical and magnetic workspace are investigated, offering potential for independent actuation through specific magnetization profiles and local gradient fields. The extensive characterization study of the double helix reinforcement identifies optimal designs for addressing unstable actuation cases. Moreover, the integration of an inflatable pneumatic chamber within the SMM addresses the challenge of maintaining stability during clinical procedures, demonstrating a significant increase in accuracy and potential for precise control in clinical environments. These findings contribute to the advancement of endoscopic technologies, paving the way for improved surgical outcomes and patient care.

The primary focus of this thesis is to address the gap in research regarding the integration of magnetic continuum devices into surgical tasks. While these devices have been thoroughly investigated for their navigation methods, their application in surgical scenarios remains underexplored. Specifically, our goal is to explore methods for controlling two magnetically actuated tools within a single workspace using SMMs.

Chapter 4 presented two solutions addressing the challenge of actuating multiple SMMs in one magnetic and anatomical workspace. This work explored innovative design of a double helix, wrapped around a typical cylindrical shape of a magnetic catheter. The double helix provided needed reinforcement to minimize torsional behavior during scenarios of instability. Moreover, the resultant planar reinforcement, combined with specific magnetic design, allowed actuation of two SMMs in one workspace, for the first time. Additionally, an alternative approach was presented that utilized local magnetic gradient application on one of the manipulators, while keeping the second SMM static. Both approaches were experimentally evaluated for the available workspace. Despite the recognized constraints of the proposed methodologies, both strategies enabled independent motion of the two parallel manipulators across expansive areas (up to 0.55 and 0.32 cm² for the OM strategy and up to 0.45 and 0.56 cm² for the PM strategy). Eliminating the marker frames, necessary for tracking, would likely expand the attainable range of motion. Nonetheless, the successful manipulation of the tracker payload underlines the potential applicability of these methods for surgical tool manipulation within constrained anatomical spaces. Clinical applicability of the proposed system was shown in a brain phantom, mimicking laser ablation of a lesion in a pituitary fossa. Evaluation of laser tip position showed the average positional error of 0.13 mm.

Chapter 5 further investigated the double-helix design presented for the first time in Chapter 4. Nine designs were tested by adjusting design parameters, such as number of helix revolutions and helical thickness. Out of tested designs, two with the highest ratio of torsion to deflection were chosen for further testing. We showed independent actuation in 1D electromagnetic coil of three independent segments. This shows promise of multi-tool actuation with SMMs.

Apart from multiple tool actuation, as explored in Chapters 4 and 5, stability is another significant requirement when utilizing SMMs in surgical tasks. Considering the soft nature of SMMs, procedures requiring any force transmission at the tip, or accurate tip control e.g. for laser ablation, are challenging due to buckling.

Chapter 6 explores utilization of a pneumatic chamber embedded in SMM design for improved stability in procedures requiring accurate tip actuation. By integrating inflating anchor, we successfully showed that the SMM can be locked in position, when arriving at a target and perform accurate laser ablation. We showed that the system was 4.7 times more accurate on average than SMM without the anchoring mechanism. The design supported up to 30 g weight at its tip before it slipped out of a lubricated lumen in which it was anchored. This is a promising result, showing that procedures with required payload of 30 g at the tip (or reaction force), could be possible with SMMs combined with presented anchoring mechanism.

Remaining challenges and areas of future research that should be investigated following the research presented in this thesis are highlighted in more detail below.

7.1 Open Challenges

7.1.1 Miniaturization

Further miniaturization of endoscopic tools is crucial for moving the advancement of interventional endoscopy deeper into the human anatomy. Scaling down beyond sizes presented in this thesis (2 mm - 3.5 mm) would allow entry into anatomical structures which are currently inaccessible.

There are fabrication techniques that can produce magnetic structures smaller than current SMMs (less than 2 mm), such as aerosol jet printing; [1] or adapted 3D printing techniques [2], [3]. However, apart from manufacturing challenges, there are multiple limitations that can arise after scaling down the SMMs.

Main concerns for miniaturization come from scaling down torques and forces that can be generated, due to decrease in volume of magnetic elements. As described in section 2.3, magnetic actuation heavily relies on the volume of the magnetic element.

Additionally manufacturing methods presented in this paper have size limitations too. Injection moulding techniques explored in this thesis, utilizing SLA 3D printing (Form 3, Formlabs, USA) for mould manufacturing, can produce cylindrical SMMs approximately 1mm in size. However, considering available technology to instrument the SMM with tools, it is limited at this size. This means that the tool channel needs to be at least 1 mm for any currently used endoscopic tools (grippers, forceps etc.) other than a functional fiber (e.g. optical fiber, FBG). Implementing such tool channel in an SMM can take away significant magnetic volume out of the manipulator, leading to further losses in available torque, which is significant at this scale.

Alternative to using off shelf surgical tools is to manufacture miniaturized versions that would fit our size requirements (less than 1 mm). This, however, presents itself with an issue of available payload due to size, as well as e.g. grip force in the case of grippers or cutters.

7.1.2 Independent and Collaborative SMM actuation

In Chapter 4, the prototyped sets of manipulators for both control strategies, were tested extensively for the available workspace, considering two bending primitives creating a cross motion when combined (as in Chapter 4, Section 3.2, Figure 4.10).

This was done to simplify the experimental process and showcase the constraint of the double helix; however, it is possible to actuate the SMMs in more DoFs. In the orthogonal magnetization strategy, this can be achieved by overcoming our set maximum field (7.5 mT) that would activate the constrained plane of the SMM. This threshold magnitude of 7.5 mT was chosen experimentally, for the given set of manipulators. This value will be different depending on the material used for manufacturing, concentration of magnetic particles, varied helix parameters, diameter or length of the SMM.

Actuating the manipulator beyond this threshold magnitude would be a first step to develop the system further, where apart from independent control, it could provide a level of collaborative control when needed, which is important in many surgical scenarios. The available area is expected to be comparable in size, through optimizing magnitude of applied fields, as well as their direction, to overcome the mechanical constraint of the double helix when bending on the high stiffness plane.

In the Parallel Magnetization (PM) strategy, the main limitation was lower range of motion than in the OM case. This can be improved by either increasing NdFeB particle concentration,

decreasing the SMM diameter or applying field gradients higher in magnitude (e.g. with bigger permanent magnets).

Moreover, it is important to emphasize that achieving independent actuation (or collaborative actuation in the future) using this approach heavily depends on the precise calibration of the dEPM system and accurately identifying and aligning the focal point. Even minor deviations in the focal point can lead to simultaneous activation of both SMMs. Moreover, calibration accuracy is crucial for determining the symmetry of the reachable workspace for both manipulators. To overcome these precision-related challenges, future enhancements to the calibration methods of the dEPM platform may involve integrating more accurate optical tracking systems. Collaborative control with the utilization of magnetic field gradients introduces different challenges than the OM strategy. This would require a higher-level magnetic field generating system, which can shift the focal point on demand with high precision. Placing the focal point at different locations in between the manipulators would allow application of magnetic field gradients varied in magnitude on the SMMs, to achieve different deformation of the two SMM simultaneously.

For both presented magnetization strategies, it is important to test them further with different lengths of the SMMs, which will affect the available workspace area. Shorter SMM length is also expected to allow independent actuation at smaller distances than tested in this work (less than 2 cm separation), which would be suitable for applications in smaller anatomical cavities.

An alternative approach to independent SMM actuation is utilization of the inflating chamber presented in Chapter 6 in set-ups with two or more SMMs. Integration of a chamber (or multiple chambers) which can stabilize the whole length of the SMM can be beneficial to facilitate independent actuation of another, non-stabilized SMM in the workspace.

Chapter 4 primarily focused on demonstrating the concept of independent tool manipulation using two SMMs. To fully assess the system's reliability, further testing is needed to evaluate repeatability through additional experiments and statistical analysis.

7.1.3 Stability in surgical tasks

Results presented in Chapter 6 showed that tip actuation was 4.7 times more accurate in an anchored SMM than in unanchored SMM. Tests performed in this study were limited to three different lumens, including dry and lubricated tubes. Even though two of the used tubes were mechanically accurate phantoms of human vasculature, more testing should be performed in soft tissues in the future. Specifically, since the focus of the work was to stabilize the SMM for surgical tasks, more examples of possible procedures should be tested, such as those requiring high payloads at the tip or reaction force, e.g. biopsy, tissue grasping, injection.

A deeper dive into fabrication of the pneumatic chamber should also be investigated to improve robustness of the system and fabrication repeatability. The PTFE mask can be laser cut to the desired width to more accurately accommodate pneumatic connection fixed along the magnetic segment. We found that in some cases, movement of the tube after/during silicone injection affected alignment of the chamber, creating nonconcentric placement of the balloon.

Utilization of the anchor in a longer SMM should also be explored. An additional balloon at the distal end can be added for improved stability of the body while actuating the tip.

7.1.4 Biocompatibility

The elastomers used in this work were chosen due to their availability, low cost for prototyping and ease of use. Even though the range of silicones used in this work (Smooth-on, USA) is not cytotoxic, they are not considered biocompatible. Translation of SMMs into clinical practice

would require utilization of medical grade materials for device fabrication. The choice of material should be guided not only by the need to meet mechanical requirements but also by ensuring the material's safety when in contact with tissues. Some candidate materials can include medical-grade silicones [4] or UV-curable flexible materials (e.g. Stratasys, Formlabs). Additionally, the material must have the capacity to incorporate sufficient NdFeB microparticles into its matrix to achieve the desired behavior, which varies depending on specific use case.

Apart from the elastomeric matrix, NdFeB particles themselves can pose a risk in the body. Although alternative magnetic particles with lower biocompatibility risks, such as iron-based compounds, are available, NdFeB microparticles remain the optimal choice for integration into SMMs due to their superior coercivity and remnant magnetization [5]. These magnetic properties enable magnetic programming through the ability to magnetize the structure or its sections in specific directions [6], [7]. To transition NdFeB-doped devices into clinical applications, it is imperative to address safety and toxicity concerns. This can be effectively managed by coating the devices with biocompatible material. However, standard coating techniques employed in the medical device industry are primarily designed for smooth surfaces, such as those of rubber or polymer tubes (e.g., catheters, guide wires, cannulas). These conventional methods may present challenges when applied to structures with complex geometries, such as SMMs reinforced with helical patterns. Recent research has explored methods to coat non-uniform objects, including advancements in hydrogel skin technology [8] and hydrogel paint [9]. Coating SMMs could not only mitigate biocompatibility concerns but it can also potentially offer additional benefits, such as reducing friction coefficients, which is particularly advantageous for navigational purposes. An interesting area to explore is drug doped coatings e.g. hydrogels that by dissolving in vivo would locally release treatment to the affected area, similarly as in [10], [11], [12].

Alternatively, treating individual particles pre-fabrication could also solve the issue of cytotoxicity. As presented in [13], coating NdFeB microparticles in silica prevents particle corrosion. Given that silica is inherently biocompatible and noncytotoxic, it can be reasonably assumed that the coated NdFeB particles will exhibit similar properties. However, this assumption requires further investigation to confirm.

References

- [1] S. Taccola, T. da Veiga, J. H. Chandler, O. Cespedes, P. Valdastri, and R. A. Harris, “Micro-scale aerosol jet printing of superparamagnetic Fe₃O₄ nanoparticle patterns,” *Sci. Rep.*, vol. 12, no. 1, pp. 1–12, 2022, doi: 10.1038/s41598-022-22312-y.
- [2] M. H. D. Ansari *et al.*, “3D Printing of Small-Scale Soft Robots with Programmable Magnetization,” *Adv. Funct. Mater.*, vol. 33, no. 15, 2023, doi: 10.1002/adfm.202211918.
- [3] Z. Liu, M. Li, X. Dong, Z. Ren, W. Hu, and M. Sitti, “Creating three-dimensional magnetic functional microdevices via molding-integrated direct laser writing,” *Nat. Commun.*, vol. 13, no. 1, pp. 1–11, 2022, doi: 10.1038/s41467-022-29645-2.
- [4] M. Zare, E. R. Ghomi, P. D. Venkatraman, and S. Ramakrishna, “Silicone-based biomaterials for biomedical applications: Antimicrobial strategies and 3D printing technologies,” *J. Appl. Polym. Sci.*, vol. 138, no. 38, pp. 1–18, 2021, doi: 10.1002/app.50969.
- [5] B. L. Gray, “A review of magnetic composite polymers applied to microfluidic devices,” 2014, *Electrochemical Society Inc.* doi: 10.1149/2.023402jes.
- [6] J. J. Abbott, E. Diller, and A. J. Petruska, “Magnetic Methods in Robotics,” *Robot. Auton. Syst.*, vol. 19, no. 4, 2019, doi: 10.1146/annurev-control-081219.
- [7] G. Z. Lum *et al.*, “Shape-programmable magnetic soft matter,” *Proc. Natl. Acad. Sci. U. S. A.*, vol. 113, no. 41, pp. E6007–E6015, Oct. 2016, doi: 10.1073/pnas.1608193113.
- [8] Y. Yu *et al.*, “Multifunctional ‘Hydrogel Skins’ on Diverse Polymers with Arbitrary Shapes,” *Adv. Mater.*, vol. 31, no. 7, pp. 1–9, 2019, doi: 10.1002/adma.201807101.
- [9] X. Yao *et al.*, “Hydrogel Paint,” *Adv. Mater.*, vol. 31, no. 39, pp. 1–8, 2019, doi: 10.1002/adma.201903062.

-
- [10] R. De Piano, D. Caccavo, S. Cascone, C. Festa, G. Lamberti, and A. A. Barba, “Drug release from hydrogel-based matrix systems partially coated: experiments and modeling,” *J. Drug Deliv. Sci. Technol.*, vol. 61, no. August 2020, p. 102146, 2021, doi: 10.1016/j.jddst.2020.102146.
- [11] R. Narayanaswamy and V. P. Torchilin, “Hydrogels and their applications in targeted drug delivery,” *Molecules*, vol. 24, no. 3, 2019, doi: 10.3390/molecules24030603.
- [12] J. Li and D. J. Mooney, “Designing hydrogels for controlled drug delivery,” *Nat. Rev. Mater.*, vol. 1, no. 12, 2016, doi: 10.1038/natrevmats.2016.71.
- [13] Y. Kim, G. A. Parada, S. Liu, and X. Zhao, “Ferromagnetic soft continuum robots,” *Sci. Robot.*, vol. 4, no. 33, p. eaax7329, 2019, doi: 10.1126/scirobotics.aax7329.